

IMPROVED UNDERSTANDING OF METAL CUTTING BASED ON SLIP-LINE FIELD  
THEORY

A Dissertation by

Amit Anand Deshpande

Master of Science, Wichita State University, 2006

Bachelor of Engineering, Pune University, India, 2004

Submitted to the Department of Industrial Engineering  
and the faculty of the Graduate School of  
Wichita State University  
in partial fulfillment of  
the requirements for the degree of  
Doctor of Philosophy

December 2012

© Copyright 2012 by Amit Anand Deshpande

All Rights Reserved

IMPROVED UNDERSTANDING OF METAL CUTTING BASED ON SLIP-LINE FIELD  
THEORY

The following faculty members have examined the final copy of this dissertation for form and content, and recommend that it be accepted in partial fulfillment of the requirements for the degree of Doctor of Philosophy with a major in Industrial Engineering.

---

Vis Madhavan, Committee Chair

---

Amir Adibi-Sedeh, Committee Member

---

Krishna Krishnan, Committee Member

---

Charles Yang, Committee Member

---

Bob Minaie, Committee Member

Accepted for the College of Engineering

---

Zulma Toro-Ramos, Dean

Accepted for the Graduate School

---

Abu S.M. Masud, Interim Dean

## DEDICATION

To my parents and my sister

## ACKNOWLEDGMENTS

I take this opportunity to express my sincere gratitude to my advisor and dissertation committee chair, Dr. Vis Madhavan, for his valuable guidance and continuous motivation in performing this work. I would always be indebted to him for the knowledge which he has imparted to me. I also thank him for providing the financial as well as the emotional support required to face all the ups and downs during this journey.

I thank my co-advisor Dr. Amir Adibi-Sedeh for providing valuable inputs at all stages of this work. He took time out on a regular basis to meet with me and provided his guidance right from pointing out good literature to implementing new concepts. I thank Dr. Krishna Krishnan for providing financial support to me as well as for reviewing my work by being a part of my dissertation committee. I am thankful to Dr. Charles Yang for providing me with the minor exam in Solid Mechanics and Dr. Bob Minaie for taking time from his busy schedule to review my work. I am grateful to John Matrow for all his help in getting my analyses done at the WSU HIPECC facility. I am grateful to Valerie Mounes from the graduate school for promptly helping to address all my queries. I am also grateful to the entire faculty and staff of the Industrial Engineering department for their help and cooperation.

I thank my lab mates Mahdi Saket Kashani, Kiran Srinivasan, Palanivel Swaminathan, and Sreedhar Vasomsetti for all their help and inspiration. I thank my roommates and friends, who made Wichita State, a very pleasant and memorable experience for me. Finally, the encouragement, which I have received from my parents and my sister, is an everlasting inspiration for me. I would always be indebted to them for continuing to have faith in my abilities. It would be impossible for me to thank them for their innumerable sacrifices, on which I am standing today.

## ABSTRACT

This dissertation consists of three papers, which describe a new capability for deriving slip-line fields (SLFs) from results of finite element analyses, and its application to the problem of metal cutting. The first paper describes the new SLF generation capability, that uses the stress components obtained from FE analysis (which already satisfy the equations of equilibrium) to obtain the first and second directions of maximum shear stress, the streamlines of which are the slip-lines. This new capability for slip-line field generation has been validated using the problem of compression of a plate between rough platens and there is an exact match between the slip-lines generated from FEA results and the analytical slip-line solution.. This study also shows the importance of alignment of the mesh with the velocity discontinuities in order to capture them accurately, as pointed out by various researchers.

In the next chapter, the reason the hydrostatic pressure around the cutting edge in machining is much lower than that under an indenter, has been investigated by comparing the machining process with flat punch indentation. Using finite element simulations of flat punch indentation, it is shown that for confinement ratios above the critical value, the field is that given by Prandtl for flat punch indentation. But for confinement ratios less than the critical value, the indentation field changes to a ‘S’ shaped shear plane field which is similar to that in machining. The analogy with machining is made clear using finite element simulation of the initial contact between the workpiece and a tool with a rake angle of  $0.05^\circ$ . It is found that the slip line field is initially an indentation field. As the contact length increases, the field switches over to the ‘S’ shaped shear plane field at the exact confinement ratio (8.59) given by Chakrabarty (1987), to within the resolution of the mesh. This makes it clear that the ratio of the depth of cut to the contact length between the tool and the chip is the confinement ratio in machining. As the length

of contact increases further, the contact pressure is observed to decrease. In metal cutting, the contact length is typically larger than the uncut chip thickness, making the confinement ratio less than one. Since the confinement ratio is very small compared to that in indentation, the hydrostatic pressure observed at the cutting tool tip is much smaller compared to that under the indenter.

The new slip-line field generation capability is then applied to metal cutting. A new slip-line field model is developed for machining with tools having a finite cutting edge radius. The slip-line field model is based on the results of finite element simulations carried out under different conditions of friction, rake angle, and the ratio of the uncut chip thickness to the cutting edge radius ratio. It is shown that there exists a Dead Metal Zone (DMZ) for all non-zero values of sticking friction coefficient ( $m > 0$ ). For  $m < 1$ , it is clearly shown that the plastic deformation originating from the lower boundary of the DMZ reaches the free surface of the chip forming a Primary Shear Zone (PSZ). At point A on the free surface, the width of the PSZ is zero making it a pressure singularity.

## TABLE OF CONTENTS

Chapter	Page
1. INTRODUCTION.....	1
1.1 Metal Cutting Process.....	1
1.2 Contribution of the Cutting Edge in Machining .....	2
1.3 Dead Metal Zone in Machining.....	3
1.4 Constitutive Material Models .....	3
1.5 Need for Finite Element Analysis.....	4
1.6 Significance of the Slip-Line Fields .....	5
1.7 Objectives of this Research .....	6
1.8 Organization of this Dissertation .....	6
2. GENERATION OF SLIP-LINES BASED ON DATA OBTAINED FROM FE ANALYSES .....	8
2.1 Abstract.....	8
2.2 Introduction.....	9
2.3 Basics of Slip-Line Fields.....	9
2.4 Previous Approaches Used to Generate Slip-line Fields .....	11
2.5 Different Finite Element Analysis Techniques to Capture the Velocity Discontinuities .	14
2.6 New Finite Element Based Slip-line Field (SLF) Generation Approach.....	20
2.7 Compression of a Flat Plate under the Action of a Rough Punch.....	22
2.8 Explanation of the Slip-Line Field.....	23
2.9 Effect of Mesh Refinement.....	26
2.10 Effect of Mesh Size.....	29
2.11 Verification of the Achievement of Steady Deformation Field .....	31
2.12 Check for Elastic Effects .....	32
2.13 Satisfaction of Hencky’s Equations .....	33
2.14 Comparison of Radii of Curvatures and Velocities with Analytical Calculations.....	34
2.15 Satisfaction of Geiringer’s Equations .....	37
2.16 Comparison of the Shear Strain Rate Obtained from FEA with Analytical Calculations	38
2.17 Discussion.....	39
2.18 Conclusion .....	41
2.19 Acknowledgement .....	42

## TABLE OF CONTENTS (continued)

Chapter	Page
2.20	References..... 42
3.	UNDERSTANDING THE PRESSURES IN MACHINING WITH ANALOGY TO FLAT PUNCH INDENTATION..... 45
3.1	Abstract..... 45
3.2	Introduction ..... 45
3.3	Background..... 46
3.4	Indentation Pressure in Machining ..... 52
3.5	Analogy between Machining and Indentation ..... 54
3.6	FE Simulation Technique and Generation of Slip-lines ..... 55
3.7	Verification of Attainment of Steady State..... 57
3.8	Simulations with Different Values of the Confinement Ratios ..... 59
3.9	Results for the Simulation with Different Confinement Ratios..... 59
3.10	Effect of Friction on the Critical Confinement Ratio ..... 62
3.11	Simulation with an Inclined Punch..... 63
3.12	Results for the simulation with the inclined punch..... 63
3.13	Discussion..... 66
3.14	Conclusion ..... 67
3.15	Acknowledgement ..... 68
3.16	References ..... 68
4.	SLIP-LINE FIELD MODEL FOR TOOLS WITH FINITE CUTTING EDGE RADIUS ..... 72
4.1	Abstract..... 72
4.2	Introduction ..... 73
4.3	Background..... 73
4.4	Finite Element Analysis and the Slip-Line Field Generation Technique ..... 77
4.5	Effect of Mesh Alignment ..... 81
4.6	Verification of Attainment of Steady State..... 82
4.7	Effect of Friction Along the Chip-Tool Contact..... 84
4.8	Effect of Friction on the Size and Extent of the Dead Metal Zone (DMZ) ..... 87
4.9	Effect of the Depth of Cut and the Radius of the Cutting Edge ..... 89
4.10	Effect of the Rake Angle ..... 93

## TABLE OF CONTENTS (continued)

Chapter	Page
4.11	Discussion on Different Regions of the Field..... 94
4.12	Equilibrium Based Explanation for Dependence of Shear Plane Angle on the Friction 104
4.13	Significance of the New Slip-Line Field Model..... 104
4.14	Variation of the different angles in the proposed slip-line field ..... 105
4.15	Estimation of the Indentation force Component..... 106
4.16	Slip-Line Field for Straight Chips ..... 108
4.17	Discussion..... 110
4.18	Conclusion ..... 112
4.19	Acknowledgement ..... 113
4.20	References ..... 113
5.	CONCLUSIONS AND FUTURE WORK ..... 116
5.1	Conclusions ..... 116
5.2	Future Work..... 121
	BIBLIOGRAPHY ..... 123

# CHAPTER 1

## INTRODUCTION

### 1.1 Metal Cutting Process

Machining is the most widely used process in the manufacturing of parts and products (Childs et. al., 2000). Increasing the productivity without compromising the part quality is the key to success in today's competitive environment. Hence, there is a need to optimize manufacturing processes like machining. However, in order to optimize the machining process, first, it needs to be understood completely.

The simplified version of any metal cutting process is the orthogonal machining process. Any metal cutting process, in which the cutting edge of the cutting tool is perpendicular to the velocity of the cut, is known as orthogonal machining process. The main advantage of this process is that the chip formation process is the same everywhere along the cutting edge, throughout the width of the cut. For this reason, the 3D orthogonal machining process shown in Figure 1.1(a) can be simplified to the 2D orthogonal machining process as shown in Figure 1.1(b). This simple orthogonal cutting operation represents a reasonably good approximation of

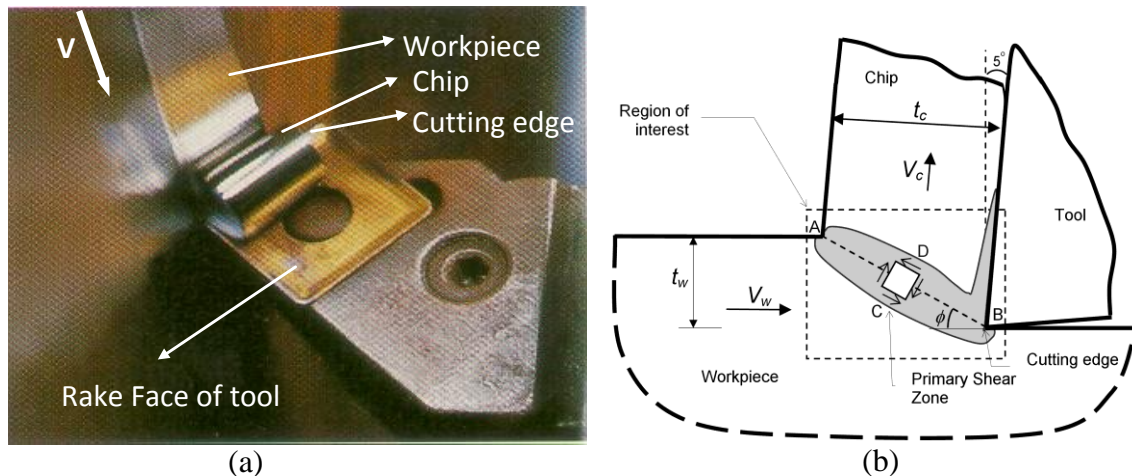


Figure 1.1:(a) Orthogonal cutting as a three dimensional cutting (Sandvik, 1996) and (b) Orthogonal cutting simplified to a two dimensional cutting process

the performance of the major cutting edge and for this reason, has been extensively studied by various researchers.

During the process of metal cutting, the work material undergoes strains greater than 100% at extremely high strain rates of the order of  $10^3/s$  to  $10^6/s$ . For this reason, the metal cutting process can be considered to be a good test for obtaining the mechanical properties of a material in high strain and strain rate range. Large shear strains ( $\gamma > 1$ ) are induced in the workpiece as the material flows through a thin zone called the primary shear zone (PSZ) to form a chip as seen in Figure 1.1. The length of the PSZ extends from the tool tip to the free surface of the chip and its thickness ranges from few tens of micrometers to hundreds of micrometers. For range of cutting speeds (0.1 m/s to 100 m/s), it usually takes one millisecond (slowest velocity) to less than a microsecond (fastest velocity) for the material to pass through the PSZ. The large deformation induced in such a thin region of PSZ causes the strain rates to be extremely high.

## **1.2 Contribution of the Cutting Edge in Machining**

The interaction of the cutting tool and workpiece material in metal cutting comprises of two actions. First action is the shearing action, which separates the material being cut into machined workpiece and the chip. The second action is the indentation action in which the tip of the tool with finite edge radius presses against the workpiece increasing the contact pressure in the material just ahead of the cutting edge. This additional pressure, also contributes towards increasing the cutting and the thrust force generated during cutting.

Albrecht (1961) was one of the first researchers to point out that the effect of the cutting edge (ploughing) is one of the significant factors, which affect the mechanics of metal cutting. Palmer and Yeo (1964) performed cutting tests with artificially blunt tools to understand the flow

of material around the cutting edge. Other researchers like Basuray and Misra (1976), showed that the effect of cutting edge becomes more significant in finishing operations, where the depth of cut is small. Most of the researchers agree that the cutting edge has a significant contribution in the metal cutting process, but there is not much research available, which quantifies the effect of cutting edge (forces, extent of the dead metal zone etc).

### 1.3 Dead Metal Zone in Machining

The material being cut has a tendency to accumulate in front of the cutting edge of the tool. This accumulated material, doesn't move and hence, this zone is termed as the dead metal zone as shown in Figure.1.2. The orientation and the extent of this dead metal zone (DMZ) depends on the properties of the material being cut, cutting tool geometry (rake angle and the cutting edge radius), and the cutting conditions (coefficient of friction at the tool-chip interface, the depth of cut, and the cutting velocity).

This DMZ acts as a “false tip” and thus changes the effective cutting tool tip geometry.

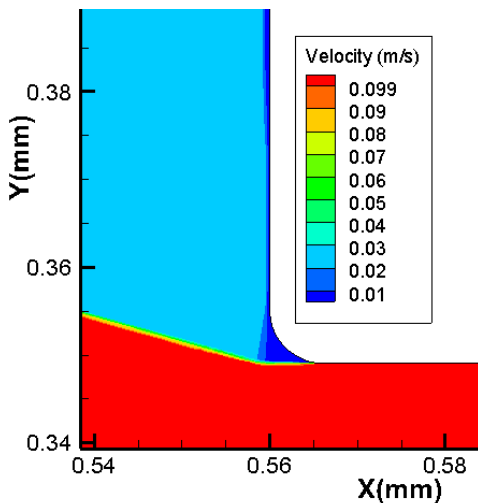


Figure.1.2: A Dead Metal Zone (DMZ) can be observed for cutting condition of 18  $\mu\text{m}$  depth of cut with a zero degree rake angle tool of 6  $\mu\text{m}$  cutting edge radius.

This change in the tool tip geometry has a significant impact on the cutting process. For this reason, it is important to understand the formation of the DMZ.

### 1.4 Constitutive Material Models

The most popular test used to generate data for high strain rate material models is the Split Hopkinson Pressure Bar (SHPB, also known as the Kolsky bar test) test. However, compared to metal cutting, this test generates limited strains of about 40% to 50% of values observed in machining and that too, at limited

strain rates (less than  $10^4$ ). This drawback of the SHPB is clearly visible when the constitutive models generated from the test data are unable to predict the experimental observations in metal cutting. The errors in prediction of the cutting forces are sometimes more than 100% (Srinivasan and Madhavan, 2010). This shows that the constitutive model coefficients obtained from SHPB are not even close to the actual material behavior. Also, phenomenological models like the Johnson-Cook model do not perform well when extrapolated, and so there is a need for data at higher strains and strain rates. For this reason, the model constants obtained based on the SHPB tests can't even be used as a good starting point for constitutive model development. On the other hand, it is hoped that the coefficients that have been obtained from machining tests itself, for the same material model, might better match the experimental observations. In order to improve the predictions of these material model constants, accurate estimation of the flow stress is essential. In order to calculate the value of the flow stress accurately, a correct estimate of the shear force components is required by compensating for indentation force. Madhavan et. al. (2005) have used the Digital Image Correlation (DIC) technique to obtain the strain as well as strain rates from actual cutting tests. The average temperature along the Primary Shear Plane (PSP) can then be obtained from Oxley's analysis (Oxley, 1989) using Wiener's heat partition coefficient. This data can then be used to fit a constitutive model like the Johnson Cook (JC) material model. It has been observed from various finite element simulations that the flow stress along the primary shear plane ends up being uniform inspite of using the Johnson Cook (JC) material model coefficients (Deshpande, 2011). This suggests that the strains, strain rates, and temperatures within the PSZ vary in manner such that the flow stress ends up being a constant value.

## **1.5 Need for Finite Element Analysis**

In machining, the material has to go through extreme shear at very high rates. Also, there is tremendous amount of heat generated due to this shear. All these quantities have very large gradients and hence measuring them experimentally is a very tough task. The values obtained from the thermocouples and strain gauges are the average values rather than the more interesting local values. Further, it is extremely difficult to replicate the cutting process by means of non cutting tests, like the Split Hopkinson Pressure Bar Test (SHPB). This can be attributed to the incapability of SHPB to generate the large strains as well as strain rates as observed during actual metal cutting.

Solving the machining problem analytically involves very complex calculations. Most researchers (Oxley, 1969, Adibi et. al., 2004) have used various assumptions about the shape of the shear plane, the thickness of the shear plane, the radius of the cutting edge, the distribution of heat generation and so on to simplify the calculations. Using such assumptions induces inaccuracy in the analyses of machining process.

On the other hand, Finite Element Analysis (FEA) has emerged as a powerful computational tool which has the ability to solve complex equations without many simplifications. Due to these disadvantages of experimentation and analytical solutions, and the continuing increase in computation power, FEA is being used extensively to simulate and study material removal processes.

## **1.6 Significance of the Slip-Line Fields**

The first and second directions of the maximum shear stresses are known as slip-lines. Slip-lines help in understanding the complex deformation patterns observed in large deformation plane strain problems. Slip-lines provide a very good first approximation of the loads at yielding (Johnson and Mellor, 1973). There are relationships governing the pressure distribution and the

velocity distribution along the slip-line families known as the Hencky's equations and the Geiringer's equations respectively. These relationships assist in finding solutions for mixed (stress and velocity) boundary problems. Using slip-line field analysis in combination with the FE results, can lead to significantly improved understanding of a complex deformation process like machining.

### **1.7 Objectives of this Research**

The objectives of this research were as follows:

- 1) To develop and validate slip-lines based on the stress data obtained from Finite Element (FE) Analysis
- 2) To develop an analogy between flat punch indentation and metal cutting and use it to study the effect of confinement on the pressures observed at the tool tip.
- 3) To develop a slip-line field model for metal cutting using the slip-line field generation technique in objective one with finite edge radius tools and study the existence as well as estimate the boundaries of the dead metal zone
- 4) To estimate the indentation force contribution and to develop a relationship for the indentation pressure as a function of the cutting tool geometry (edge radius, rake angle) and the shear plane angle

### **1.8 Organization of this Dissertation**

Chapter 2 describes the different slip-line field generation approaches developed by previous researchers as well as the newly developed slip-line field generation approach where the stress and velocity results obtained from FE analysis, is used to find the first and second direction of the maximum shear stress which are nothing but the slip-lines. The FE simulations were carried out using the Lagrangian simulation technique in Abaqus/Standard. The symbolic

math package, MAPLE, was used to perform the slip-line calculations and Tecplot was used to generate the slip-line plots. This new technique of slip-line generation was validated by means of a flat punch compression problem. The slip-lines generated from FE results as per the new approach, were compared with the theoretical slip-lines for the same problem provided by Johnson and Mellor (1973).

An analogy between flat punch indentation and metal cutting was developed in Chapter 2. This helped in understanding key things like the dependence of indentation pressure on the confinement ratio i.e. the ratio of the contact length and the depth of cut. A critical confinement ratio at which the slip-line field changes from Prandtl's (1920) indentation field, to the one similar in machining was investigated in detail. This improved understanding was used to justify the lower than expected indentation pressures at the cutting tool tip.

The validated SLF generation approach discussed in Chapter 2 was used extensively in Chapter 4 to develop slip-line field for metal cutting process. When cutting with a tool of finite cutting edge radius, the total cutting force comprises of the force due to shearing of the material as well as due to the indentation action of the cutting tip. The variation of the pressure in front of the cutting edge as well as along the cutting edge was studied for different friction coefficients in order to develop a model for the indentation force. This understanding helped in separating the cutting forces due to shearing of material and due to indentation. Further, the shape and extent of the dead metal zone (DMZ) was also evaluated as a function of the cutting tool geometry and the cutting conditions.

The key findings of this research are summarized in Chapter 5 and the scope for furthering this research has been outlined.

## CHAPTER 2

### GENERATION OF SLIP-LINES BASED ON DATA OBTAINED FROM FE ANALYSES

#### 2.1 Abstract

A new approach of generating slip-line fields based on the results obtained from the Finite Element (FE) analysis has been developed. This new method makes use of the stress components obtained from FE analysis (which already satisfy the equations of equilibrium) to obtain the first and second direction of maximum shear stress, which are the slip-lines. Since the force and moment equilibriums are satisfied in FEA by default, no additional checks for these were required, which saved significant computational effort in slip-line generation, unlike previous slip-line field approaches of Dewhurst and Collins (1973).

The classic problem of compression of a plate between rough platens, for which there is a known slip-line field solution, was used for validation. Since, the slip-line field for this problem comprised of different types of regions, like the centered fan field, the extended fan field and the Dead Metal Zone (DMZ), and the velocity discontinuity along its boundaries, this problem was an ideal problem to validate the new approach. The slip-lines obtained from the new approach match exactly with the analytical slip-line solution provided by Johnson and Mellor (1983). It was found that, with the mesh exactly aligned with the slip-lines, the velocity discontinuity along the boundary of the DMZ could be captured within the width of two elements. The hodograph generated from the FE simulation in which the mesh was aligned to the slip-line field was found to match accurately with the one given by Johnson and Mellor. The newly generated slip-lines also satisfied Hencky's and Geiringer's equations. The velocity components in the slip-line field coordinate system, the radii of curvatures, and the strain rates were in good agreement with the analytical calculations.

## 2.2 Introduction

Slip-line field theory is widely used to analyze non homogeneous plane strain deformation of metals subjected to various manufacturing processes. It is applicable only to rigid perfectly plastic isotropic solids where the magnitude of the elastic strains is zero and the strain hardening and strain rate effects are absent (Hill, 1950). In spite of these idealizations, the slip-line field theory provides excellent insight

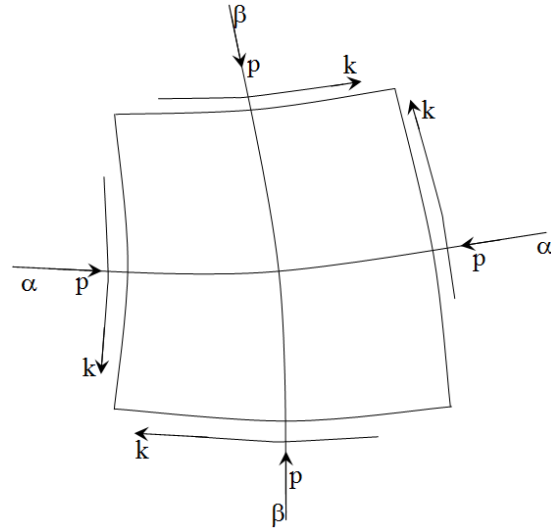


Figure 2.1: Stress on a small curvilinear element bounded by slip-lines, where  $p$  is the hydrostatic pressure and  $k$  is the yield shear stress (reproduced from Hill, 1950)

into the nature of deformations and gives good approximations of the load requirements in manufacturing processes like sheet drawing, rolling and forging (Johnson and Mellor, 1983). However, previous (direct) approaches of obtaining the slip-line field solution for plastic deformation problems were difficult to evaluate numerically without sacrificing the accuracy. The (indirect) matrix method was based on trial and error approach where the slip-line field was generated based on known boundary conditions and then checked for equilibrium.

With the advent of computational power, the Finite Element (FE) method has become more popular to solve plasticity problems. However, the FE method is time consuming and requires correct inputs for obtaining accurate output. Also, the FE method doesn't reveal much information about the physics in the process and doesn't provide adequate reasoning for the observed outputs. These details are better revealed by the slip-line field solutions.

## 2.3 Basics of Slip-Line Fields

Hill (1950) has defined slip-lines as the two orthogonal families of curves whose directions at every point coincide with those of the maximum shear strain rate. ' $p$ ' is the mean compressive

stress and ‘ $k$ ’ is the yield shear stress acting on a small curvilinear element as shown in Figure 2.1. The alpha and beta family of slip-lines are as shown in Figure 2.1. It follows that if  $\phi$  is the anti clockwise angular rotation of the alpha line from the x axis, the Cartesian components of stress are given as follows.

$$\begin{aligned}\sigma_x &= -p - k \sin 2\phi \\ \sigma_y &= -p + k \sin 2\phi \\ \tau_{xy} &= k \cos 2\phi\end{aligned}\tag{1}$$

Levy originally put forth these equations and they can be verified with the help of Mohr’s circle of stress. When these values of stress were substituted in the equilibrium equations, it was found that the tangential derivatives at any point P were,

$$\begin{aligned}p + 2k\phi &= \text{constant for an } \alpha \text{ line and} \\ p - 2k\phi &= \text{constant for a } \beta \text{ line}\end{aligned}\tag{2}$$

These equations were put forth by Hencky (1923) and are referred as the Hencky’s equations.

$$\begin{aligned}u_x &= u \cos \phi - v \sin \phi \\ u_y &= u \sin \phi + v \cos \phi\end{aligned}\tag{3}$$

Once the angle  $\phi$  is known everywhere, the Cartesian components of velocity,  $u_x$  and  $u_y$  can be transformed to components ‘ $u$ ’ and ‘ $v$ ’ which are along the  $\alpha$  and  $\beta$  slip-line direction respectively.

Further, similar to Hencky’s equations, Geiringer (1937) showed that

$$\begin{aligned}du - v d\phi &= 0 \text{ along an } \alpha \text{ slip-line and} \\ dv + u d\phi &= 0 \text{ along a } \beta \text{ slip-line}\end{aligned}\tag{4}$$

These equations mean that the rate of extension along any slip-line is zero.

This theory of slip-line fields has been applied to a wide range of boundary value problems with rigid plastic solids such as metal machining, metal forming, extrusion etc, where the plane strain condition assumptions can be made (Toulios and Collins, 1982).

## 2.4 Previous Approaches Used to Generate Slip-line Fields

The previous approaches of generating slip-lines comprised of a trial-and-error method to obtain the shape of an initial slip line or a finite difference approximation based influence coefficient technique, or the Riemann method of expressing the solution to the governing equations (Dewhurst and Collins, 1973).

Ewing (1966) was one of the first researchers to develop an exact method of slip-line field generation by direct summation of the convergent power series. An explicit solution in the form of a uniformly convergent double power series was presented for the radius of curvatures of the

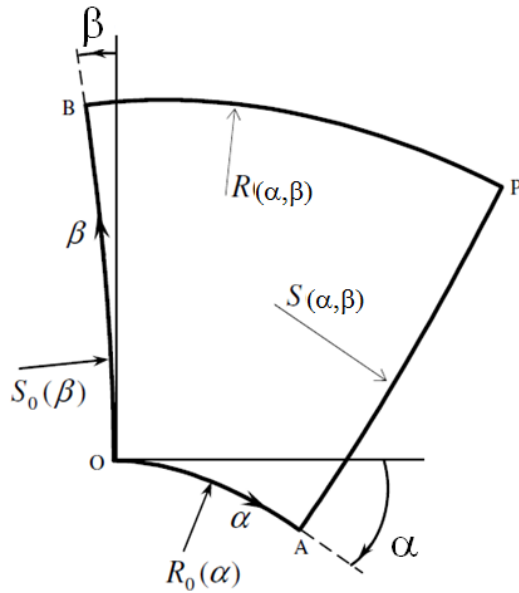


Figure 2.2: Pair of alpha and beta slip-lines with their radius of curvatures as  $R_0$  and  $S_0$  respectively are referred to as the base slip-lines. These were used to develop a convergent power series representation of the radius of curvature of the other two slip-lines.

alpha and beta slip-lines shown in Figure 2.2 by

$R(\alpha, \beta)$  and  $S(\alpha, \beta)$ .

$$\begin{aligned} -R(\alpha, \beta) &= \sum_{m,n=0}^{\infty} \left[ a_n \frac{\alpha^{m+n}}{(m+n)!} \frac{\beta^m}{m!} + b_n \frac{\alpha^m}{m!} \frac{\beta^{m+n+1}}{(m+n+1)!} \right] \\ -S(\alpha, \beta) &= \sum_{m,n=0}^{\infty} \left[ a_n \frac{\alpha^{m+n+1}}{(m+n+1)!} \frac{\beta^m}{m!} + b_n \frac{\alpha^m}{m!} \frac{\beta^{m+n}}{(m+n)!} \right] \end{aligned} \quad (5)$$

These expressions for the radius of curvatures shown in equation 5, were then used to derive expressions for other quantities like the tractions and the moments of the tractions. Since the direct

summation of convergent power series was used, the errors due to finite difference were completely eliminated by this approach. The only errors which

were present were the series truncation errors and the accumulated round off errors. It was possible to reduce the magnitude of these errors to a very small value by considering more terms in the power series. However, the main drawback of this approach was that the shape of the initial slip-lines had to be known before hand which was not always possible. The new technique was demonstrated with an example of the first boundary value problem. The power series expansions of the radii of curvatures were developed.

Collins (1967) further enhanced this technique by simplifying the representation of the radii of curvatures of the slip-lines and writing the power series expansion terms in the form of a column vector. This made it very easy to implement matrix algebra techniques and develop different algorithms and matrix operators. As shown in Figure 2.2,  $R_0(\alpha)$  and  $S_0(\beta)$  are the radius of curvatures of the starting slip-lines and are written in matrix form as below

$$R_0(\alpha) = \begin{bmatrix} a_0 \\ a_1 \\ \vdots \end{bmatrix} ; S_0(\beta) = \begin{bmatrix} b_0 \\ b_1 \\ \vdots \end{bmatrix}$$

$$R(\alpha, \beta) = P_\beta * R_0(\alpha) + Q_\beta * S_0(\beta) ; \quad (6)$$

$$S(\alpha, \beta) = P_\alpha * S_0(\beta) + Q_\alpha * R_0(\alpha)$$

Here, Different linear matrix operators ( $P$  and  $Q$ ) were developed for deriving the vector representation of any point in the whole slip-line field. Collins also formulated auxiliary matrix operators based on the principle of superposition and by using the different basic matrix operators. The technique was demonstrated for a problem of compression of plastic material between smooth dies.

In their work, Dewhurst and Collins (1973) addressed the main drawback of Ewing's approach, which is knowing the initial slip-line geometry a priori. They developed an indirect approach based on Ewing (1966) and Collins (1967) to obtain the slip-line field for a class of mixed (stress and velocity) boundary value problems. By this approach, the most important

problem of finding the shapes of the initial pair of the slip-lines simply was reduced to that of a matrix inversion. Further, different matrix operators like the  $P$ ,  $Q$ ,  $G$ , and  $F$  were developed which served different functions. The  $P$  and  $Q$  operators can construct a singular slip-line field on the convex side of a single slip-line. The  $G$  operator was used to establish the slip-line field between a given slip-line and a rough boundary. The  $F$  operator was used to establish the field between a given slip-line and a steady state deforming stress free surface. These matrix operators were used by various researchers like Fang (2003), to develop a slip-line field for metal cutting.

Petryk (1979) further established two additional matrix operators and called them operator  $H$  and  $E$ . The  $H$  operator was used in conjunction with the  $F$  operator to construct the characteristic net in the hodograph plane associated with the slip-lines intersecting the free surface. The  $E$  operator was used to satisfy the non dimensional velocity requirements of the hodograph characteristics and was based on the unit diagram concept of Hill (1950). Another big advancement in the application of matrix based slip-line field generation approach was by Dewhurst (1985), when he extended its application to obtain an approximate solution for a Coulomb friction boundary value problem where the shear stress along the contact is not uniform. Previously, these matrix operators were used only for linear boundary value problems.

In spite of these advances, the matrix method was time consuming and the computer programming was inefficient since it required solving a set of integral equations. Also, it was required to check whether the obtained slip-line field solution satisfied equilibrium. If not, then the process had to be repeated with different starting geometry of the initial slip-lines.

Smith and Gilbert (2007) developed a procedure to determine the critical layout of discontinuities in plasticity problems to obtain upper bound limit loads. Each node in the body under consideration is linked to every other node in the body by means of bars. The new optimization procedure which makes use of efficient linear programming is termed as the

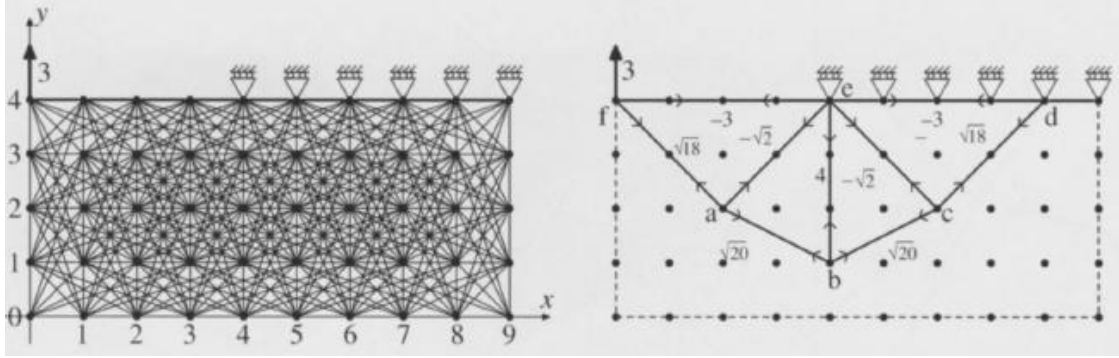


Figure 2.3: The analogy between truss and discontinuity layout optimization is shown for (a) a problem of loading a truss. The supports and ground structure as well as location of the pre existing bar, (b) the final optimal layout of truss bars obtained by eliminating the unwanted bars (adapted from Smith and Gilbert, 2007)

Discontinuity Layout Optimization (DLO). DLO was used to remove unwanted bars which represent the discontinuities and find the optimum configuration. Adaptive nodal analogy used to find translational failure mechanisms in plasticity problems. The orientation of slip line field in plasticity can be represented by bars in the optimized Mitchell structure. DLO involves minimizing total internal energy ( $\min E = [c_i l_i]^T d$ , subject to  $Bd = u$  and  $d \geq 0$ ) which is a product of shear displacement ( $d$ ), cohesive shear strength ( $c$ ), and length of the bar ( $l$ ).  $B$  represents the compatibility matrix and  $u$  represents the virtual displacements. This technique has been demonstrated with the help of flat punch compression problem. With this approach, the limiting stress at failure was overestimated by just 4% which was reduced to 0.04% by increasing the nodal density.

## 2.5 Different Finite Element Analysis Techniques to Capture the Velocity Discontinuities

With the significant advances in computation power, other approaches based on the finite element (FE) analysis technique were developed to obtain the slip-line fields. These approaches implemented the adaptive remeshing technique in order to align the mesh to the velocity discontinuities and captured the velocity discontinuities accurately. Gutierrez et. al. (1993) developed an algorithm for automatic rezoning of the mesh along with conservation of its initial

topology. Initial simulations was carried out with a coarse mesh and based on the outputs of these simulations, further mesh refinements were carried out which led to an improved solution. For each node in the two dimensional domain, the neighboring nodes formed the domain of influence as shown in Figure 2.4.

The influence domain was then divided into three noded triangular elements. The original node was moved to a new location such that the distortion of the triangular elements in the influence domain would be minimum. The distortion factor for each triangular element was calculated based on its height and base and the deviation of its shape from an isosceles triangle. This approach was able to make the mesh finer in the region of high plastic strains i.e. the region of discontinuity. Since the final element alignment was not exactly along the localization, the discontinuity was of finite width. This made it impossible to obtain discontinuities of infinitesimal width, which is important to obtain the correct geometry of the slip-lines as well as to calculate the

strain rates accurately.

Another similar approach developed by Deb et. al. (1996) was termed as a mesh enrichment procedure. This approach was able to capture the shear bands or localized deformations based on the strain localizations in elasto-(visco)-plastic solids. The researchers used three criteria to select the elements to be enriched, which were the velocity variations in the element, the equivalent plastic strains in the element, and

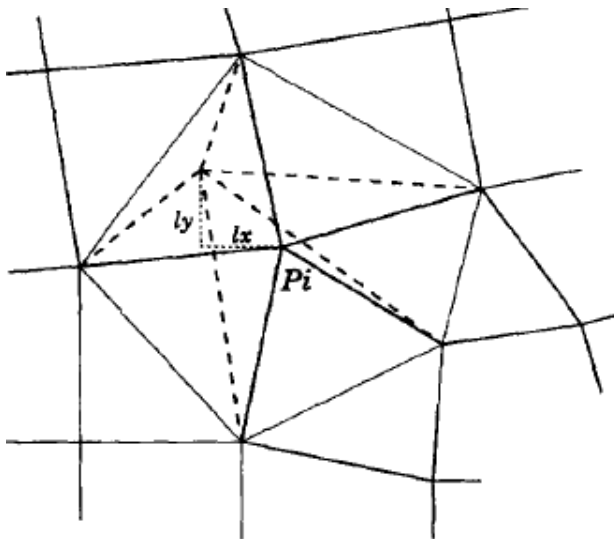


Figure 2.4: All the surrounding nodes of node  $P_i$  form its domain of influence. Node  $P_i$  is moved such that the distortion in the triangles is minimized. (adapted from Gutierrez et. al. ,1993)

the ratio of elastic and elastic plastic acoustic tensors. Out of the three criteria, the velocity variation and equivalent plastic strain are directly related to the material instability and the third criteria i.e. acoustic tensors is a representative of the localization characteristics. An adaptive mesh refinement scheme was implemented which carried out successive mesh refinements in the sub domains of interest only and not of the entire mesh domain. This selective mesh refinement in the region of localized deformation reduced the computation burden significantly.

The process consisted of different steps first of which was to identify the elements in the localized deformation domain. They were the elements which were crossed by shear bands as shown in Figure 2.5(a) and Figure 2.5(b). Then these elements were divided into four successor

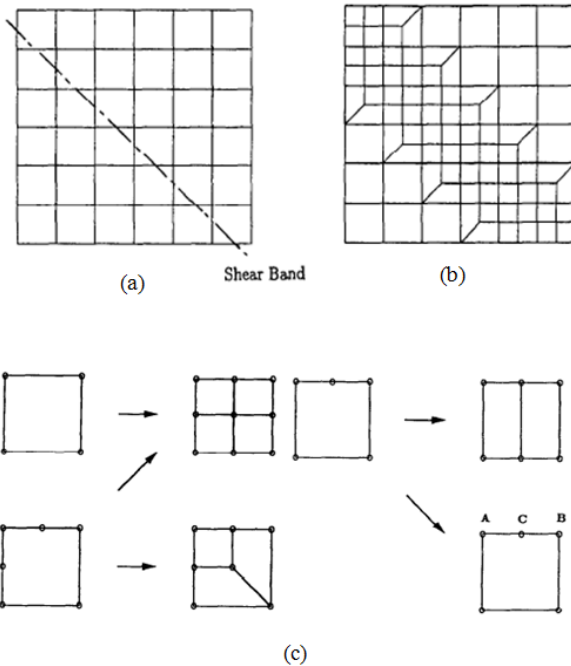


Figure 2.5: The localized deformation is identified in (a) and the localized splitting of the elements is carried out in (b), and (c) The localized enrichment was carried out by adding extra nodes on the edges of the 4 noded elements and then splitting them into multiple elements as shown. (adapted from Deb et. al. 1996)

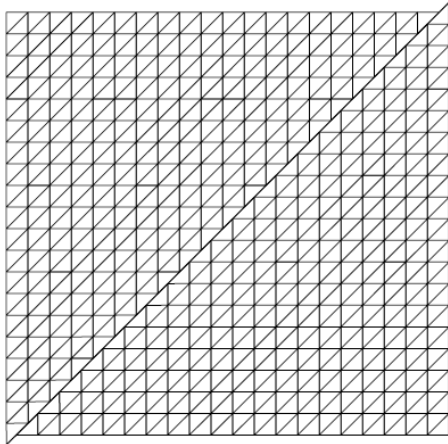
elements by adding new nodes at the centroid as well as at the centers of all the edges as shown in Figure 2.5(c). This was done to allow for the Laplacian smoothing. Due to addition of new nodes, the neighboring elements of the localized elements now had five or six nodes. The six-noded and five noded elements were then split into four four-noded quadrilateral elements or into three four-noded quadrilaterals elements. In this way, the mesh enrichment was carried out along the identified localized deformations. This approach suffered from the same drawback as the previously described approach of Gutierrez. The element edges were not aligned to the shear bands

and thus, were not able to capture the correct infinitesimal width of the discontinuities.

In an attempt to overcome the drawbacks of previous approaches like the finite width of discontinuity and its dependence on the mesh, Regueiro and Borja (1999) came up with a finite element model of the localized deformations based on the strong discontinuity approach previously developed by Simo et. al.(1993). The solutions obtained using this approach were independent of the mesh and hence didn't require any special remeshing and mesh alignment strategies. For the FE analysis, the rate independent Drucker -Prager plasticity model was used along with an enhanced strain quadrilateral element. The discontinuous displacements were detected using the localization condition which was based on the fact that for the equilibrium to be satisfied, the traction must be continuous across the discontinuity surface. The displacement field was reparameterized (the shape functions were modified) based on the jumps in displacement within the elements. This enhancement was then confined within the element boundaries. It has been shown that the solution is insensitive to the mesh since the edges of the elements through which the slip-lines are traced are not aligned to the slip-lines. They have demonstrated the technique for a slope stability problem where gravity loads are also applied, often considered in soil mechanics. In spite of overcoming the mesh dependency drawback of the previous approaches, their model is mathematically very complex and difficult to implement.

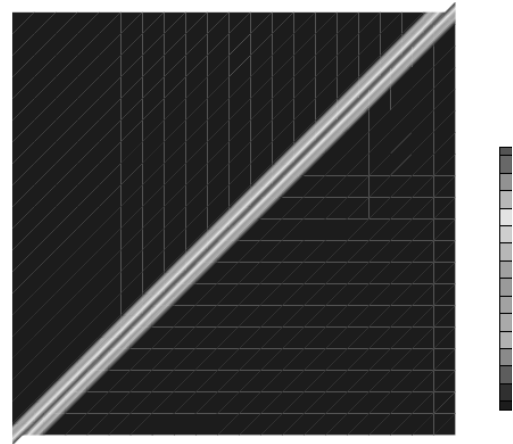
In his work Steinmann (1998) developed a finite element formulation in order to capture velocity discontinuities in a deforming non linear solid since they act as a failure mechanism in localization problems. A three step process was developed where the first simulation was carried out with a regular homogeneous mesh with four node elements. The deformation information from this simulation was used to perform adaptive meshing wherein the region was remeshed with triangular elements whose edges were aligned to the direction of the localizations and hence, the localizations were resolved within one to two elements. Even though the localizations were

Deformed Configuration: Aligned P111 Discretization



Mag.: 4

Plastic Zone: Aligned P111 Discretization



Mag.: 4

Figure 2.6: In the third step of the three step approach, Steinmann (1998) added interface elements along the discontinuity. The displacements were regularized to this layer of interface elements, thus giving a zero width discontinuity as can be seen in the figure. (Figure adapted from Steinmann (1998)).

resolved, the pattern of deformation was still continuous (distributed over the width of one to two elements) and of finite width. The deformation was still distributed to all the nodes of the elements along the localization. In order to capture the discontinuities in deformation a third step simulation was carried out where interface elements were added along the localization. Here, the deformations were regularized to the interface elements. The deformation pattern was now discontinuous and had zero width. The deformation was concentrated just along that edge of the interface elements.

Further, with the intension of carrying out a lower bound limit analysis for problems on soil mechanics, Lyamin et.al. (2005) used adaptive meshing technique to capture the discontinuity in the stress field accurately. They highlighted the importance of the arrangement and alignment of the discontinuities in obtaining accurate solutions especially in lower bound analysis. They identified two critical requirements, i.e. the adaptive mesh generator and the discretization error estimator, in order to be able to capture the discontinuities accurately. The advancing-front-type mesh generator first proposed by Prairie et. al. (1987) was used in this study. This approach has

the ability to generate the ‘fan’ zones which are centered on stress singularities. The advantage of these ‘fan’ fields is that they allow a fast transition of the stress components in the direction of their circumference about the singular point. Also, this technique has been found to be convenient for adaptive remeshing which involved stretching of the elements and ‘fans’ having multiple singularities. The rules put forth for placement of internal nodes were modified slightly to generate the required fan of elements at required locations on the initial front. Along with this, it was required to have information about the location of the center of each fan, the element density in the fan field, and the threshold distance beyond which the normal advancing front routine would resume. Different schemes for the discretization error were tested along with the advancing front meshing strategy. Best results were obtained when the magnitude of the Lagrangian multiplier was used as an error estimator, especially for the lower bound analyses. The approach has been demonstrated with two example problems i.e. ‘Critical height of an unsupported vertical cut’ and ‘rigid smooth strip footing on cohesive-frictional soil.’ The new approach developed was able to predict the actual collapse load in both the examples within one percent accuracy and that too with moderate number of elements.

The advancing front type mesh generator, similar to Lyamin et.al. (2005) discussed above, was also implemented by Sloan (2008). As described previously, the important features like the fan field centered on the singularity point can be modeled very efficiently. Usually, the mesh refinement proceeds with a small adjustment to the element size which resulted reduction of the local discretization error by uniform distribution over the entire mesh. But in their work, the element size distribution was chosen such that the global error would be minimum based on a designated control variable ‘u’ over the entire mesh. This approach was termed as the optimal-mesh-adaptive technique and in their study an improved version of this approach where the control

variables were plastic multipliers and velocity distribution, were used. The problem of ‘Critical height of an unsupported vertical cut’ was used to demonstrate the technique.

## **2.6 New Finite Element Based Slip-line Field (SLF) Generation Approach**

All of the FE based approaches described above are able to identify the localizations and the discontinuities in velocity field or stress field accurately. These approaches either refine or enrich the mesh in the regions of localizations to improve the results of the simulations. However, they don’t add to the understanding of the deformation patterns observed. The new approach developed below is similar in many respects yet significantly different from the above approaches. The new approach doesn’t stop at identifying and refining the mesh in the regions of discontinuities, but goes further to generate slip-line fields for the regions of plastic deformations. Generation of slip-lines provide significant insight in the understanding of the deformation patterns and observed pressures.

In the technique we have developed, a first simulation is carried out with a homogeneous mesh, similar to the previous approaches. Based on the stresses obtained from the simulation of this first analysis, a slip-line field is generated using MAPLE™, the details of which are explained later. These slip-lines are plotted using TECPLOT and the coordinates of the points along the slip-line field are extracted. These coordinates are entered into Abaqus CAE and are used to manually generate a new mesh for the region of interest. The newly generated mesh is well aligned to the slip-lines, since the coordinates of the slip-lines itself were used to generate the new mesh. A second simulation with the newly generated mesh is carried out which is able to capture the discontinuities in the velocity fields more accurately than the first one. A third step is rarely required if it appears that the deformation localizations are still not captured correctly. In that case, the mesh for the third simulation is generated based on the slip-line field generated from the

stress data of the second step simulation. In this way, the exact alignment of the mesh with the velocity discontinuity is achieved by making use of this iterative approach.

A new FE based slip-line field generation approach has been developed where, the local directions of principal stresses and maximum shear stress were identified for each plastically deforming element based on the stress components  $\sigma_1$ ,  $\sigma_2$ , and  $\sigma_{12}$ . The direction of the principal stresses ( $\theta$ ) is obtained using the following relationship.

$$\theta = \frac{\arctan\left(\frac{\sigma_{12}}{\frac{\sigma_{11}-\sigma_{22}}{2}}\right)}{2}; \eta_1 = \theta + \frac{\pi}{4}; \eta_2 = \theta + \frac{3\pi}{4} \quad (7)$$

The first and second directions of maximum shear stress ( $\eta_1$  and  $\eta_2$ ) which are the slip line directions for plastically deforming elements were calculated using the symbolic math package MAPLE™. The obtained maximum shear stress directions were then rearranged such that they are aligned to the maximum shear stress directions of the neighboring elements. The results were then imported in Tecplot and streamlines of these directions were plotted, which were the slip-lines

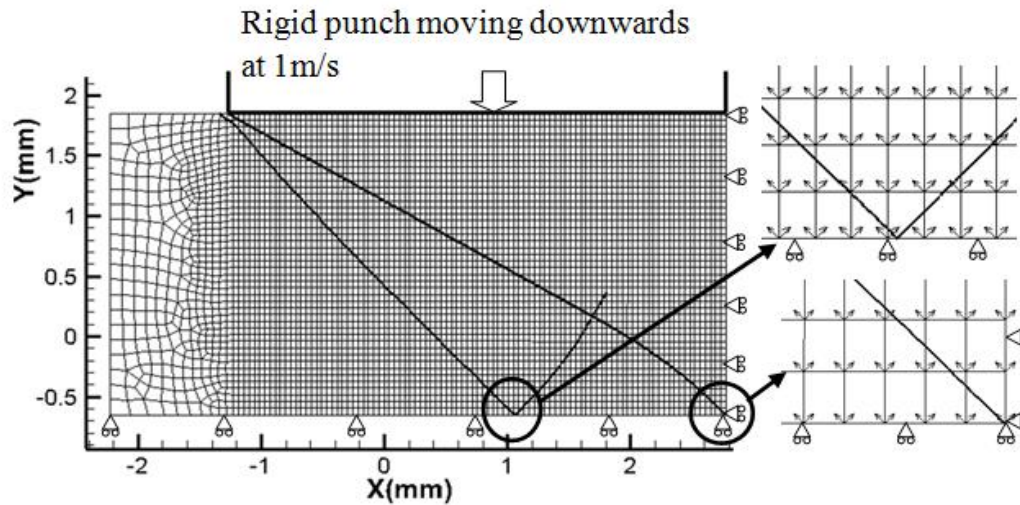


Figure 2.7: The compression of a plate under a rigid punch was simulated as a quarter model with the symmetry boundary conditions on the bottom and on the right edge as shown here for a punch width to plate height ratio of 1.6. The insets show the first and second slip direction vectors at different locations of the plate. The streamlines of these vectors are the slip-lines.

This method of generating SLFs by FEA has been validated using the rough punch compression problem. The slip-line field and the hodograph obtained from FEA were compared with those given by Johnson and Mellor (1983). The insets in Figure 2.7 show the direction of the 1<sup>st</sup> and second direction of the maximum shear stresses at different locations in the plate being compressed between rough platens. The orientation angle ' $\phi$ ' of the alpha slip-line with X axis can be easily found using trigonometry, once the alpha slip-line vectors are known. The equations given by Hencky (equation 2) and Geiringer (equation 4) can be verified using the values of orientation angle of the alpha slip-line ( $\phi$ ), shear stress ( $k$ ) and hydrostatic pressure ( $p$ ) within the plastic region. Since the new approach to obtain slip-line solution developed below is developed based on FE analysis, the need to check for validity of equilibrium equations is eliminated.

## **2.7 Compression of a Flat Plate under the Action of a Rough Punch**

Johnson and Mellor (1983) have provided the exact slip line field solution for compression under the action of rough platens for various ratios of punch width to plate height. Since the exact solution for a punch compression problem was available, this problem was used to validate the new slip line field generation methodology. . Further, the slip-line field for a punch compression problem comprises of various features like the dead metal zone (DMZ), the centered fan field and the extended fan field. The knowledge of material deformation in these regions can be used to develop slip-line fields for complex problems like metal cutting as demonstrated in our previous work (Deshpande et. al. 2011).

Two values for the ratio of the punch width to the plate thickness ( $2w/2h=1.6$  and  $2w/2h=3.6$ ) were selected for validating the new slip-line field approach. A Lagrangian Finite Element (FE) analysis of compression of a slab under the action of rough platens as shown in Figure 2.8(a) was carried out and slip-line field based on the stress components obtained from FE analysis was generated using MAPLE<sup>TM</sup>. Coulomb friction with a large value for the coefficient

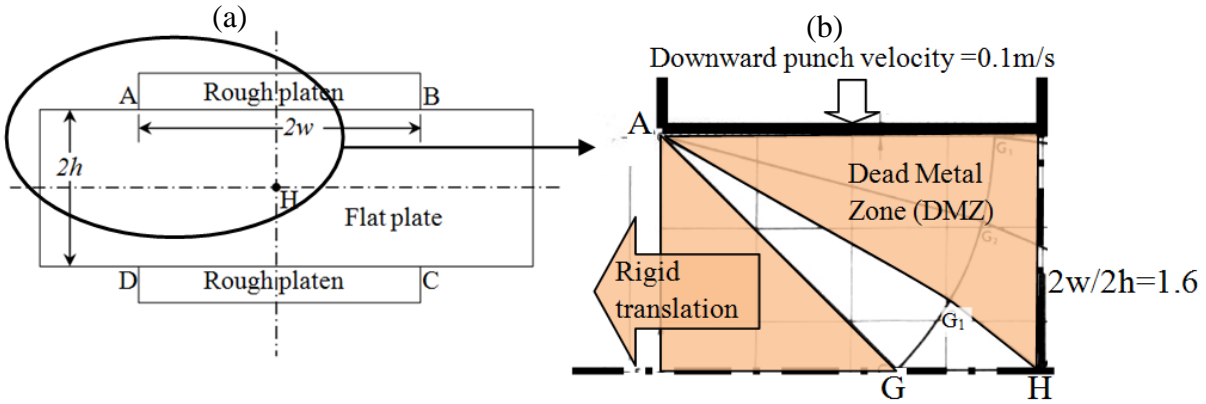


Figure 2.8: (a) Compression of a plate under the action of rough platen and (b) the 15 degree slip-line field provided by Johnson and Mellor for the upper left quarter model with  $2w/2h$  ratio of 1.6 along with the Dead Metal Zones (DMZ). Some part of the figure adopted from Johnson and Mellor (1983)

of friction ( $\mu=20$ ) was used in order to simulate the rough contact between the rough punch and the plate. The punch was displaced by a very small value of  $0.1\mu\text{m}$  compared to the slab height of  $2500\mu\text{m}$ . These SLFs obtained from the FE data were then quantitatively compared with the already available analytical SLF solutions from Johnson and Mellor (1983).

### 2.8 Explanation of the Slip-Line Field

Figure 2.8(b) shows the slip line field solution for the platen width to plate height ratio of

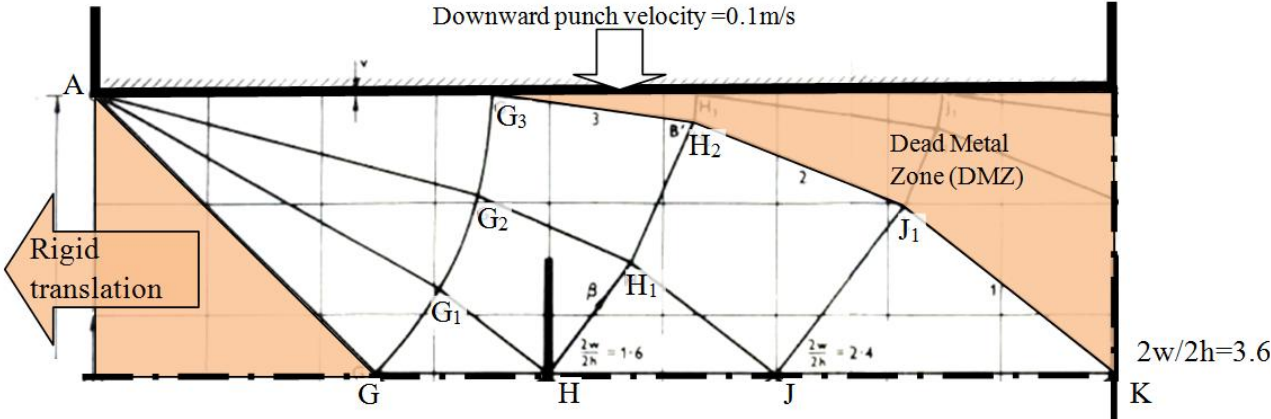


Figure 2.9: The slip-line provided by Johnson and Mellor for the upper left quarter model with  $2w/2h$  ratio of 3.6. The region bounded by alpha slip-line  $AG_3H_2J_1K$  and  $AG$  is the plastically deforming region. The Dead Metal Zones (DMZ) has been identified as the region bounded by slip-line  $G_3H_2J_1K$  on the lower side and some part of the rough punch from above. Some part of the figure adopted from Johnson and Mellor (1983)

1.6. It should be noted that Johnson and Mellor have represented slip-lines by means of straight lines connecting two points. For example, slip-line  $G_1H$  has been drawn as a straight line. This approximation is for the sake of representation only and correct curvatures and change in angles have been accounted in all the calculations. For this ratio, the vertical symmetry line passes through point H. The slip line field is described by the points  $AGG_1$  which is a 15 degree center fan field with the center located at A. The region  $G_1HG$  is the expanding fan field whereas, the region above the alpha slip line  $AG_1H$  is the Dead Metal Zone (DMZ). This DMZ acts like a rigid block attached to the rough platen. Also, the region on the left of the alpha line AG acts as a rigid block and moves to the left as the platen moves vertically downwards.

Figure 2.9 shows the slip line field solution for the platen width to plate height ratio of 3.6. For this ratio, the vertical symmetry line passes through point K. The region bounded by alpha slip-line  $AG_3H_2J_1K$  and AG is the plastically deforming region. The slip-line field described by the points  $AGG_3$  is a center fan field with the center located at A. The region  $GG_1G_2G_3H_2J_1K$  is the expanding fan field. For the  $2w/2h=3.6$  only some part of the punch contact acts as a DMZ

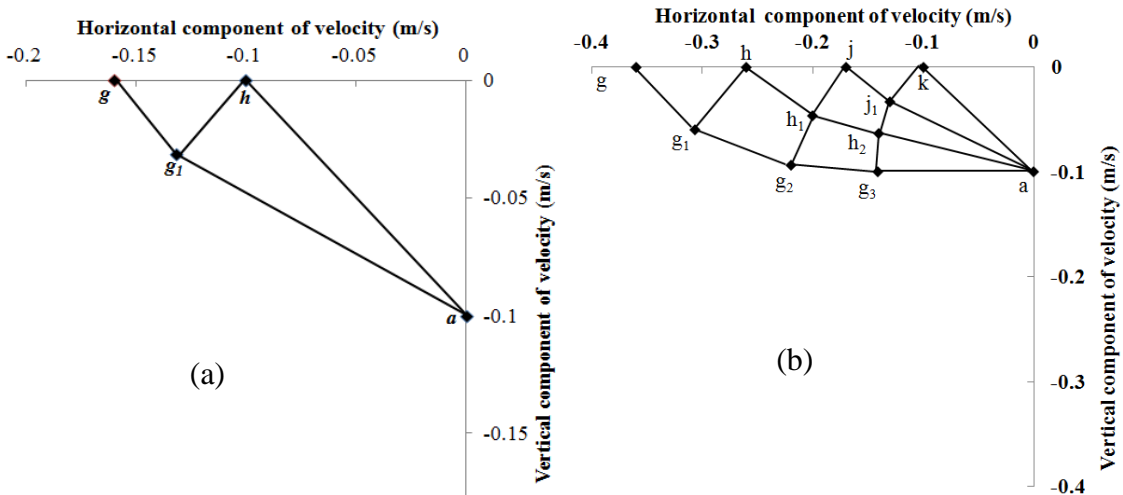


Figure 2.10: The hodograph provided by Johnson and Mellor for the upper left quarter model with (a)  $2w/2h = 1.6$  and (b)  $2w/2h = 3.6$  The figure has been recreated from Johnson and Mellor (1983)

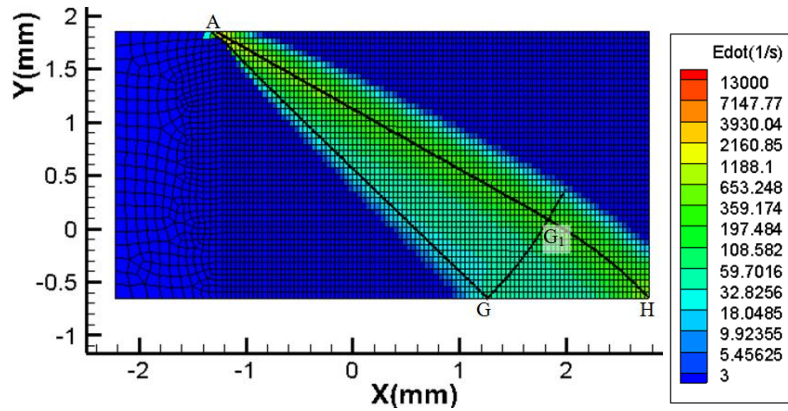


Figure 2.11: The slip-line field obtained based on the results of FE analysis with the mesh not aligned along the slip-lines. The results for  $2w/2h=1.6$

unlike the  $2w/2h = 1.6$  where the entire punch-plate contact was the upper boundary of the DMZ region. Even here, the region on the left of the alpha line AG acts as a rigid block and moves to the left as the platen moves vertically downwards. Figure

2.10 shows the hodograph for the rough punch compression problem for  $2w/2h= 1.6$  and  $2w/2h= 3.6$ .

The compression of a plate under the rough platen was selected for SLF generation approach validation. The top left quarter of the platen and the plated were modeled in Abaqus. The plate was meshed with 2D four noded full integrated plane strain (CPE4) elements and the platen was modeled as a rigid body as shown in Figure 2.7.

A very high value of Young's modulus  $E \geq 210,000$  GPa and the yield strength,  $Y=0.8$  GPa was used to make the elastic strains ( $Y/E \leq 3.81e-6$ ) negligible compared to the plastic strains. A Poisson's ratio of 0.499 was used to make the material incompressible. Thus, the material was made to behave like a rigid plastic material for which the SLF theory is applicable.

Symmetry boundary conditions were applied the right side vertical edge and the bottom of the plate as shown in Figure 2.7. The right edge was constrained in X direction and the bottom of the plate was constrained in the Y direction. The rigid top platen was given a unit velocity in the downward direction. Since the Young's modulus was scaled to a high value, a small platen displacement was enough to produce plastic deformation. The deformation was so small that no change in geometry was observed at the corner 'A' of the platen. Figure 2.11 shows the contours

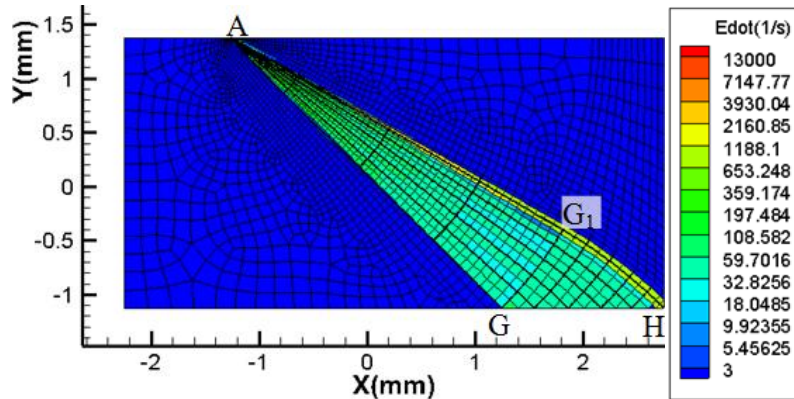


Figure 2.12: The slip-lines generated from a FE simulation for  $2w/2h=1.6$  where the mesh in the plastic region was aligned to the slip-lines. The slip-line geometry from the 1<sup>st</sup> simulation was imported in Abaqus and was used to generate mesh for the 2<sup>nd</sup> simulation.

of strain rate and the slip line field obtained from MAPLE based on the FE simulation results for the simulation with  $2w/2h=1.6$ . Figure 2.15 shows the strain rate distribution and the slip-line field obtained for  $2w/2h=3.6$ . The strain rates were calculated as a difference

in the plastic strains in two output frames divided by the time difference between those two output frames. The geometry of the slip-lines obtained appears to be in close agreement with the slip-line field provided by Johnson and Mellor (1973). A detailed quantitative comparison has been carried out in the Results section.

## 2.9 Effect of Mesh Refinement

From Figure 2.11, it can be observed that the strain rate extends into the Dead Metal Zone (DMZ) along the slip-line  $AG_1H$  (non zero strain rates on the right side of the slip-line  $AG_1H$ ). There exists a velocity discontinuity along the boundary of the DMZ and the plastically deforming region which leads to a very sharp transition in the strain rate values. From the strain rate distributions in Figure 2.11 it can be seen that the region along the discontinuity (boundary of the DMZ) is fairly wide as opposed to an ideal infinitesimal thin plane. The region within the DMZ which is expected to have zero strain rate, has finite strain rate. The finite width of the velocity discontinuity might be attributed to the manner in which the plate is meshed.

As pointed out by various researchers discussed earlier (Steinmann in 1998, Lyamin et. al. in 2003, Sloan in 2008), in order to capture the true width of a discontinuity, the finite element

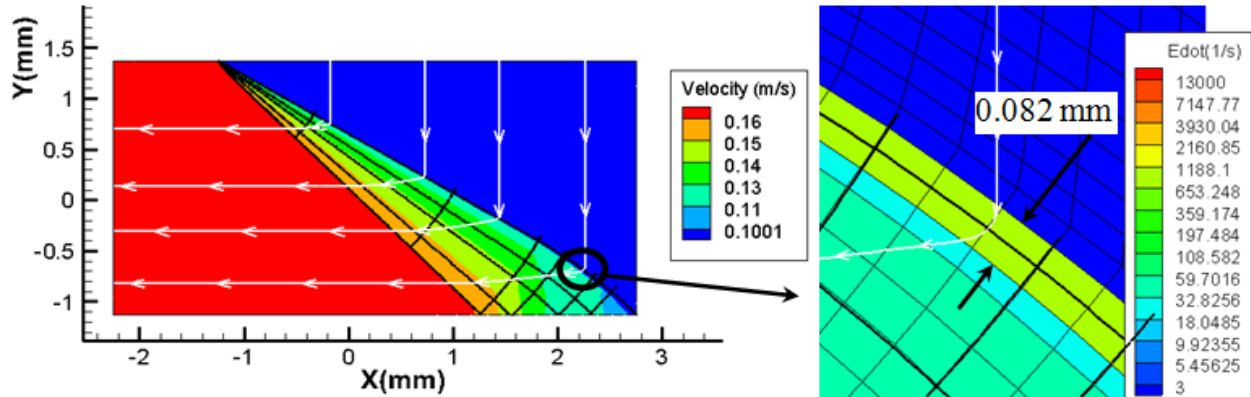


Figure 2.13: Velocity magnitude for the case where  $2w/2h=1.6$ . The black solid lines are the slip-lines and the white lines with arrows are the velocity streamlines. In the inset it can be seen that the velocity discontinuity across the streamline is just 2 element length (0.082mm) wide

mesh has to be aligned to the discontinuity. To check if aligning the mesh would capture the velocity discontinuity, a second FE simulation was carried out in which the mesh was oriented along the slip lines in the plastic region. The geometry of the slip-lines obtained from the 1<sup>st</sup> simulation above was imported in Abaqus and was used to generate a slip-line aligned mesh.

Figure 2.12 shows the FE mesh generated based on the slip-line geometry obtained from the 1<sup>st</sup> simulation and imported in Abaqus along with the new slip-lines computed using the stress

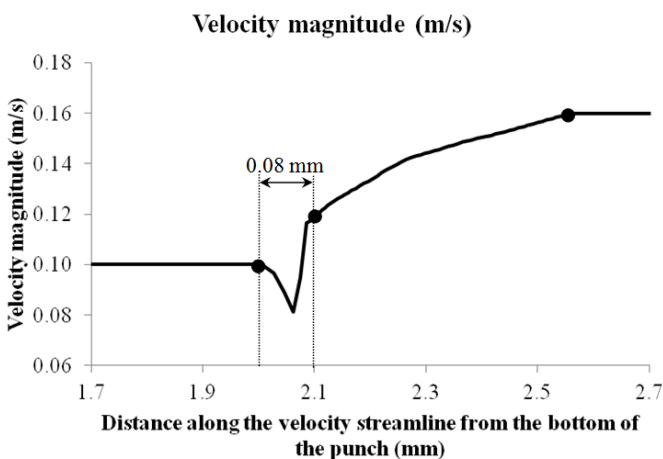


Figure 2.14: The magnitude of velocity was plotted along the velocity streamline shown in the inset in Figure 2.13. The discontinuity in velocity was 0.08mm wide which is same as the length of the 2 elements, one on either side of the slip-line

components obtained from FE analysis with aligned mesh. From Figure 2.12, it can be seen that the boundary of the plastically deforming region and the DMZ is very narrow and extends just one layer of element into the DMZ.

Figure 2.13 shows the contours of velocity magnitude along with the slip-lines (black colored) and the velocity

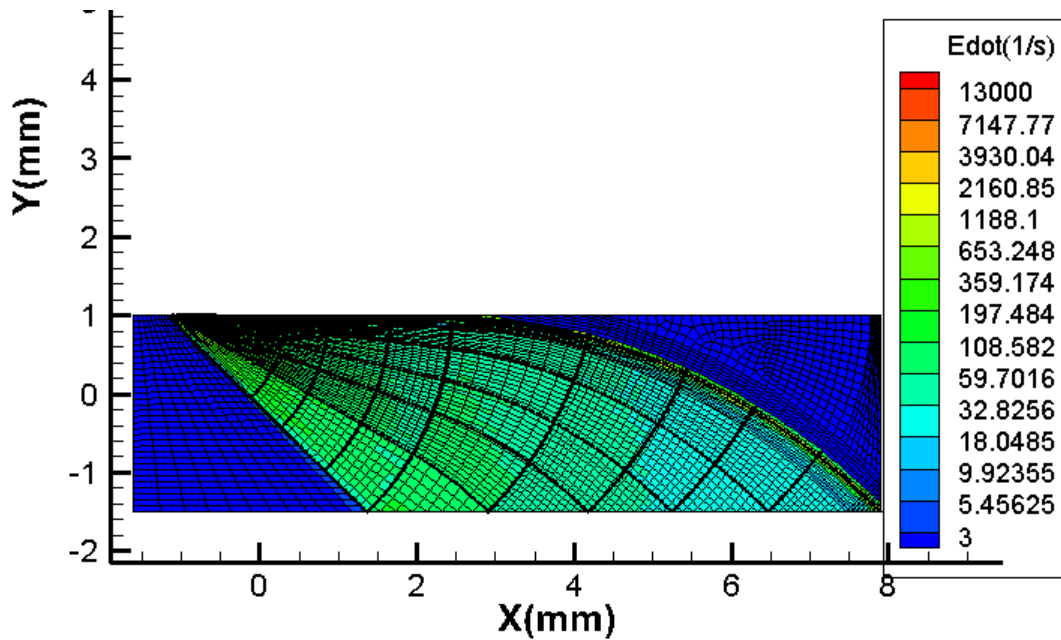


Figure 2.15: The slip-lines generated from a FE simulation for  $2w/2h=3.6$  where the mesh in the plastic region was aligned to the slip-lines. The slip-line geometry from the 1<sup>st</sup> simulation with unaligned mesh was imported in Abaqus and was used to generate mesh for the 2<sup>nd</sup> simulation.

streamlines (white colored with arrows). It can be clearly seen in the inset that the discontinuity of velocity is just 0.082mm which is the width of 2 elements. This can again be verified from the graph of velocity variation plotted along the velocity streamline as shown in Figure 2.14. The velocity has a constant value of 0.1m/s in the DMZ indicating that the material moves downwards with the punch velocity as indicated by Johnson and Mellor. The velocity in the plastically deforming region matches exactly to that computed by Johnson and Mellor. The material exits the plastically deforming zone with a constant sideways velocity of 0.16m/s.

Same treatment was also applied to the simulation with  $2w/2h=3.6$ . The slip-lines generated for aligned mesh are shown in Figure 2.15. Figure 2.16 shows the contours of velocity magnitude along with the slip-lines (black colored) and the velocity streamlines (white colored with arrows). It can be seen in the inset that the strain rate is greater than zero for 2 element lengths within the DMZ instead of just one element length as seen in the previous case for  $2w/2h=1.6$ .

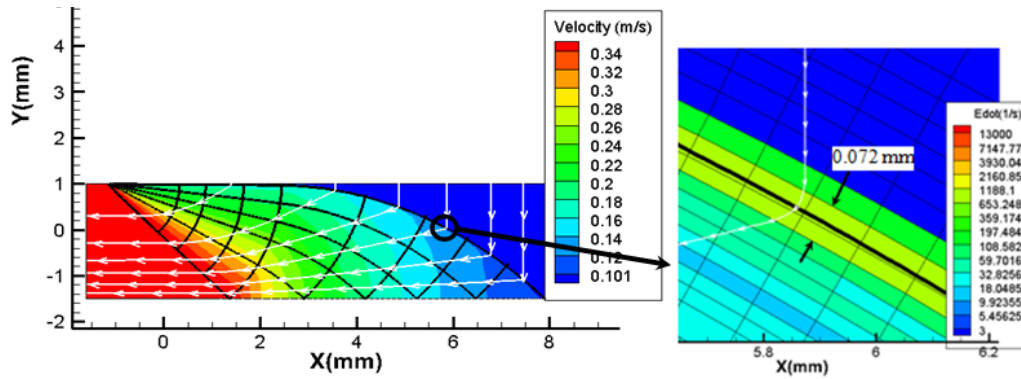


Figure 2.16: Velocity magnitude for the case where  $2w/2h=3.6$ . The black solid lines are the slip-lines and the white lines with arrows are the velocity streamlines. In the inset it can be seen that the velocity discontinuity across the streamline is just 2 element length (0.072mm) wide

This is attributed to the fact that the slip-line shown in the inset for this case has a slight misalignment with the mesh which can be seen in the inset in Figure 2.16. It is due to this small misalignment that there is strain rate in one additional element row in the DMZ. The width of the velocity discontinuity obtained by plotting the velocity along that streamline is found to be 0.104 mm which is slightly more than the width of 2 elements as shown in Figure 2.17. The velocity has a constant value of 0.1m/s in the DMZ indicating that the material moves downwards with the punch velocity as indicated by Johnson and Mellor. After the velocity discontinuity, the velocity again matches exactly to that computed by Johnson and Mellor in the plastically deforming region. The material exits the plastically deforming zone with a constant sideways velocity of 0.36m/s. Thus, it should be noted that aligning the mesh with the discontinuity is extremely important in capturing the correct width of the discontinuity.

## 2.10 Effect of Mesh Size

In order to check if the velocity discontinuity can indeed be captured within 2 elements and doesn't depend on the mesh size, yet another simulation with aligned mesh, but finer element size along the boundary of the discontinuity was carried out for  $2w/2h=1.6$  case. In this simulation, the boundaries of the discontinuities were more finely meshed as shown in Figure 2.18. In this third

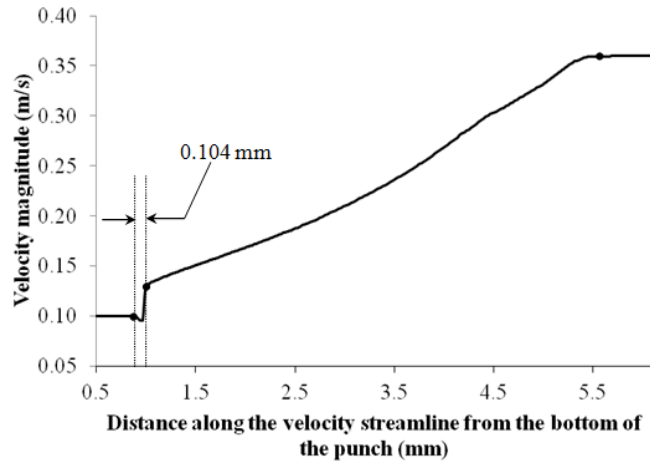


Figure 2.17: The magnitude of velocity was plotted along the velocity streamline shown in the inset in Figure 2.16. The discontinuity in velocity was 0.104mm wide which is slightly more than the width of Figure 2.12.

It can be seen that the width of the discontinuity further decreases as the mesh size decreases and the mesh becomes finer. Thus, the discontinuity is always two elements wide irrespective of the size of the mesh. Figure 2.19 shows the plot of strain rate across the

simulation, the width of the elements along the boundary was  $1/8^{\text{th}}$  of the width of the boundary elements in the second simulation. As can be seen from Figure 2.18, the discontinuity is again two elements wide. Note that, even for Figure 2.18, the contour range of strain rate is same as that in Figure 2.11 and Figure 2.12.

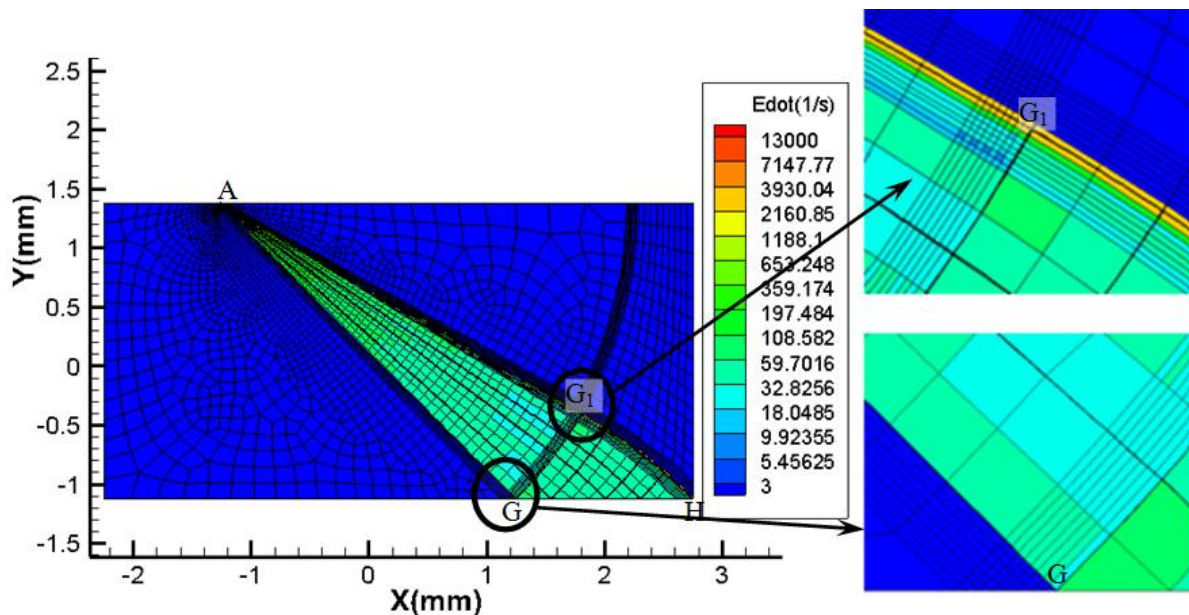


Figure 2.18: A third simulation with aligned mesh was carried out. The boundaries of the discontinuity were mesh much finer compared to the 2<sup>nd</sup> simulation, to make sure that the discontinuity is always 2 elements wide. The fine mesh can be seen clearly in the inset pictures of the mesh near the points  $G$  and  $G_1$ .

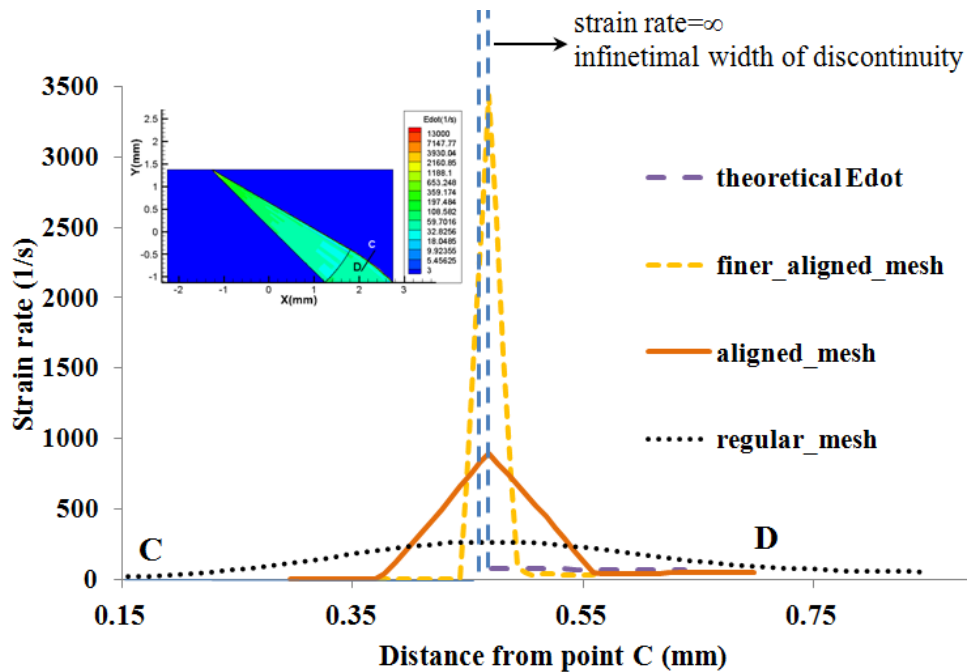


Figure 2.19: The graph of strain rate variation was plotted along the line CD. The bell shaped distribution of the strain rate shows that the actual width of the velocity discontinuity is finite and the value of peak strain rate is also finite. The dotted black line in the graph shows the expected infinitesimal width of discontinuity with infinite peak strain rate

discontinuity. The strain rates were plotted along line CD (shown in the inset) for the simulation with regular mesh, aligned mesh, and aligned mesh with finer elements. The theoretical strain rate distribution which, has infinitesimal width where the strain rate are infinity, has been superimposed on the plot. It can be seen that although the width of discontinuity is always two elements wide, the strain rate distribution approaches theoretical value as the element size decreases.

## 2.11 Verification of the Achievement of Steady Deformation Field

In order to verify whether the deformation obtained from the FE simulations is steady in nature, the punch reaction forces were plotted as a function of time. Figure 2.22 (a) and Figure 2.22 (b) show the punch reaction force components in X and Y direction for  $2w/2h=1.6$  and  $2w/2h=3.6$  respectively. It can be seen that both the components of force reach a constant value in

a very short amount of punch displacement and remain constant thereafter indicating that the steady state deformation has been achieved.

Another check for stability would be to plot the strain rate and velocity at different times during the simulation. Figure 2.20 and Figure 2.21 which are for  $2w/2h$  ratios of 1.6 and 3.6 respectively, show that the strain rates ( $a_1, a_2, a_3$ ) and velocities ( $b_1, b_2, b_3$ ) are constant throughout the simulation. Note that the fringe ranges is same for all the velocity plots as well as same for all the strain rate plots.

### 2.12 Check for Elastic Effects

In order to apply the slip-line field theory, the material was made to behave like a rigid plastic material by scaling the Young's modulus to a very high value and making Poisson's ratio equal to 0.499. Scaling the Young's modulus to a large value significantly reduced the elastic strain ( $Y/E= 3.8e-7$ ). In order to check if the material shows rigid plastic behavior i.e. the plastic strains are significantly higher than the elastic strains, the ratio of equivalent plastic strain to maximum principal elastic strains was calculated. Figure 2.23 (a) to (d) show the ratio of

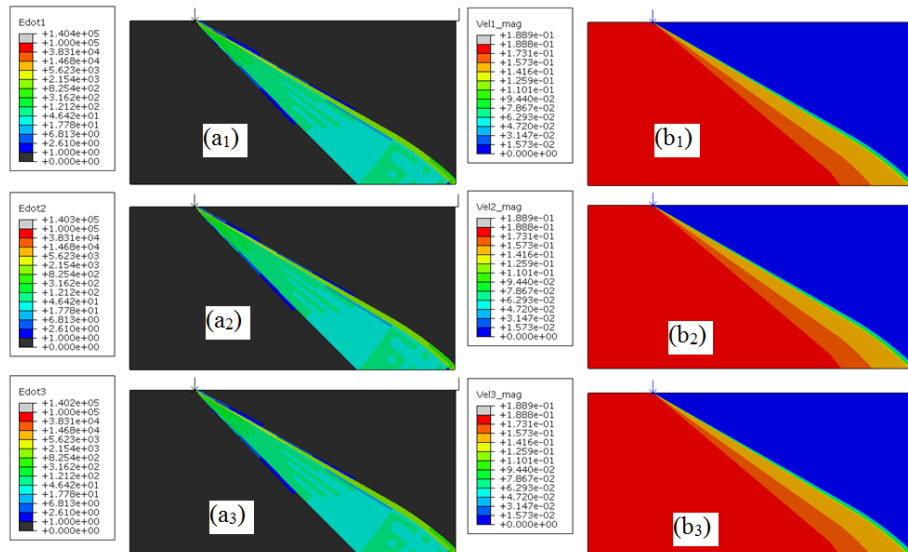


Figure 2.20: The strain rates ( $a_1, a_2, a_3$ ) and velocities ( $b_1, b_2, b_3$ ) were calculated at different time instances during the simulation to check if they are constant for  $2w/2h=1.6$

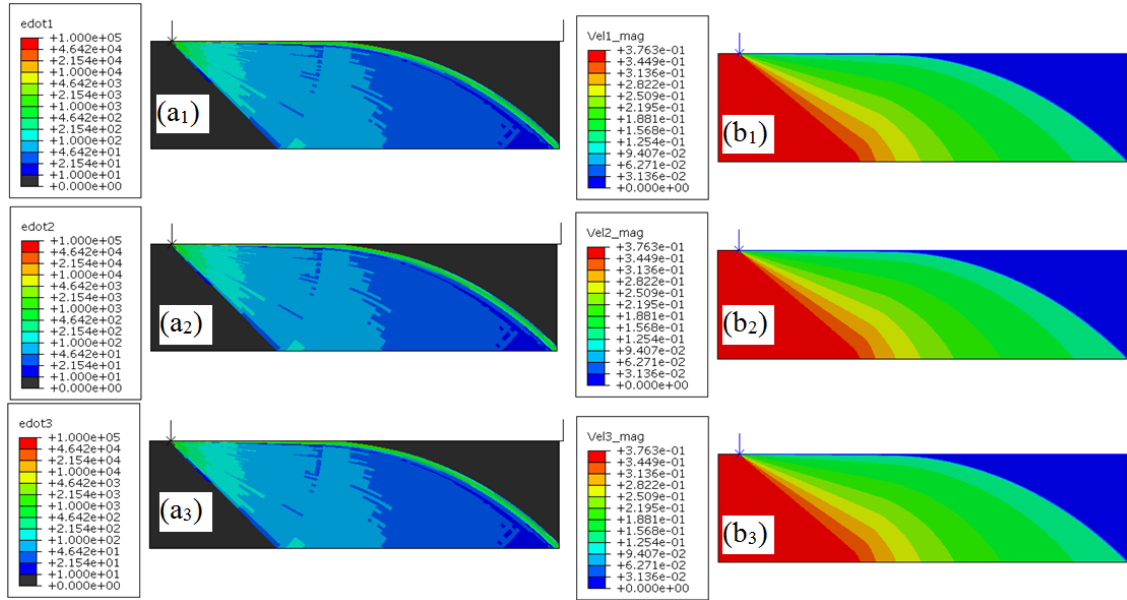
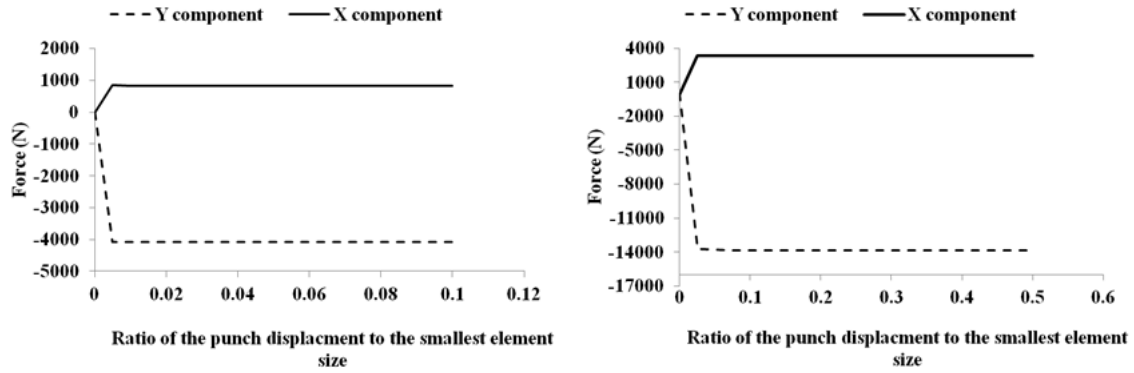


Figure 2.21: The strain rates ( $a_1$ ,  $a_2$ ,  $a_3$ ) and velocities ( $b_1$ ,  $b_2$ ,  $b_3$ ) were calculated at different time instances during the simulation to check if they are constant for  $2w/2h=3.6$

equivalent plastic strain to maximum principal elastic strains for  $2w/2h=1.6$ . The different figures are plotted for different lower values of the fringe range (1, 10, 50, 100 corresponding to figures (a), (b), (c), and (d)) in order to view the regions which act as rigid plastic. From Figure 2.23(d) it can be seen that in the region of interest i.e. the region of plastic deformation, the plastic strains are about 100 times greater than the elastic strain. Since the elastic strain is significantly small, the rigid plastic material behavior assumption is valid and slip-line field theory can be implemented.

### 2.13 Satisfaction of Hencky's Equations

The equations shown in equation 2 are the equilibrium equations, which were put forth by Hencky (1923). Based on the orientation angle ( $\phi$ ) of the alpha line with  $X$  axis, the quantities  $(p+2k\phi)$  and  $(p-2k\phi)$  where ' $p$ ' is the hydrostatic pressure and ' $k$ ' is the shear stress, were calculated in TECPLOT. Within the plastic region, it is expected that the quantities  $(p+2k\phi)$  and  $(p-2k\phi)$  will have constant values along the  $\alpha$  and the  $\beta$  lines respectively. The plots in Figure



(a) (b)

Figure 2.22: The X force (sideways) and Y force (in the direction of the punch motion) components plotted with respect to the punch displacement for width to plate height ratio of (a) 1.6 and (b) 3.6, show that the forces are constant which indicate the achievement of the steady state deformation.

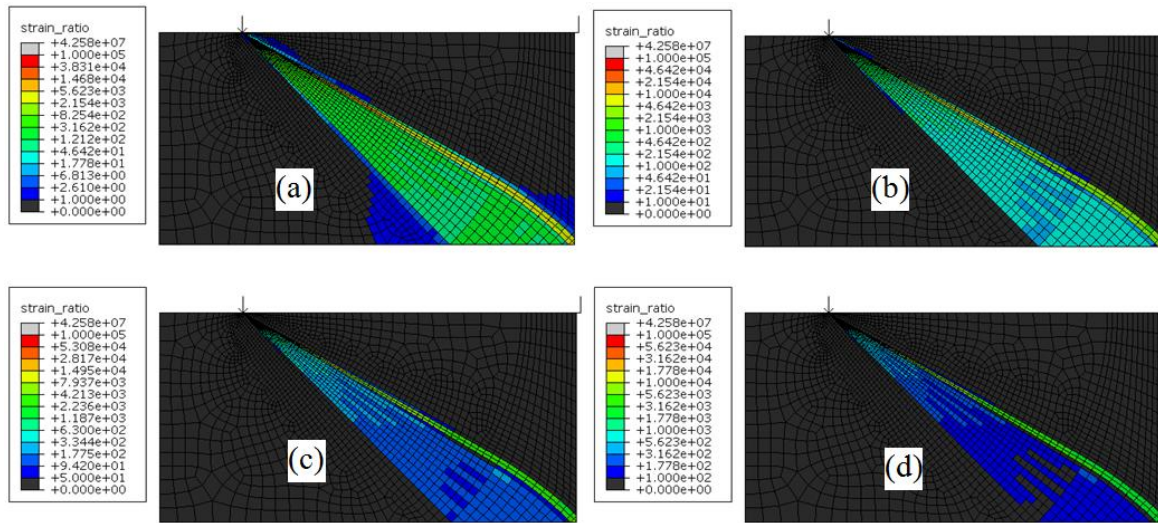


Figure 2.23: The absolute value of the ratio of the equivalent plastic strain to the maximum elastic strain was calculated. (a) The region where the absolute value of the ratio is greater than one, (b) The region where the absolute value of the ratio is greater than ten, (c) The region where the absolute value of the ratio is greater than fifty, and (d) The region where the absolute value of the ratio is greater than hundred.

2.24(a) and (b) are for quantities  $(p+2k\phi)$  and  $(p-2k\phi)$  respectively for  $2w/2h=3.6$ , show that although the value of these terms vary from one slip-line of the same family to another slip-line of the same family, they are indeed constant along one slip-line.

## 2.14 Comparison of Radii of Curvatures and Velocities with Analytical Calculations

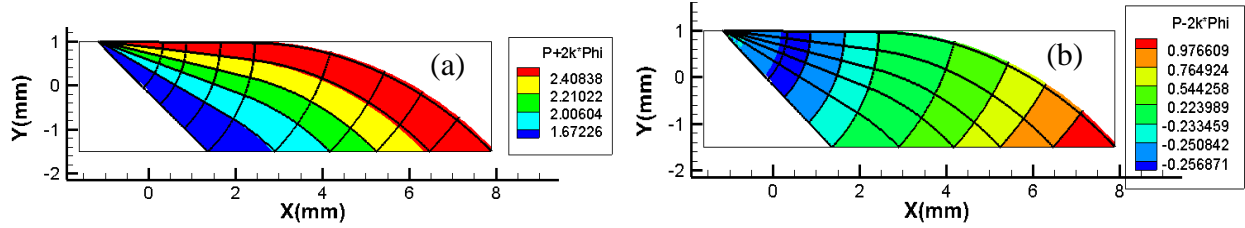


Figure 2.24: The plots verifying that Hencky's equations are modified by the sliplines generated from FEA (a)  $(p+2k\phi)$  being constant along the alpha slip-lines and (b)  $(p-2k\phi)$  being constant along the beta slip-lines for the flat punch simulation with  $2w/2h=3.6$  for terms in the Hencky's equations. It should be noted that since these quantities are valid only within the plastic region, only the region with strain rate greater than  $3/s$  (a very small value) has been plotted.

The radii of curvatures  $R$  and  $S$  of the alpha and beta sliplines respectively, were calculated using equation 8 and equation 9 shown below. The calculations of gradients for the FE simulation data were carried out using Tecplot. The global  $X$  and  $Y$  components of velocity  $(u_x, u_y)$  were transformed in to the components along the slipline directions  $(u, v)$ .

$$\frac{1}{R} = \frac{\partial\phi}{\partial s_\alpha} \equiv \left( \frac{\partial\phi}{\partial x} * \cos\phi + \frac{\partial\phi}{\partial y} * \sin\phi \right) \quad (8)$$

$$\frac{1}{S} = -\frac{\partial\phi}{\partial s_\beta} \equiv \left( -\frac{\partial\phi}{\partial x} * \sin\phi + \frac{\partial\phi}{\partial y} * \cos\phi \right) \quad (9)$$

In order to check the accuracy of the velocity components as well as the radii of curvatures obtained from FE data, a slipline field for the extended fan field region was obtained analytically in Maple, using equations 8 and 9 specified in Johnson and Mellor (1973). The punch velocity in the analytical calculations same as the punch velocity used in FE simulations. The velocity components as well as the radii of curvatures calculations were repeated for the analytically calculated slipline field. A detailed comparison between the values obtained from FEA and analytical calculations was carried out for radii of curvatures as well as the velocity components as shown in Table 2.1 only for the extended fan field region  $GG_1H$  of Figure 2.8. It can be seen from Table 2.1 that the velocity components 'u' and 'v' obtained from FEA are in a very close agreement with the values obtained from analytical calculations, indicating that the velocity field

Table 2.1: The velocity components ( $u$  and  $v$ ) along the slip-line directions, the angle ' $\phi$ ' made by the alpha line with X axis, and the radii of curvatures ( $R$  and  $S$ ) of the alpha and beta slip-lines obtained from FEA were compared with the corresponding quantities calculated analytically using MAPLE.

Variable	FE data	Analytically calculated values from MAPLE
velocity component along the alpha lines ' $u$ ' (m/s)		
velocity component along the beta lines ' $v$ ' (m/s)		
The angle made by the alpha line with the X axis ' $\phi$ ' (radians)		
Radius of curvature of the alpha line ' $R$ ' (mm)		
Radius of curvature of the beta line ' $S$ ' (mm)		

obtained from FEA is correct. However, the values of radii of curvatures ( $R$  and  $S$ ) obtained from FEA were significantly different from the values obtained from analytical calculations.

It was thought that the calculations of the gradients in Tecplot is affected by the presence of discontinuity along the boundary of the DMZ. The gradients of  $\phi$  had a very large value along

this discontinuity, which affected the curvature values in this region. The calculations of curvatures for the FEA data in Tecplot were then repeated by considering only the interior region of the extended fan field. These results are reported in Table 2.1 and it is clear that the agreement between analytical calculations and FEA is not very satisfactory. Several other options were tried to improve the results obtained from FEA and have been summarized in Table 2.2.

Extra layer of elements were included in the Maple calculations which didn't help. A new simulation with half model of the compression problem was carried out without significant improvement in R and S. The half model simulation with 100X displacement of the punch compared to the previous simulation was also carried out. This would increase the plastic strain in the extended fan field region which would increasing the ratio of plastic strain to the elastic strain to be much higher than previously reported value of 100.

Both the half model simulations showed some improvement in R and S but only in the region of the symmetry boundary (bottom boundary). This set of results is reported in Table 2.2 and it can be seen that the results of curvature calculations are still not in agreement with the analytically calculated values.

### 2.15 Satisfaction of Geiringer's Equations

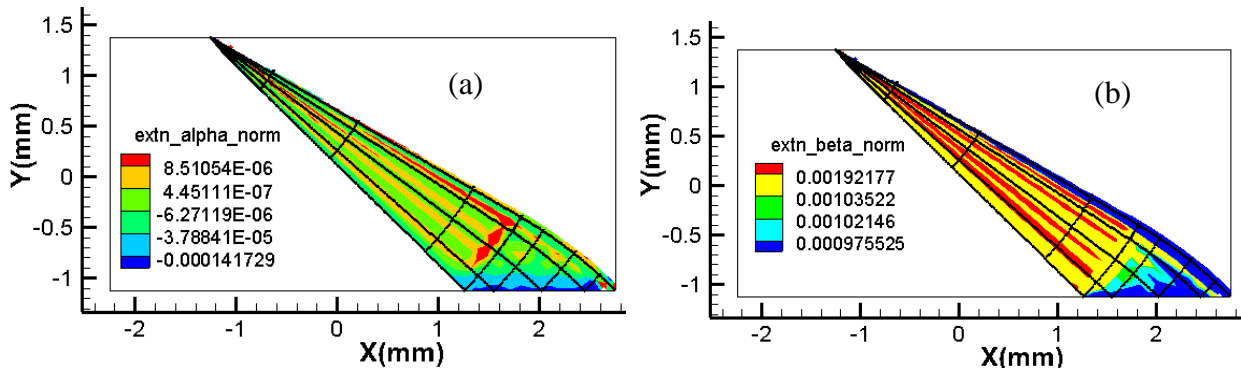


Figure 2.25: Extension along (a) alpha sliplines and (b) beta sliplines were plotted according to equation 8 and 9 respectively. The values were normalized by dividing them with the plastic strain rate and were found to be zero indicating that the Geiringer's equations are satisfied.

The velocity components in the global  $X$  and  $Y$  directions were transformed into the slip-line coordinate system, where ‘ $u$ ’ is the component of velocity in the direction of  $\alpha$  slip-line and ‘ $v$ ’ is the component of velocity in the direction of  $\beta$  slip-line, using equation 3. Further equation 4 was simplified in terms of partial derivatives of velocity components ‘ $u$ ’ and ‘ $v$ ’ with respect to the global  $X$  and  $Y$  directions as shown in equation 8 and equation 9 within TECPLOT.

$$du - vd\phi \equiv \frac{du}{d\phi} - v \equiv \frac{du}{Rd\phi} - \frac{v}{R} \equiv \frac{du}{ds_\alpha} - \frac{v}{R} \equiv \left( \frac{\partial u}{\partial x} \cos \phi + \frac{\partial u}{\partial y} \sin \phi \right) - \frac{v}{R} = 0 \quad (10)$$

$$dv + ud\phi \equiv \frac{dv}{d\phi} + u \equiv \frac{dv}{sd\phi} + \frac{u}{s} \equiv \frac{dv}{ds_\beta} + \frac{u}{s} \equiv \left( -\frac{\partial v}{\partial x} \sin \phi + \frac{\partial v}{\partial y} \cos \phi \right) + \frac{u}{s} = 0 \quad (11)$$

Since slip-lines can be drawn at any location in the plastically deforming region, it implies that the Geiringer equations should be valid at every point in the plastic region. Figure 2.25 shows that at every point in the plastic region, the value of Geiringer’s equations is almost zero for  $2w/2h=1.6$  case.

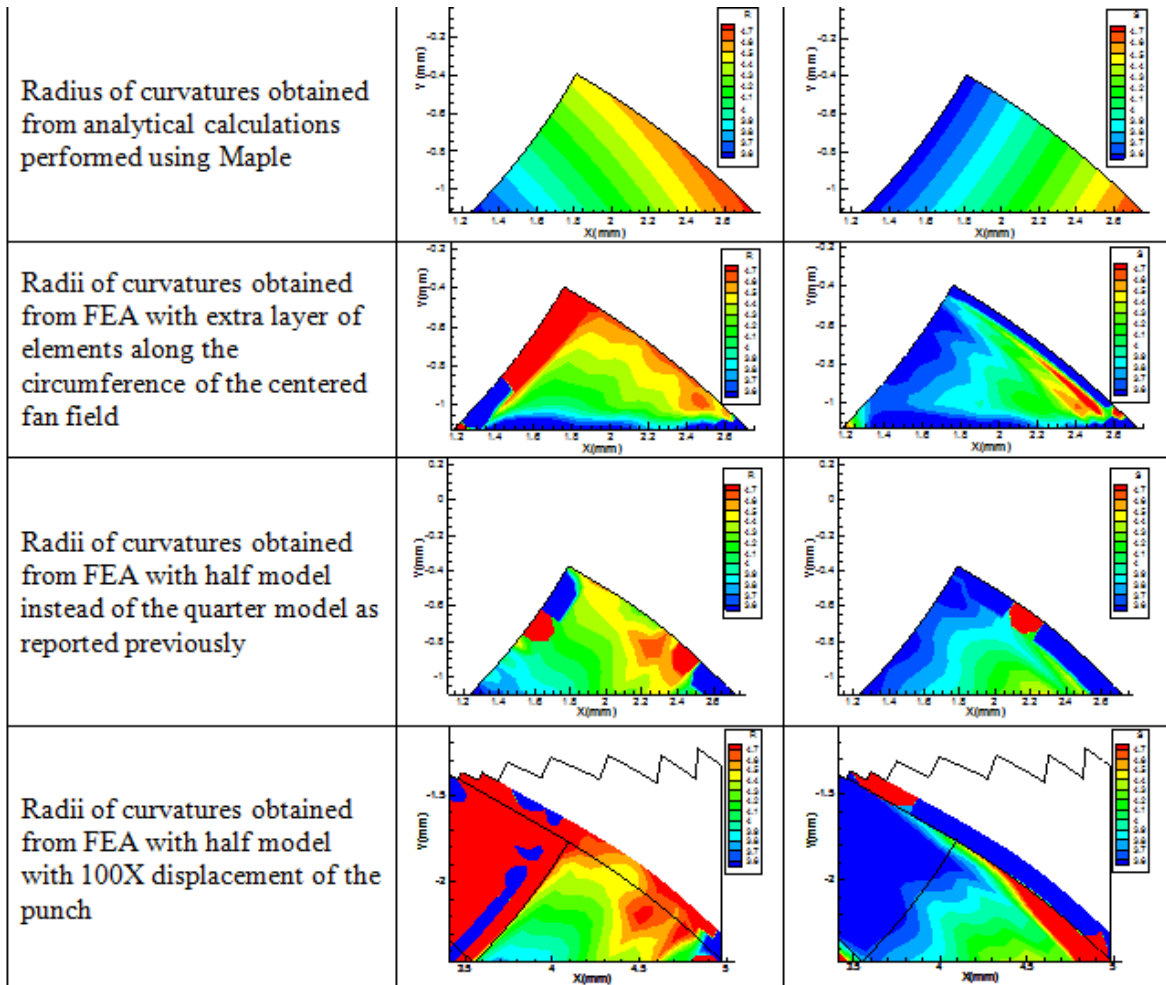
## 2.16 Comparison of the Shear Strain Rate Obtained from FEA with Analytical Calculations

The strain rate comprises of four terms as shown in equation 10 below. Each of the four terms from equation 10 was calculated for the slipline field obtained from FE simulation as well as for the slipline field obtained from analytically from Maple.

$$\dot{\gamma} = \frac{du}{ds_\beta} + \frac{dv}{ds_\alpha} + \frac{u}{R} + \frac{v}{s} \quad (12)$$

A comparison between each of the four terms was carried out separately as shown in Table 2 for  $2w/2h=1.6$ . It can be seen from Table 2.3 that the agreement of each of the four strain rate terms from FEA with their analytically calculated counterparts is good in the interior of the extended fan field region. Whereas, the FEA based results show significant noise along the boundary of the region. This is similar to the observations for ‘R’ and ‘S.’ This can be attributed to the manner in which Tecplot calculates the gradients. Further, in order to make sure that the

Table 2.2: Different option evaluated in FEA, in order to match the radii of curvature values obtained from analytical calculations using Maple and their outcomes are summarized below. Only the extended fan field region GG<sub>1</sub>H from Figure 7 has been considered.



four terms of shear strain rate obtained based on the FE results are correct, the shear strain rate which is the sum of these four terms was compared with the shear strain rate obtained as plastic strain increment divided by the time increment from the FE simulation. Figure 2.26 compares these two shear strain rates obtained from the same FE results but in different manner. There is excellent agreement in the two values suggesting that the shear strain rate calculated as the sum of the four terms are correct inspite of the noisy values of R and S.

## 2.17 Discussion

A detailed evaluation of the slipline field obtained based on the FE results was carried out. The slipline field theory is applicable only for rigid perfectly plastic material under conditions of plane strain. The rigid perfectly plastic material was simulated by increasing the Young's modulus by a factor  $>1000$  and the material was made incompressible by increasing the Poisson's ratio to 0.499. The ratio of plastic strain to elastic strain was found to be greater than 100 in the plastically deforming region indicating that the material approximations are reasonable. Further, the achievement of steady state deformation field was verified by plotting the reaction forces as a function of the punch displacement. Also, the velocity and the strain rate at different punch displacements were plotted and found to be exactly the same indicating achievement of steady state. The newly generated slipline field satisfied Hencky's equations as well as Geiringer's equations. Once the mesh was oriented along the sliplines, the discontinuity along the boundary of the DMZ was captured within the width of two elements.

Output variables like velocity, reaction forces, and contact stresses are predicted correctly by the new slipline field. However, variables which were obtained by calculating gradients, end

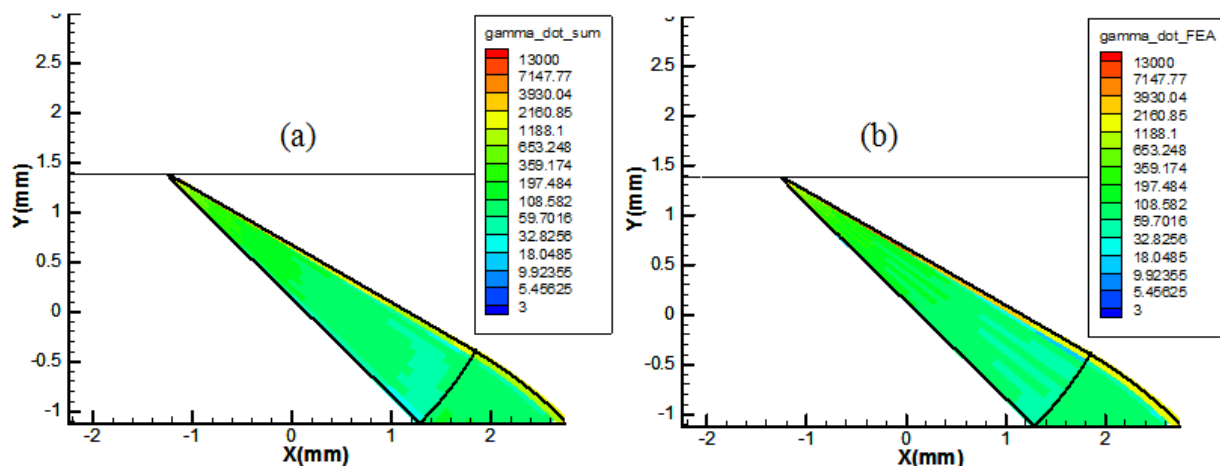
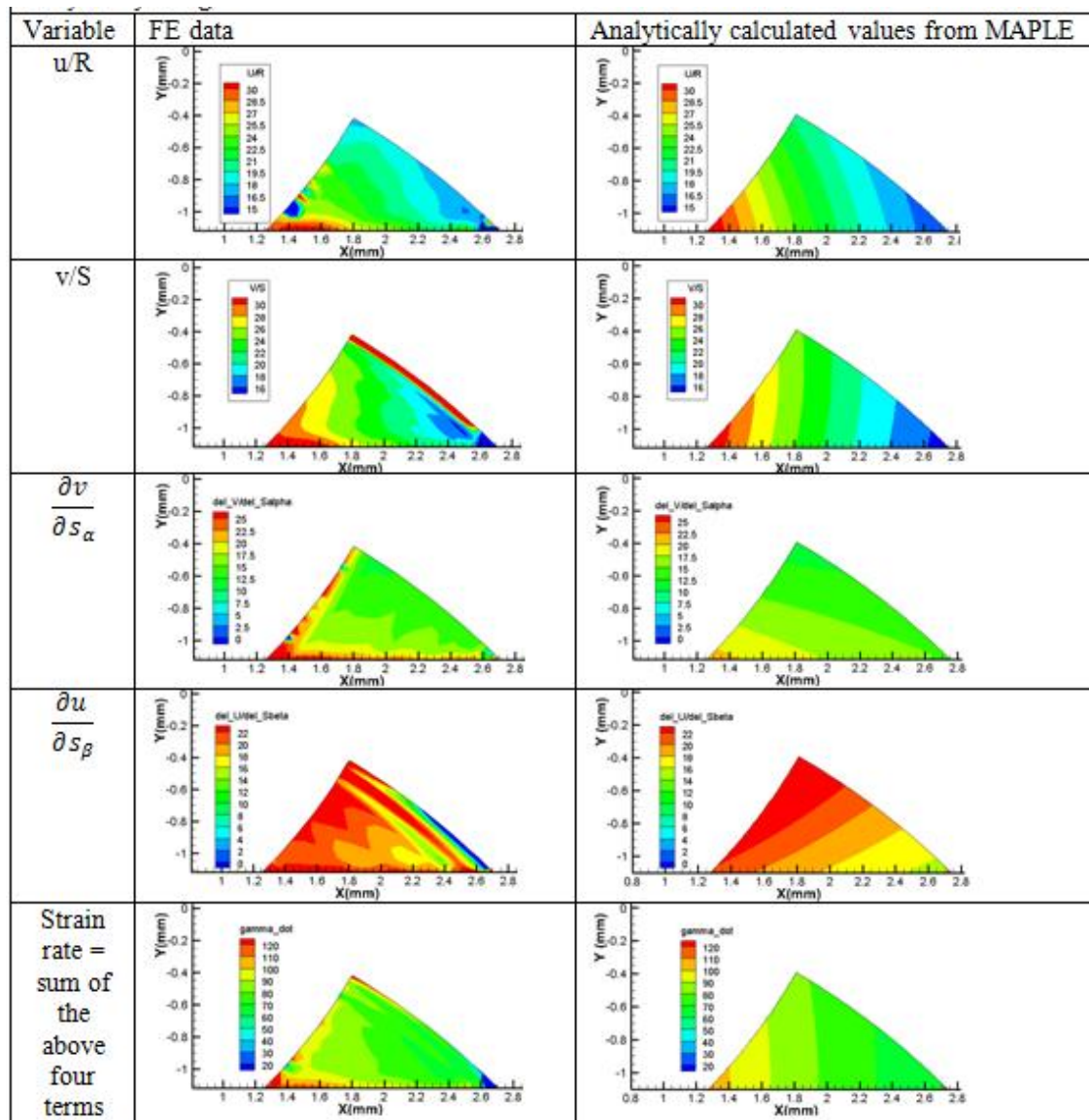


Figure 2.26: The shear strain rate calculated as (a) sum of the four terms in equation 12 were compared with shear strain rate calculated (b) directly from FEA as the strain increment between two frames divided by the time interval between those two frames. Both the strain rates calculations show excellent agreement

Table 2.3: The four terms ( $u/R$ ,  $v/S$ ,  $\frac{\partial v}{\partial s_\alpha}$ ,  $\frac{\partial u}{\partial s_\beta}$ ) which contribute to the shear strain rate were obtained from the FEA results and were compared with the corresponding quantities calculated analytically using MAPLE



up being not in good agreement with the analytically obtained values. This can be attributed to the manner in which Tecplot calculated the gradients. They are satisfied by the slipline field generated based on FE results.

## 2.18 Conclusion

A novel method to obtain accurate slip-line field based on the exact aligned mesh using the stress components of FE analysis was developed. The validation of this novel method was carried out with the help of a rough punch compression problem. The geometry of the slip-lines generated with the new method matched exactly with those given in the literature. The Hencky's equations as well as the Geiringer's equations were also found to be satisfied in the entire plastic deformation region. The rigid plastic approximation implemented by scaling the Young's modulus of the material was thoroughly validated. An iterative refinement of the mesh was carried out in order to obtain the exact boundaries of the DMZ and capture the velocity discontinuities accurately. Based on the results of simulations with aligned mesh, it was found that the reaction force on the punch and the contact pressure distribution are accurate even with the homogeneous mesh pattern. However, the most significant finding was that the accurate estimation of the boundaries of the dead metal zone which are nothing but velocity discontinuities is only possible with the exact alignment of the mesh and the discontinuity. This is very important for problems with complex slip-line field like that of metal cutting where it is necessary to obtain the exact width of the primary shear zone (PSZ) and the boundaries of the dead metal zone. The exact estimation of the shear stress in the PSZ is possible only when the exact geometry of the PSZ is known. The obtained shear stress can then be used to develop the constitutive material models.

## **2.19 Acknowledgement**

This material is based upon work supported by the National Science Foundation under grant number EIA-0216178 and grant number EPS-0236913, matching support from the State of Kansas and the Wichita State University High Performance Computing Center. NSF support under grant number DMI-0621174 is also acknowledged.

## **2.20 References**

Borges L., Zouain N., Costa C., Feijöo R., 2001, "An adaptive approach to limit analysis", *International Journal of Solids and Structures*, v 38, pp 1707-1720.

Collins I. F., 2011, "The Algebraic-Geometry of Slip Line Fields with Applications to Boundary Value Problems," *Proceedings of the Royal Society of London, Series A: Mathematical and Physical Sciences*, v 303, n 1474, pp 317-338.

Deb A., Prevosta J.H., Loretb B., 1996, "Adaptive meshing for dynamic strain localization," *Computational Methods in Applied Mechanics and Engineering*, v137, pp 285-306.

Dewhurst P. and Collins, I. F., 1973, "A Matrix Technique for Constructing Slip-Line Field Solutions to a Class of Plane Strain Plasticity Problems," *International Journal of Numerical Methods in Engineering*, v 7, pp 357-378.

Dewhurst P., 1978, "On the Non-Uniqueness of the Machining Process," *Proceeding of the Royal Society of London, Series A: Mathematical and Physical Sciences*, v 360, n 1703, pp 587-610.

Ewing D. J. F., 1967, "A Series-Method for Constructing Plastic Slipline Fields," *Journal of Mechanics and Physics of Solids*, v 15, pp 105-114.

Fang N., 2003, "Slip-Line Modeling of Machining with a Rounded-Edge Tool Part I: New Model and Theory," *Journal of Mechanics and Physics of Solids*, v 51, pp 715-742.

Geiringer H., 1937, "Memorial des Sciences Mathanmatiques, 86, Paris: Gauthier-Villars.

Hencky H., 1923, "Über Einige Statisch Bestimmte Fälle Des Gleichgewichts In Plastischen Körpern," *Zeitschrift für Angewandte Mathematik und Mechanik*, v3, n4, pp 241-251

Hill R., 1950, "The Mathematical Theory of Plasticity," Clarendon Press, Oxford.

Hill R., 1954, "On the Limits Set by Plastic Yielding to the Intensity of Singularities of Stress," *Journal of Mechanics and Physics of Solids*, v 2, pp 278-285.

Hill R., 1954, "The Mechanics of Machining: A New Approach," *Journal of Mechanics and Physics of Solids*, v 3, pp 47-58.

Johnson W., Mellor P.B., 1983, "Engineering plasticity," Ellis Horwood

Johnson W., Sowerby R., and Venter R. D., 1992, "Plane-Strain Slip-Line Fields for Metal-Deformation Processes-A Source Book and Bibliography," Pergamon Press, Oxford.

Lyamin A.V., Sloan S.W., Krabbenhöft K., and Hjjaj M., 2005, "Lower bound limit analysis with adaptive remeshing," *International Jouranal for Numerical methods in Edngineering*, v 63, pp 1961-1974.

Ortiz M., Quigley IV J.J., 1991, "Adaptive mesh refinement in strain localization problems," *Computer Methods in Applied Mechanics and Engineering*, v 90, pp 781-804.

Petryk H., 1987, "Slip Line Field Solutions for Sliding Contact," *Proceedings of International Conference on Tribology - Friction, Lubrication and Wear Fifty Years On*, pp 987-994.

Regueiro R.A., Borja R.I., 1999, "A finite element model of localized deformation in frictional materials taking a strong discontinuity approach," *Finite Elements in Analysis and Design*, v 33, pp 283-315.

Shaw M. C., 2005, "Metal Cutting Principles," Oxford University Press, New York.

J.C. Simo, J. Oliver, F. Armero, An analysis of strong discontinuities induced by strain-softening in rate independent inelastic solids, *Comput. Mech.* 12 (1993) 277-296.

Sloan S.W., 2008, "Limit Analysis With Adaptive Mesh Refinement," 8<sup>th</sup> World Congress on Computational Mechanics (WCCM8)

Toulios M., and Collins I. F., 1982, "A Technique for Calculating the Continued Deformation of a Class of Slip Line Field Solutions," *International Journal of Mechanical Sciences*, v 24, n2, pp 61-72.

## CHAPTER 3

### UNDERSTANDING THE PRESSURES IN MACHINING WITH ANALOGY TO FLAT PUNCH INDENTATION

#### 3.1 Abstract

The analogy between machining and indentation has been utilized to understand the distribution of pressure along the finite cutting edge in metal cutting. Based on the results of the flat punch indentation simulations, it has been shown that for confinement ratios below the critical value, the Prandtl's flat punch indentation slip-line field changes to a 'S' shaped shear plane field similar to the one observed in machining. Also, the contact pressure was observed to decrease once the 'S' shaped shear plane was formed and the plastic deformation reached to the sides of the workpiece rather than the top of the workpiece. This critical ratio of confinement was found to be 8.75 from the flat punch simulations as opposed to the value of 8.593 provided in the literature. Further, a simulation with punch inclined by a very small angle of  $0.05^\circ$  was carried out to check if the critical value of confinement ratio would be closer to the theoretical value of 8.593. Indeed, with a very small inclination, the critical value of the confinement ratio was found to be  $8.59 \pm 0.05$ . The difference in the critical confinement ratio obtained from the flat punch and the wedge indentation was due to the singularity of stress at the sharp corner of the punch in case of flat punch indentation. In metal cutting, the contact length is significantly higher than the uncut chip thickness making the confinement ratio less than one. Since the confinement ratio is very small, significant deformation happens in the shear plane. This is also the reason for lower pressure observed at the cutting tool tip compared to the indentation process.

*Keywords:* FEA; slip-line field, confinement; indentation; machining

#### 3.2 Introduction

Slip-line field theory has evolved as a tool to analyze plane strain problems which have non homogeneous deformations in rigid perfectly plastic isotropic solids. It doesn't take into account the strain hardening, the strain rate effects, or the temperatures effects which cause change in the material properties (Hill, 1950). The idealizations of rigid perfectly plastic solids, although very far from realistic material behavior, give a very good starting point to obtain loads at yielding as well as help in better understanding the observed deformation patterns. In the conventional slip-line field solution approach, the slip-line field solution is proposed first. Later, it is shown that the solution is able to satisfy all the boundary conditions. On some occasions, it also needs to be shown that the obtained slip-line field solution is indeed the unique solution based on the criteria of energy minimization (Johnson and Mellor,1973).

The similarity between the metal cutting process and the indentation process has been utilized to study the pressure distribution observed in machining. In machining, the cutting tool acts as an indenter which pushes against the workpiece being cut. As expected from the flat punch indentation, the pressure along the tool-chip contact should be about three times the value of flow stress. However, it was observed that in machining, the pressure at the tool tip is significantly lower than the expected value. This difference in contact pressure at the tool tip has been attributed to the ratio of confinement, which is the ratio of the uncut chip thickness to the contact length along the chip-tool contact, being very small in case of machining. The small confinement ratio leads to the plastic deformation traveling to the sides rather than traveling downwards as observed in indentation. In order to investigate the effect of confinement ratio further, an extensive study has been carried out by running flat punch compression problem with different confinement ratios.

### **3.3 Background**

In order to estimate the flow stress in the primary shear zone (PSZ) accurately, it is required to obtain an accurate estimation of the indentation pressure at the tip of the cutting tool. The analysis of machining becomes a very complex process when it comes to obtaining something like the detailed information about the flow around the finite cutting edge. Hence, it is useful to study other processes like the flat punch indentation, which are easier to understand. Further, the similarity of indentation with machining can assist in improving the understanding of metal cutting process. Both the processes can be approximated as plane strain processes since the width of the workpiece is significant. Researchers like Haddow and Johnson (1962) have used the square grid lines to understand the deformation during piercing of soft metals. The deformation of these gridlines from their original shape represented the elongation of the grain boundaries within the material. This information is helpful in understanding the direction of the maximum strains and different characteristics of the deformation like dead metal zones. Even in machining analysis, researchers like Heginbotham and Gogia (1961), Palmer and Yeo (1964) made use of photomicrographs and cinefilms to understand the deformation characteristics. Hutchings (1976) also showed the similarity of the deformation pattern, observed after the oblique impact of square plates in mild steel workpiece, with the deformations observed in machining. Multiple experiments with different impact angles, rake angles, and impact velocities were carried out. Finally, it was concluded that when there is a backward rotation of the impacting cube, deformation similar to metal cutting was observed.

Indentation by a flat punch can be considered to be a problem in which the stress and velocity at any given point are continuously varying from one time to another time (Johnson and Mellor, 1973). The slip-line field theory can be easily used to determine the yield point load, under which there is the onset of deformation in a rigid perfectly plastic body. In a flat punch

indentation problem, the development of the plastic zone happens in such a way that the punch and the workpiece configuration remains geometrically similar during the entire deformation. The workpiece punch configuration needs to be scaled down by a certain factor at each stage in order to obtain the same geometrical figure; the stress and velocity at any given point remain constant. This scaling makes the problem analogous to that of steady motion. However, it is still necessary to satisfy the velocity boundary condition required for the maintenance of the geometrical similarity (Johnson and Mellor,1973).

Tan and Chou (1989) developed a finite element program to analyze the flat punch indentation. They assumed an elasto-plastic material behavior and studied cases with smooth as well as rough punch. They didn't generate the slip-line field but compared the velocity field obtained from their FE simulations with the slip-line fields given by Prandtl as well as Hill. All of the simulations in their study are done for aluminum (Al 1100) with a Young's modulus of 68.95 GPa. Some simulations were carried out with the Young's modulus scaled by a factor of 10, but no significant difference was observed. However, the Poisson's ratio of 0.33 was used in all cases i.e. material was not incompressible. Two sets of simulations were carried out, one with pressure load applied along the punch-workpiece contact and the other with velocity applied to the punch instead of the pressure load. It was concluded that the shape of the triangular dead metal zone (DMZ) below the punch is much closer to that predicted by Prandtl (1920). It was also concluded that the velocity field and the magnitude of the velocity at the free surface are closer to the solution given by Prandtl.

Prandtl's solution is shown in Figure 3.1. From Hencky's equation (1923) for an alpha slip-line, we have

$$p + 2k\phi = \text{constant} \quad (1)$$

The point B in Figure 3.1 is at the free surface and the slip-line BD is a straight line,

$$p_B = k; p_D = p_B = k$$

From point D to C the total change in angle is  $\pi/2$ . Hence,

$$p_C = p_D + 2k(\phi_D - \phi_C) \quad (2)$$

$$p_C = k(1 + \pi) \quad (3)$$

The normal pressure at the punch contact is given by

$$\sigma_n = k + p_C \equiv k + k(1 + \pi) \equiv 5.14k \cong 3Y \quad (4)$$

A simple estimate for the pressure at the tip of the cutting tool can be obtained from the indentation theory. As per the analysis of the indentation process using a flat punch, the indentation pressure can be estimated to be three times the flow stress as shown in equation 4.

A statically admissible extension to the Prandtl's field has been given by Chakrabarty (1987) as shown in Figure 3.2. The region ABDEC is same as the Prandtl's field. The field to the left of ADPQ is uniquely defined since the circular arc CD and the condition of symmetry uniquely define the field to the left of DPQ. BN is the stress-free boundary where the tangency line at point N is vertical and parallel to the symmetry line. JM is the stress discontinuity, since

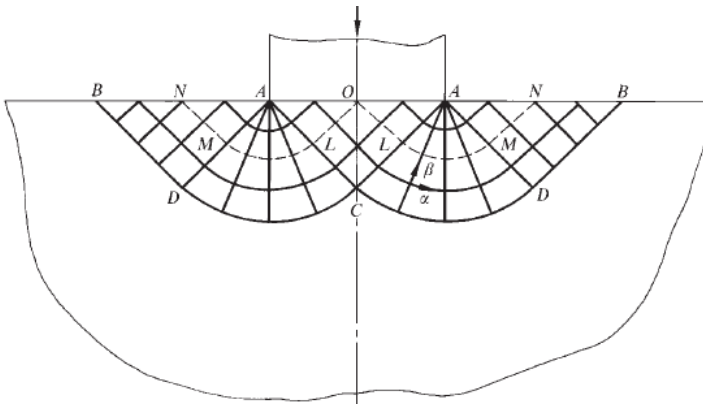


Figure 3.1: Slipline fields for the indentation of a semi-infinite medium by a flat punch given by Prandtl. (Figure adapted from Chakrabarty,1987)

the slip-lines of the same family start to intersect with one another. The field between slip-lines to the right side of the stress discontinuity JM has to be compatible with the slip-line JKN. Also, the hydrostatic pressure jump across the JM has to be compatible with the slip-line JKN.

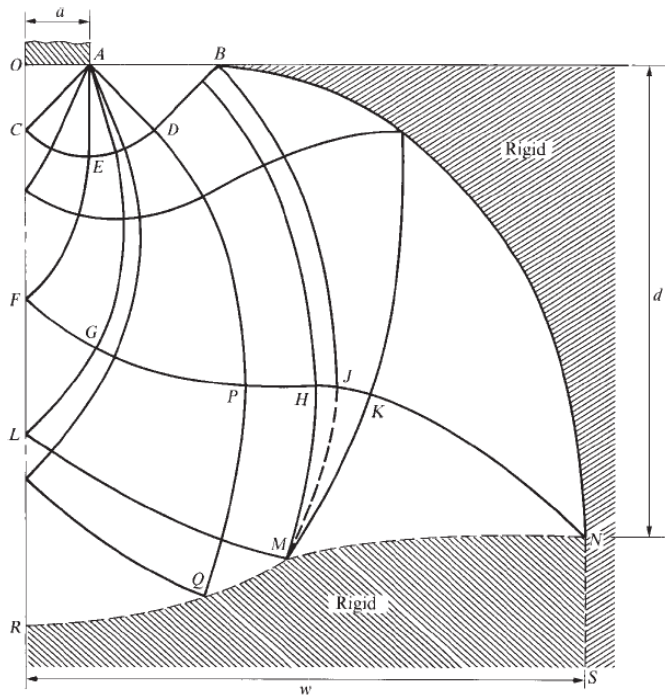


Figure 3.2: The extension of the flat punch indentation Prandtl field which is statically admissible (Figure adapted from Chakrabarty,1987)

These conditions are sufficient to generate the complete field bounded by JKN and JM.

The main aim of the current work is to find out the point of transition of the slip-line field from Prandtl's indentation field to the metal cutting field and use this information to understand the lower contact pressures observed in metal cutting. For this reason, machining has been considered to be a special case of indentation in which, the indenter is flat (wedge angle is 180 degrees).

Several researchers have attempted to predict the magnitude of the indentation force, either based on the geometry of the cutting edge and the cutting conditions or based on the observed deformation field in the PSZ. Albrecht (1960) was the first researcher to point out that the effect of the ploughing force of the cutting edge could be a significant contributor to the cutting force in metal cutting. He proposed a new cutting force diagram with divided the total cutting force in to two parts i.e. a force which doesn't contribute in the shearing of the material and is present only due to the non zero cutting edge radius and the remaining force which causes shearing.

Several researchers studied the flow of the metal around the cutting edge in order to understand the pressure distribution on the cutting edge and to obtain an estimate for the

indentation force. Most of the researchers proposed some sort of a slip-line field for machining and made its use to obtain estimates for indentation force. Palmer and Yeo (1964) performed orthogonal cutting experiments with blunt tools and recorded the material deformation on cine film. Based on their observations, a built-up edge (BUE) was postulated with an included angle of 90 degrees for most cutting conditions. Coupling such reasoning with their observations, they obtained an approximate slip line field for the metal flow around the cutting edge for a blunt tool when cutting a work hardening material. Sarvar and Thompson (1982) also studied metal cutting with blunt tools, at feeds which were less than or equal to the radius of the cutting edge of the tool. Based on their observations from the photomicrographs obtained with a quick stop device, it was concluded that there is a dead metal zone (DMZ) which occupies the region between the cutting edge and the extension of the rake face and machined surface. A slip line field solution was proposed taking the DMZ into account, with a PSZ of zero thickness. Equations were provided for the cutting and thrust forces based on the slip line field solution, including the component arising from the lower boundary of the DMZ, and were found to compare well with experimental data.

Shi and Ramalingam (1991) developed a slipline field for machining with chip breaker tools having a finite amount of flank wear. A finite thickness of the PSZ was found, arising from the wear land. Waldorf et al.(1996) adapted this slip line field for cutting with a blunt cutting edge, by introducing a triangular DMZ ahead of the cutting edge that causes the effective shape of the tool to be the same as that of a sharp tool with flank wear. According to this proposed model, the entire deformation reaching the free surface originates below the DMZ. The PSZ has been shown as a parallel sided zone.

Fang (2003) has given a highly detailed SLF for cutting with blunt tools. However, the curved cutting edge was replaced by two straight chords, that meet at an assumed stagnation point on the cutting edge and shear deformation arising from all points along the cutting edge is conveyed to the free surface. The analysis was generalized to handle different sticking friction coefficients for each of these two segments.

Kudo (1965) has provided slip-lines for restricted as well as non-restricted contact tools and the frictional resistance was almost constant. However, the static admissibility of the slip-line field was not completely determined. The model was able to predict the chip curl, cutting forces, chip thickness and the contact length based on the cutting parameters like the friction stress and the rake angle of the tool. The model is for a zero rake angle tool and for sticking

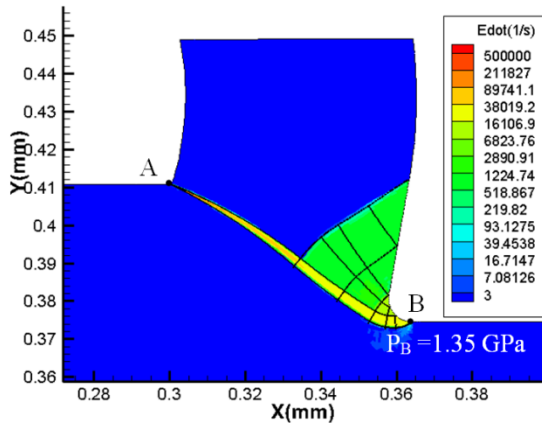


Figure 3.3: The slip-line field was generated for cutting with a 10-degree rake angle tool with 6  $\mu\text{m}$  cutting edge radius. The coefficient of friction was very high in order to simulate sticking friction. The depth of cut was 36  $\mu\text{m}$  and the velocity was 0.1m/s. The pressure at B obtained from FEA was found to be 1.35 GPa. The expected pressure based on the indentation theory should be 2.4 GPa (three times the flow stress value of 0.8 GPa. This pressure was significantly lower than that expected from indentation

friction condition. It was also suggested that the natural length of contact for an unrestricted tool is about 2.6 times the depth of cut. Kudo argued that since cutting is not an infinitesimal deformation process, the slip-line field solution which gives lower forces can't be necessarily considered to be the more realistic solution even if it is kinamatically admissible. He has provided several possible slip-line field solutions for the curled chip but there statical admissibility is questionable.

### 3.4 Indentation Pressure in Machining

In our previous work (Deshpande et. al., 2011) slip-lines for metal cutting were generated in order to investigate the indentation force component. Figure 3.3 shows the slip-lines for one such condition where a 10 degree rake angle tool with 6  $\mu\text{m}$  cutting edge radius was used. The depth of cut was 36  $\mu\text{m}$  with a cutting velocity of 0.1m/s. The friction coefficient of  $m=0.1$  was used in this simulation. For this simulation, it was found that the hydrostatic pressure at the lower most point of tangency of the tool tip was 1.35GPa. Thus, the contact normal stress was 1.82GPa (1.35 GPa + 0.462 GPa) as can be verified from Figure 3.4(a) and Figure 3.4(b). The ratio of this indentation pressure to the flow stress of 0.8GPa was calculated to be 2.2.

From Figure 3.4(a) it can be seen that starting from the free surface, the hydrostatic pressure decreases initially. This can be attributed to the beta slip-line being curved in the clockwise direction as seen in Figure 3.3. Further, after certain distance, the hydrostatic pressure starts to increase since the slip-line rotates in an anticlockwise direction. The sudden increase in the hydrostatic pressure near the cutting edge was due to the slip-line rotating to meet the last point of contact at the flank side. Overall, from the results of FEA of machining it was observed

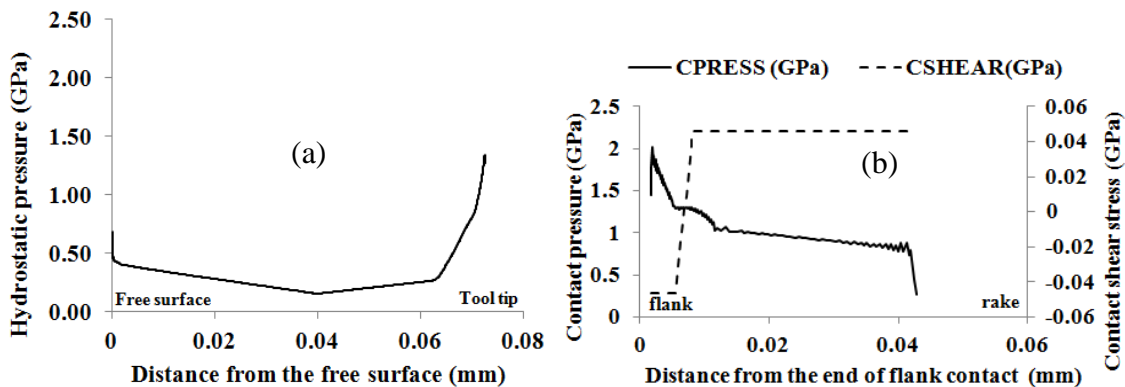


Figure 3.4: (a) The variation of the hydrostatic pressure along the beta slip-line starting from the free surface and ending at the last point of tangency of the cutting edge on its flank side and (b) distribution of the contact normal stress (CPRESS) and contact shear stress (CSHEAR) along the chip-tool contact

that the ratio of indentation pressure to flow stress ( $\chi$ ) varied between 1.5 and 2.5. Whereas, based on the theory of indentation, the indentation pressure (or hardness) is three times the flow stress of the material being indented as shown previously in equation 4. Thus, based on the indentation theory, the value of the expected indentation pressure is 2.4 GPa. This significantly lower value of pressure from machining compared to the expected value from indentation theory provided motivation to carry out a detailed comparison between machining and indentation. In order to understand the similarities and differences in machining and indentation, it was decided to carry out flat punch indentation analyses with different confinement ratios.

### 3.5 Analogy between Machining and Indentation

Figure 3.5 highlights the similarities between metal cutting and the flat punch indentation process. The cutting tool pushes the workpiece along the contact length ' $l_c$ ' similar to the manner in which the workpiece is indented by the flat punch of width ' $l_c$ '. In the case of metal cutting, the width of the incoming material is the uncut chip thickness or the feed shown as ' $d$ '. This width of the incoming material corresponds to the width of the workpiece being indented.

From Figure 3.5, the indenter or the punch can be thought to be a cutting tool with width equal to the contact length ' $l_c$ '. This analogy between machining and indentation provides an

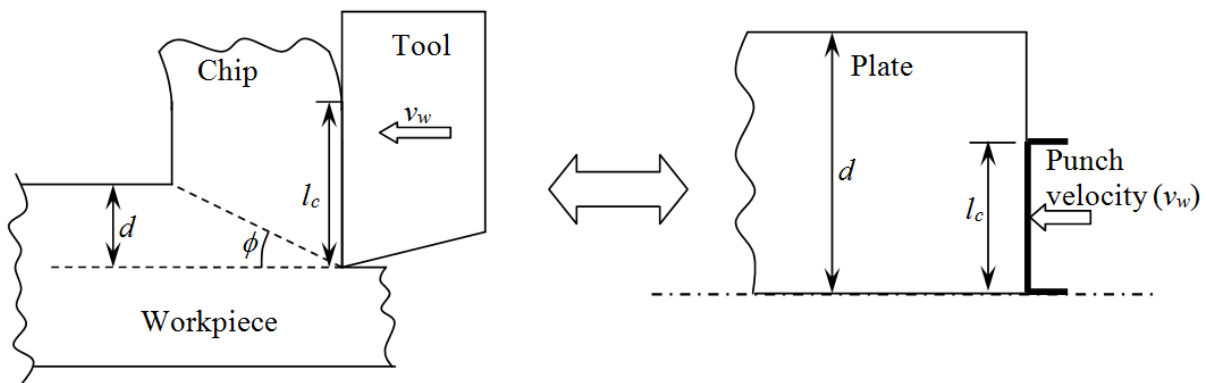


Figure 3.5: Similarity between machining and indentation

excellent opportunity to improve the understanding of complex deformations observed in machining with the aid of simpler fields observed in flat punch indentation. With this analogy to machining, indentation simulations were carried out at different confinement ( $d/l_c$ ) ratios. The variation of contact pressures with change in confinement ratios would provide significant insight on the reasons for lower pressures observed in machining. Additionally, the confinement ratio at which the slip-line field changes from the indentation field given by Prandtl to the slip-line field consisting of a shear plane can be known. The results of these simulations are presented in the later section.

### 3.6 FE Simulation Technique and Generation of Slip-lines

Indentation simulations were carried out using Abaqus Standard for different values of confinement ratios. In order to simulate the rigid plastic behavior, a very high value of Young's modulus  $E \geq 210,000$  GPa and the yield strength,  $Y = 1.0$  GPa was used for the workpiece material. The large value of Young's modulus compared to the yield strength makes the elastic strains ( $Y/E \leq 2.1 \times 10^{-5}$ ) negligible compared to the plastic strains. Further, a Poisson's ratio of 0.499

was used to make the material incompressible. Thus, a rigid plastic material was simulated and the slip-line field theory was applied to understand the deformation.

The punch was modeled as an analytical rigid entity as shown in Figure 3.6.

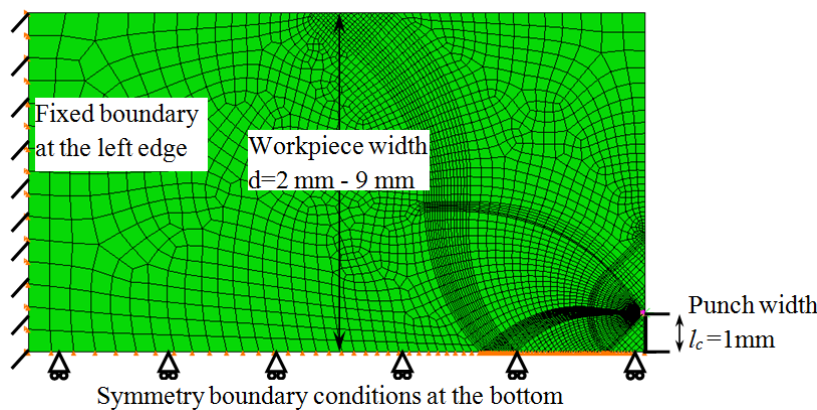


Figure 3.6: Flat punch indentation simulations were carried out for different confinement ratios ( $d/l_c$ ). The punch width was constant at  $l_c = 1$  mm and the width of the workpiece ( $d$ ) was varied from 2 mm to 9 mm. The boundary conditions are as shown.

A constant value of 1 mm was used for the width of the punch ( $l_c$ ). The width of the workpiece ( $d$ ) was varied from 2 mm to 9 mm in order to simulate different confinement ratios ( $d/l_c$ ). An iterative mesh refinement approach in which the first simulation was carried out with regular mesh and the next iteration was carried out by remeshing the workpiece such that the mesh is along the slip-lines obtained from the first iteration. The detailed approach of iterative mesh refinement and generation of slip-line field from the results of FE simulations has been described in our previous work (Chapter 2). The final set of simulations was carried out with the mesh exactly aligned to the slip-lines. The slip-line fields obtained from these simulations were compared with the slip-line field provided by Chakrabarty (1973).

A new slip-line field generation approach based on the results of Finite Element simulations, which makes use of the stress components  $\sigma_1$ ,  $\sigma_2$ , and  $\sigma_{12}$  to identify the local directions of principal stresses and maximum shear stress for each of the plastically deforming element, has been used in this work. The first and second directions of maximum shear stress (which are the slip line directions for plastically deforming elements) were rearranged such that the first and second directions in neighboring elements are aligned. Streamlines of the slip direction vectors yield the slip-line field. These computations were carried out using MAPLE™

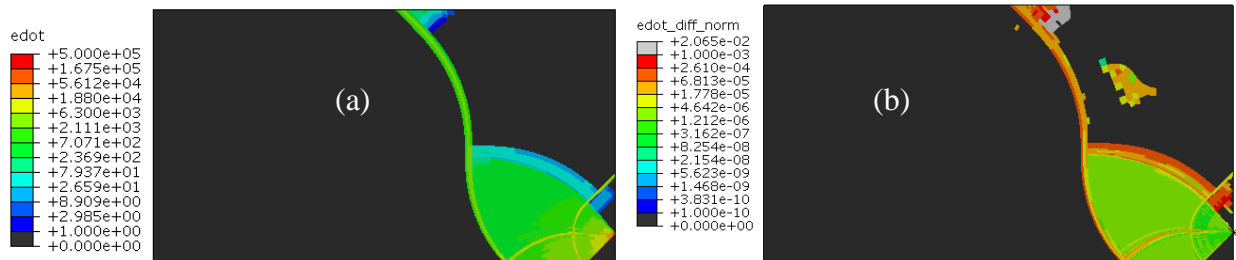


Figure 3.7: (a) The strain rate was calculated at punch displacement of  $1e-2$  mm. The difference in the two strain rates fields, one calculated at a punch displacement of  $1e-2$  mm and another at  $9e-3$  mm, was calculated and divided by the strain rate at punch displacement of  $1e-2$  mm. The above plot shows this normalized difference in strain rate to be extremely small indicating that the simulation has indeed reach steady deformation state.

the symbolic math package. The plots of the streamlines were generated in Tecplot. This method of generating SLFs by FEA has been validated using the rough punch compression problem and has been discussed in detail elsewhere (Chapter 2).

### 3.7 Verification of Attainment of Steady State

Before the computation of slip-lines from the results of FE simulations, a thorough check was carried out to verify the attainment of the steady state. In order to check if the deformations obtained in the flat punch simulations were indeed steady, the strain rate was calculated at different punch displacements of  $9e-3$  mm and  $1e-2$  mm. The difference in two strain rate values was calculated and was divided by the strain rate value at  $1e-2$  mm punch displacement. Figure 3.7(a) shows the plot of the strain rate calculated at punch displacement of  $1e-2$  mm. The normalized difference between the two strain rate values has been plotted in Figure 3.7(b). It can be seen that the normalized difference in strain rates is extremely small (varies between  $1e-10$  to

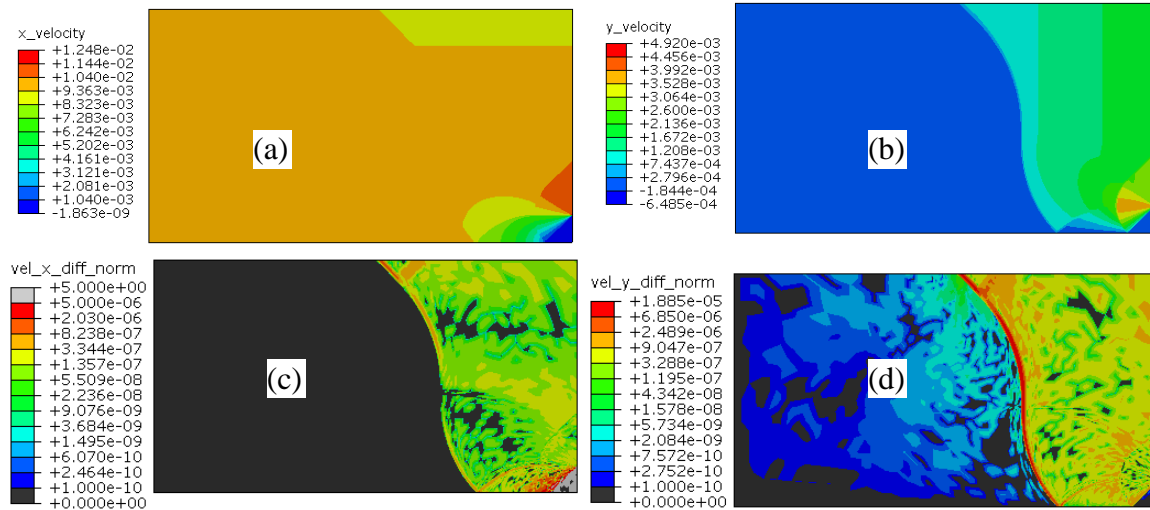


Figure 3.8: (a) The X component of velocity and (b) the Y component of velocity were calculated at punch displacement of  $1e-2$  mm. The velocity components were also calculated at  $9e-3$  mm of punch displacement. (c) The difference in the X components of velocity was normalized by dividing it with the X component of velocity at  $1e-2$  mm punch displacement and (d) the difference in the Y components of velocity was normalized by dividing it with the Y component of velocity at  $1e-2$  mm punch displacement.

2e-2) indicating that the deformation has reached steady state.

Same procedure was also carried out with the velocity field. Figure 3.8 (a) and Figure 3.8 (b) show the absolute values of X and Y component of the velocity respectively. Similar velocity field was calculated at two different values of punch displacement. The difference in each velocity components was calculated and normalized by dividing with the absolute value of the velocity component. The extremely small, normalized velocity difference observed in Figure 3.8 (c) and Figure 3.8 (d) show that the velocity components have stabilized and are constant irrespective of the punch displacement.

Further, for the confinement ratio of  $d/l_c=8.75$ , the cutting forces were plotted as a function of the punch displacement as shown in Figure 3.9. Once the punch and the workpiece contact is correctly established (after small initial punch displacement), the cutting forces reach a constant value irrespective of the punch displacement, indicating the steady nature of the process. Thus, from the strain rate field, the velocity field, and the graph of the cutting forces it was concluded that the deformation in the flat punch simulation had reached steady state. All

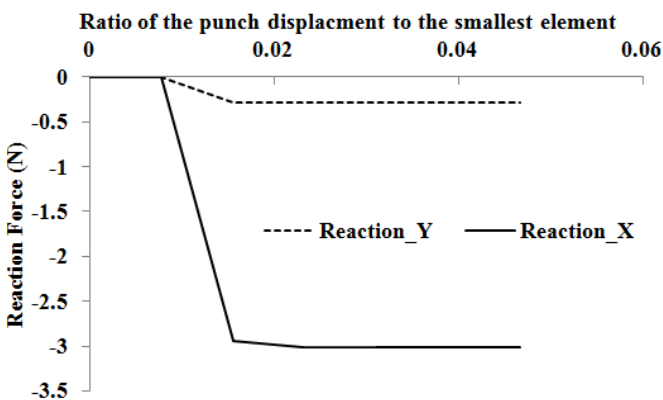


Figure 3.9: The reaction forces on the punch were plotted as a function of the ratio of the punch displacement to the smallest element. It was observed that the forces reached steady state very quickly once the contact was established. The plot is for  $d/l_c=8.75$

these checks for steady state deformation were carried out for all the flat punch indentation simulations.

Further to also check the rigid plastic assumption the ratio of the equivalent plastic strain to the maximum in plane elastic strain was plotted as shown in Figure 3.10 for  $d/l_c=8.75$ . It can be seen from Figure 3.10(d) that the

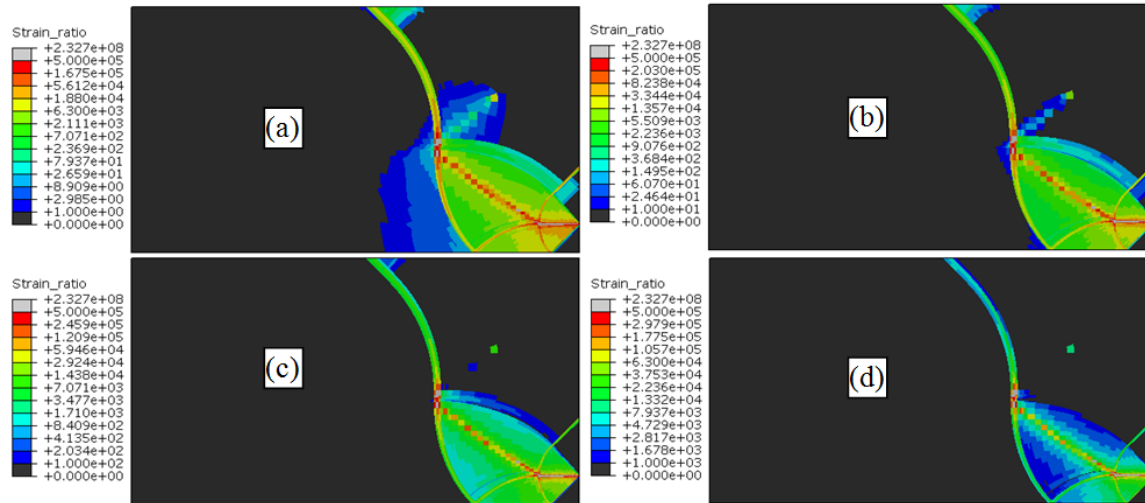


Figure 3.10: The plastic strain was divided by the maximum inplane principal elastic strain. This strain ratio was plotted with different lower contour ranges like (a) lower range =1, (b) lower range =10, (c) lower range=100, and (d) lower range=1000. It can be seen that the plastic strain is atleast 1000 times higher than the elastic strain in most of the region of interest.

plastic strains in the region of interest are at least 1000 time the elastic strains indicating the rigid plastic behavior.

### 3.8 Simulations with Different Values of the Confinement Ratios

Different simulations with decreasing  $d/l_c$  ratio were carried out in order to find the critical width at which the plastic deformation changes the pattern and spreads to the sides. In order to look at it from the machining point of view where the decrease in the confinement ratio suggests an increase in the contact length at the chip-tool interface, the scales of the plots are such that the width of the workpiece appears to be same and the width of the punch appears to be increasing. This is equivalent to the reduction in confinement observed in machining as the contact length between the workpiece and the tool increases.

### 3.9 Results for the Simulation with Different Confinement Ratios

Figure 3.11 shows the strain rate fields for simulations with different confinement ratios of  $d/l_c=9$ ,  $d/l_c =8.75$ ,  $d/l_c =4$ , and  $d/l_c =2$ . For the confinement ratio of  $d/l_c=9$  the plastic

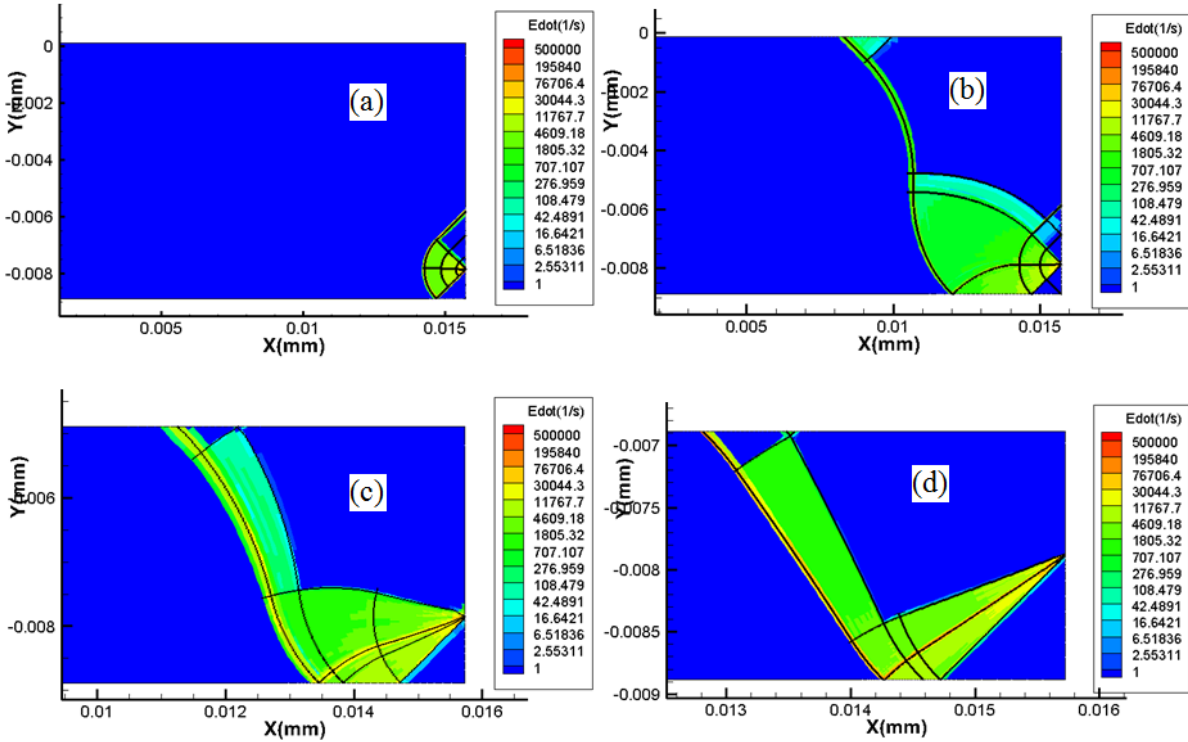


Figure 3.11: Slip-line fields were generated for different confinement ratios of (a)  $d/l_c=9$ , (b)  $d/l_c=8.75$ , (c)  $d/l_c=4$ , (d)  $d/l_c=2$ . As soon as the ratio decreases below 8.75, the deformation reaches the free surface

deformation travels down like a regular indentation field given by Prandtl. It can be seen that once the confinement ratio equals to  $d/l_c=8.75$  some part of the plastic deformation reaches to the free surface as expected in a flat punch indentation process, but some part of the plastic deformation travels to the sides of the workpiece in the form of a ‘S’ shaped shear plane. Once the confinement ratio decreases below the value of 8.75, the entire plastic deformation expands to the sides of the workpiece and an ‘S’ shaped shear plane is formed and the slip-line field is no more an indentation field. An additional simulation with a confinement ratio of 8.775, which is slightly higher than the critical value of 8.75, was carried out. The slip-line field along with the strain rate plot is shown in Figure 3.12 and it is clear that even for a slightly higher value of the confinement ratio than the critical value, the slip-line field is the Prandtl’s field.

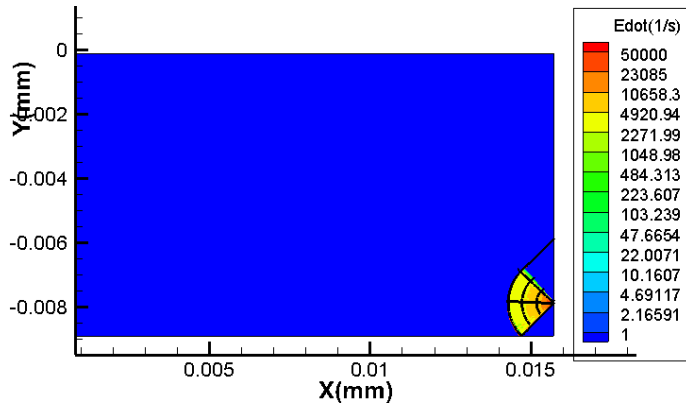


Figure 3.12: An Additional simulation with  $d/l_c = 8.775$  which is slightly higher than 8.75, was carried out in order to verify that indeed the deformation reaches the free surface at 8.75. The slip-line field and strain rate contours clearly show that at  $d/l_c = 8.775$  the field is the Prandtl's field

In order to understand the deformation pattern better, the reaction forces were plotted as a function of the confinement ratio as shown in Figure 3.13(a). The reaction force decreases with decrease in confinement ratio. Since the punch width for all the simulations is 1 mm, this decrease in the force indicates decrease in reaction force per unit

contact length. Thus, as the deformation reaches to the sides, less force per unit contact length is required to indent the material. This also means that the 'S' shaped shear deformation is the more preferred path for deformation since it requires less force.

Further, the average contact pressure along the punch contact was plotted as a function of the confinement ratio as shown in Figure 3.13 (b). It can be seen from Figure 3.13 (b) that as the

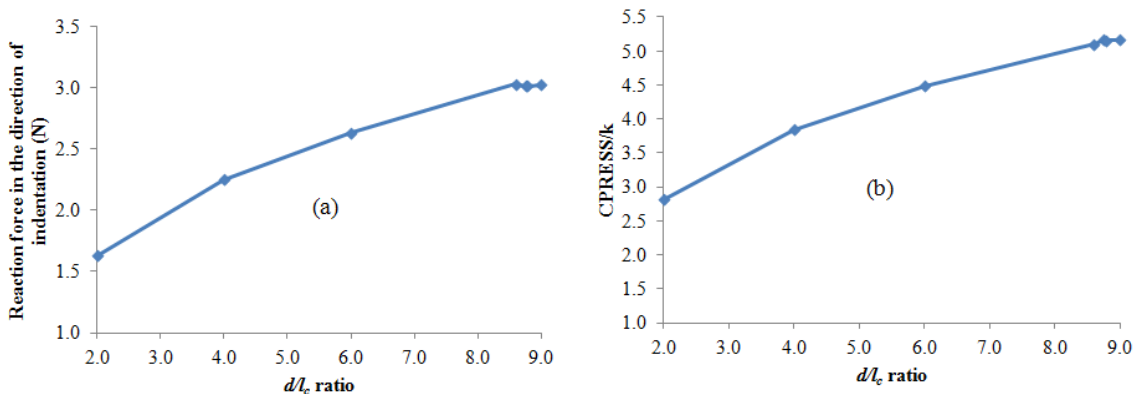


Figure 3.13: (a) The ratio of the contact pressure to the shear strength of the material was plotted for different confinement ratios. (b) The reaction force in the direction of the punch indentation was also plotted. It was observed that both the quantities decrease as the confinement ratio decreases.

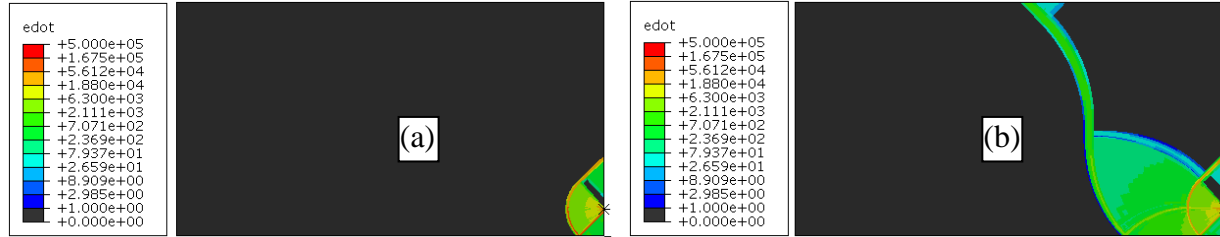


Figure 3.14: From the strain rate field obtained for zero coefficient of friction for the confinement ratios of (a)  $d/l_c = 8.75$  and (b)  $d/l_c = 8.70$  it can be seen that the plastic deformation reaches the sides of the workpiece at the ratio of 8.70 instead on 8.75 observed for sticking friction

confinement ratio decreases, there is a gradual decrease in the average contact pressure along the punch-workpiece contact. In metal cutting, the confinement ratio ( $d/l_c$ ) is always significantly less than one, indicating that the pressure at the tip of the cutting tool should be significantly less than that expected from the indentation process. Thus, improved understanding of the observed reduction in pressure is required to better understand pressures in metal cutting.

### 3.10 Effect of Friction on the Critical Confinement Ratio

The value of the critical confinement ratio obtained from FE analysis was found to be 8.75 as opposed to 8.593 provided in the literature (Chakrabarty, 1987). In order to check if the high friction coefficient of friction value used along the punch-workpiece contact was not influencing the critical confinement ratio, a simulation with zero coefficient of friction was carried out. With the zero friction coefficient, the critical ratio at which the ‘S’ shaped shear plane was formed and the plastic deformation reached to the sides of the workpiece was found to decrease by a very small value of 0.05 to 8.70. Figure 3.14 shows the plot of strain rates generated for confinement ratios of 8.75 and 8.70 respectively, with the friction coefficient being zero. Since the difference in the critical confinement ratio was negligible, it can be concluded that the critical ratio is independent of the friction coefficient along the punch-workpiece interface.

### 3.11 Simulation with an Inclined Punch

Based on the flat punch indentation simulations with decreasing confinement ratios, it was clear that the lower pressures observed in machining were due to the very small confinement values. However, there was a need to understand the reason for the difference in the theoretical and observed critical confinement ratio value. One possible reason might be the presence of the stress singularity at the corner of the punch. In order to remove the sharp corner of the punch, a single simulation with an inclined punch as shown in Figure 3.15 was carried out.

As the punch would indent the plate, more region of the plate would come in contact with the punch. This would increase the contact length gradually, decreasing the confinement ratio. Additionally, this would also help in eliminating the sharp corner of the punch, thus removing the stress singularity and also help to study the transition of the slip-line field pattern from indentation to machining. A single simulation was carried out where the punch was kept inclined with the plate by  $0.05^\circ$ . The punch was pushed in with a very small velocity of  $5e-4$  m/s in order to better capture the gradual decrease in the confinement ratio.

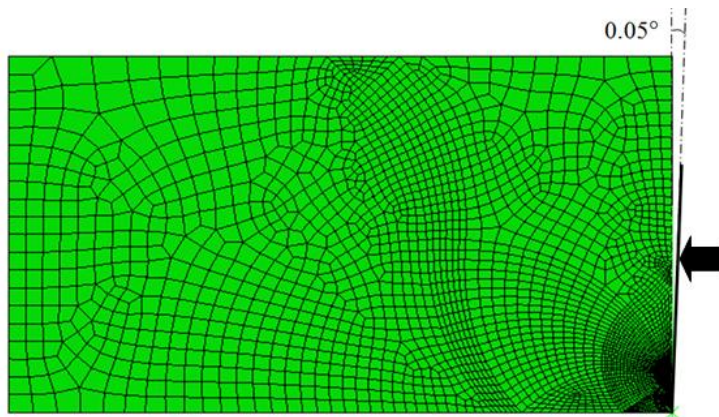


Figure 3.15: The plate was indented with a punch with an infinitesimal inclination of  $0.05$  degrees to simulate decreasing confinement. Note that the inclination of the punch shown above is not to scale and has been exaggerated for clarity

### 3.12

#### results for the simulation with the inclined punch

The slip-lines were computed at different punch displacements during the simulation i.e. at different contact lengths.

Figure 3.16 shows the computed slip-lines overlapped on the strain

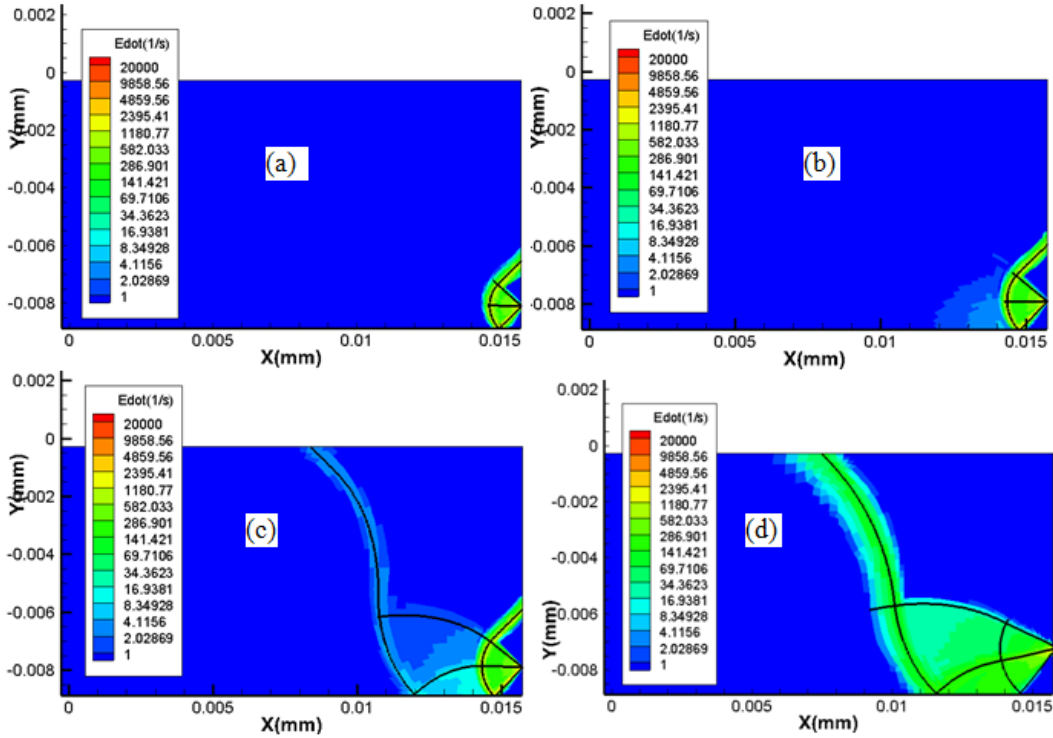


Figure 3.16: The strain rate and slip-line field generated at different times during the indentation of a plate with an infinitesimally inclined punch (0.05 degrees) at a)  $d/l_c=10.917$ , b)  $d/l_c=8.75$ , c)  $d/l_c=8.59$ , and d)  $d/l_c=5.131$

rate contours. An indentation field given by Prandtl is obtained at punch displacement of  $2.5e-4$  mm as shown in Figure 3.16 (a). The indentation zone can be seen to increase and the punch displacement increases as can be seen in Figure 3.16 (b). The indentation zone keeps on increasing upto a certain confinement ratio ( $d/l_c$ ). At the punch displacement equivalent to the confinement ratio is 8.54, the deformation reaches to the free surface on the sides and the field changes from the pure indentation field to the indentation and shear plane mixed field shown in Figure 3.16 (c). As the simulation progresses further, the indentation field vanishes and the entire deformation happens on the ‘S’ shaped shear plane only.

An interesting thing to note was that the transition of the field happened in a very short duration. The punch velocity was reduced to a very small value of  $5e-4$  m/s in order to better capture the transition, but however small value of the velocity was used, the transition would

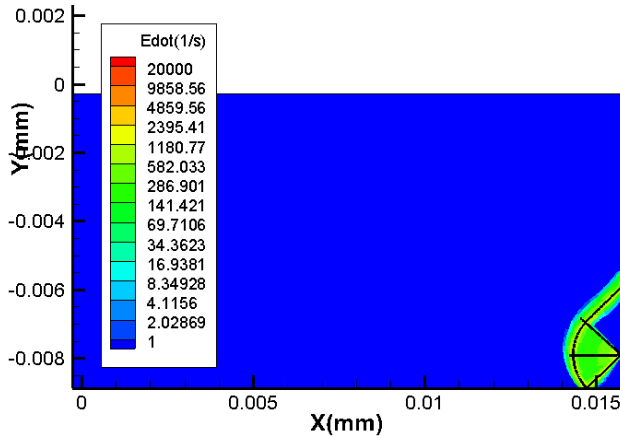


Figure 3.18: An additional frame was processed at  $d/l_c=8.66$  which is slightly higher than 8.593, was carried out in order to verify that indeed the deformation reaches the free surface at 8.593. The slip-line field and strain rate contours clearly show that at  $d/l_c = 8.66$  the field is the Prandtl's field

happen within just one output frame. In order to be certain that indeed, the switchover happens at the confinement ratio of 8.54, slip-line field for a previous output frame corresponding to a confinement ratio of 8.64 was generated as shown in Figure 3.18. It can be seen that for the confinement ratio of 8.64 the slip-line field is the Prandtl's field and doesn't show the formation of the shear

plane. Thus, the transition truly happens at the confinement ratio of 8.54.

Figure 3.17 shows the graph of variation of the cutting forces with respect to the displacement of the punch. The force (reaction\_x) in the direction of the punch displacement

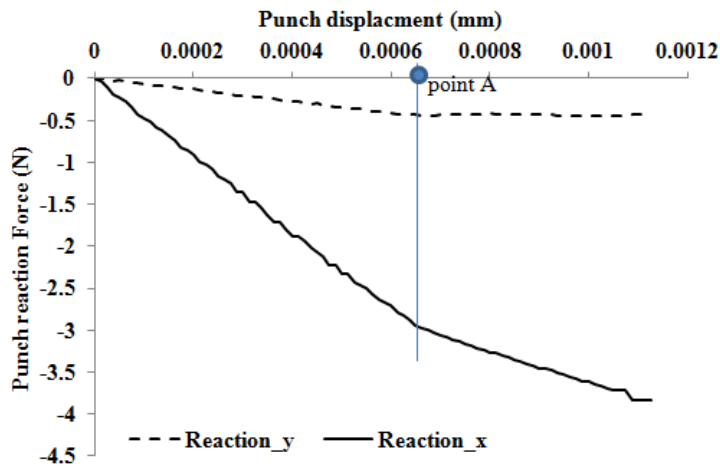


Figure 3.17: The cutting force increases with decrease in the confinement ration as expected. Interesting thing to note is that the rate of increase of force decreases after the punch displacement of 0.00066 mm which is when the shear plane is formed and the deformation reaches the free surface

increases linearly but the rate of force increase, decreases beyond the punch displacement of 0.00066 mm identified in the figure as 'point A'. This displacement is equivalent to the confinement ratio of 8.540, same ratio at which the transition of the slip-line field from the flat punch

Table 3.1: the average contact pressure obtained at different simulation times and their corresponding confinement ratios.

Punch displacement (mm)	Contact length (mm)	Confinement ratio ( $d/l_c$ )	Average contact pressure ( $P/k$ )
5.00E-04	0.787	10.917	5.56
6.424e-4	0.9820	8.75	5.23
6.537e-4	1.0003	8.59	5.17
1.25E-03	1.675	5.131	4.54

indentation to the ‘S’ shaped shear plane was observed.

This clearly indicates that less force per unit contact length is required to indent the material once the plastic deformation reaches to the

sides forming a shear plane. Table 3.1 shows the average contact pressure along the punch contact at different times in the simulation. The contact pressure is normalized by the shear strength of the material. It can be seen that the average contact pressure drops gradually as the confinement ratio decreases. Thus, as the confinement decreases, the contact pressure decreases. In metal cutting, the contact length is more than the depth of cut, which means that the confinement ratio is less than one. This explains the significantly lower pressure at the cutting tool tip compared to the indentation by flat punch.

### 3.13 Discussion

The slip-line field and the hodograph for this critical confinement ratio given by Chakrabarty (1987) is shown in Figure 3.19. It has been stated that once the confinement ratio is reduced to a certain critical value, the plastic zone deviates from the normal indentation zone and spreads to the sides of the workpiece.

It can be observed from Figure 3.11 that initially when the confinement ratio is high the field is an indentation field but as the ratio crosses the value of 8.75, the plastic deformation takes two paths; one as a ‘S’ shaped shear plane which reaches on the sides and the other in the form of an indentation field. The strain rate in the indentation field is much higher than the strain rate in the ‘S’ shaped shear plane. If the confinement ratio is decreased further, even by a

small value of 0.025 to 8.675, the entire deformation happens in the ‘S’ shaped shear plane and no deformation is observed in the indentation zone. Thus, the value of critical confinement ratio at which field changes from an indentation field to the shear plane field was found to be 8.75. Chakrabarty has reported this value to be 8.593 which was calculated based on the calculations of force and moment equilibrium. Table 3.2 shows the comparison of different dimensions given by Chakrabarty with the corresponding dimensions obtained from FE analysis. The difference in the observed values was attributed to the stress singularity at the corner of the punch. This singularity was not accounted for in the theoretical calculations.

### 3.14 Conclusion

The slip-line field generated from the results of finite element simulations of flat punch indentation showed that Prandtl’s field was obtained only when the confinement ratio was above a critical value of 8.75. For confinement ratios  $\leq 8.75$ , the slip-line field was similar to the one observed in metal cutting and an ‘S’ shaped shear plane was present. The plastic deformation

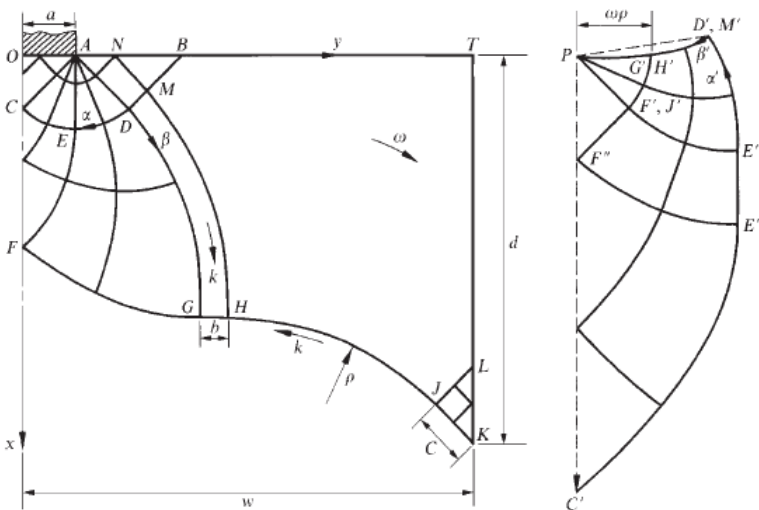


Figure 3.19: The slip-line field and the hodograph provided by Chakrabarty (1987) for the critical confinement ratio of 8.75 at which the deformation reaches the free surface. (Figure reproduced from Chakrabarty,1987)

traveled to the side of the block instead of reaching to the top surface, forming this ‘S’ shaped shear plane. The contact pressure required to indent the material decreased as soon as the shear plane was formed. This indeed shows that it is easier to indent the material at lower confinement ratios. Also,

Table 3.2: The different geometry quantities at the critical confinement ratio values obtained from FE analysis were compared with the values provided by Chakrabarty (2006). Figure 2 represents each of the quantity mentioned below

	$\rho/a$	$b/a$	$c/a$	$w/a$	$d/a$
Chakrabarty	5.686	0.490	0.937	8.593	7.290
FEA	5.520	0.560	1.023	8.750	7.340

the indentation pressures are lower for lower confinement ratios. The confinement ratios in metal cutting are always less than one, since the depth of cut is

always less than the tool-chip contact length. This observation of the indentation pressure being lower for smaller confinement ratios is very significant considering the fact that the confinement ratios in metal cutting is always less than one. Further, the critical confinement ratio dropped to 8.54 from the previously observed value of 8.75 for the case where the punch was inclined by a very small angle of 0.05 degrees with the workpiece, making it very close to Chakrabarty's predicted value of 8.593. This difference in the critical confinement ratio with flat punch and inclined punch geometries is attributed to the presence of a point of stress singularity. This stress singularity was a result of the presence of the geometrical corner point in case of the flat punch.

### 3.15 Acknowledgement

This material is based upon work supported by the National Science Foundation under grant number EIA-0216178 and grant number EPS-0236913, matching support from the State of Kansas and the Wichita State University High Performance Computing Center. NSF support under grant number DMI-0621174 is also acknowledged.

### 3.16 References

Adibi-Sedeh AH, and Madhavan V., 2003, "Understanding of Finite Element Analysis Results Under the Framework of Oxley's Machining Model," Proceedings of the 6<sup>th</sup> CIRP International Workshop on Modeling of Machining, Hamilton, Ontario, pp 1-15.

Albrecht P., 1960, "New Developments in the Theory of Metal Cutting Process, Part 1: The Ploughing Process in Metal Cutting," Transactions of the ASME, v82, pp 348-358.

Bailey J.A., and Bhanavadia D.G., 1973, "Correlation of Flow Stress with Strain Rate and Temperature During Machining," J. Eng. Mat. Tech., pp. 94-98.

Basuray P.K., Misra B.K., and Lal G.K., 1976, "Transition from Ploughing to Cutting During Machining with Blunt Tools," Wear, v43, n3, pp.341-349.

Chakrabarty J., *Theory of Plasticity*, 3<sup>rd</sup> Ed, Elsevier Butterworth-Heinemann, 2006

Challen J.M. and Oxley P.L.B., 1984, "A Slip Line Field Analysis of the Transition from Local Asperity Contact to Full Contact in Metallic Sliding Friction," Wear, v100, pp. 171-193.

Connolly R. and Rubenstein C., 1967, "The Mechanics of Continuous Chip Formation in Orthogonal Cutting," International Journal of Machine Tool Design, v8, pp. 159-187.

Deshpande A., Madhavan V., and Adibi-Sedeh A., 2011, "Models for the Indentation Force in Metal Cutting", Transactions of the North American Manufacturing Research Conference, Corvallis, OR, v39, pp 233-242.

Deshpande A., Madhavan V., and Al-Bawaneh M., 2010, "Determination of Johnson-Cook Material Model Constants for AISI 4340 HR by Metal Cutting," Transactions of NAMRI/SME 38, pp. 25-32.

Fang N., 2003, "Slip-Line Modeling of Machining with a Rounded-Edge Tool – Part 2: Analysis of the Size Effect and the Shear Strain-Rate," Journal of the Mechanics and Physics of Solids, v51, pp. 743-762.

Fang N., 2003, "Slip-Line Modeling of Machining with a Rounded-Edge Tool - Part I: New Model and Theory" Journal of the Mechanics and Physics of Solids, v51, pp. 715-742.

Fang N, Dewhurst P (2005) Slip-Line Modeling of Built-Up Edge Formation in Machining. International Journal of Mechanical Sciences 47, pp. 1079-1098.

Fang N., Jawahir I.S., 2002, "Analytical Predictions and Experimental Validation of Cutting Force Ratio, Chip Thickness, and Chip Back-Flow Angle in Restricted Contact Machining Using the Universal Slip-Line Model," International Journal of Machine Tools and Manufacture, v42, pp. 681-694.

Hill, R., *The Mathematical Theory of Plasticity*, 1<sup>st</sup> Ed., Oxford University Press, 1950.

Johnson G.R., and Cook W.H., 1983, "A Constitutive Model and Data for Metals Subjected to Large Strains, High Strain Rates and High Temperatures" Proceedings of the 7th International Symposium on Ballistics, The Hague, Netherlands, pp. 541–547.

Johnson, W., and Mellor, P. B., *Engineering Plasticity*, 1<sup>st</sup> Ed, Van Nostrand Reinhold, 1973

Karpat Y. and Ozel T., 2006, "Identification of Friction Factors for Chamfered and Honed Tools Through Slip-Line Field Analysis," Proceedings of the ASME International Conference on Manufacturing Science and Engineering, pp. 461-470.

Oxley P.L.B., *The Mechanics of Machining: An Analytical Approach to Assessing Machinability*, Ellis Horwood, 1989

Ozel T. and Zeren E., 2006, "A Methodology to Determine Work Material Flow Stress and Tool-chip Interfacial Friction Properties by Using Analysis of Machining," ASME Transactions, Journal of Manufacturing Science and Engineering, v128, pp. 119-129.

Palmer W.B. and Yeo R.C.K., 1963, "Metal Flow Near the Tool Point During Orthogonal Cutting with a Blunt Tool," Proc. 4th Int. MTDR Conf, pp. 61-71.

Pujana J., Arrazola P.J., M'Saoubi R., and Chandrasekaran H., 2007, "Analysis of the Inverse Identification of Constitutive Equations Applied in Orthogonal Cutting Process," International Journal of Machine Tools and Manufacture, v47, pp. 2153-2161.

Roth R.N. and Oxley P.L.B., 1972, "Slip-Line Field Analysis for Orthogonal Machining Based upon Experimental Flow Fields," Journal of Mechanical Engineering Science, v14, pp. 85-97.

Sarwar M. and Thompson P.J., 1982, "Cutting Action of Blunt Tools," Proceedings of the 22<sup>nd</sup> International MTDR conference, pp.295-304.

Shatla M., Kerk C., and Altan T., 2001, "Process Modeling in Machining Part I: Determination of Flow Stress Data," International Journal of Machine Tool and Manufacture, v41, pp. 1511–1534.

Shi T. and Ramalingam S., 1991, "Slip-Line Solution for Orthogonal Cutting with a Chip Breaker and Flank Wear," International Journal of Mechanical Sciences, v33, n9, pp.689-704.

Srinivasan K. and Madhavan V., 2010, "Experimental Determination of Strain Rate and Flow Stress in the Primary Shear Zone While Machining Hot Rolled AISI 4340," Transactions of NAMRI/SME 38, pp. 213-220.

Stevenson M.G. and Oxley P.L.B., 1969, "An Experimental Investigation of the Influence of Speed and Scale on the Strain-Rate in a Zone of Intense Plastic Deformation," Inst Mech Eng Proc (Part 1) Gen Proc, pp. 561-176.

Tan T.M., Li, S., and Chou, P.C., 1989, "Finite element solution of Prandtl's flat punch problem", Finite Elements in Analysis and Design, v6, pp 173-186

Waldorf D.J., 2006, "A Simplified Model for Ploughing Forces in Turning," Journal of Manufacturing Processes, v8, pp 76-82.

Waldorf D.J., DeVor R.E., and Kapoor S.G., 1999, "An Evaluation of Ploughing Models for Orthogonal Machining," Transactions of ASME, v121, pp 550-558

Waldorf D.J., DeVor R.E., and Kapoor S.G., 1998, "A Slip-Line Field for Ploughing During Orthogonal Cutting," Journal of Manufacturing Science and Engineering, v120, pp. 693-699.

Waldorf D.J., DeVor R.E., and Kapoor S.G., 1999, "Worn Tool Forces Based on Ploughing Stresses," Transactions of the North American Manufacturing Research Institution of SME 27, pp.165-170

## CHAPTER 4

### SLIP-LINE FIELD MODEL FOR TOOLS WITH FINITE CUTTING EDGE RADIUS

#### 4.1 Abstract

Slip-line field for metal cutting has been developed based on the results of high resolution finite element (FE) simulations carried out under different conditions of friction, rake angle, and the ratio of the uncut chip thickness to the radius of the cutting edge. An iterative approach where the slip-lines generated with unstructured mesh was used to modify the mesh by aligning it to the slip-line field. In this way, the shape and extent of key features like the width of the primary shear zone (PSZ) and the extent of the dead metal zone (DMZ) were captured accurately. It has been shown that a dead metal zone exists for all values of friction of  $m > 0$ . The DMZ starts as a stagnation point for  $m = 0$  and gradually increases to a triangular zone below the tool tip with finite cutting edge and has an included angle of  $90^\circ$ . This happens irrespective of the cutting conditions and the tool geometry. The plastic deformation originating from the lower boundary of the DMZ reaches the free surface of the chip, forming a Primary Shear Zone (PSZ). At the free surface, the width of the PSZ is zero, thus giving rise to a point of singularity. For conditions where  $m < 1$ , the field is similar in many aspects to the one proposed by Dewhurst (1978) for cutting with a sharp tool. It was found that the existence of the finite cutting edge radius adds finite width to the PSZ which, in case of a sharp tool has zero width. For sticking friction conditions ( $m = 1$ ), where straight chips are produced, the slip-line field in the region of PSZ is made up of a centered fan field with the center located at the point of intersection of the free surface and the chip. This field for straight chips is similar to the one proposed by Kudo (1965), except that the finite radius of the cutting edge was neglected and the tool was assumed to be sharp in Kudo's model.

*Keywords:* FEA; slip-line field model, machining; finite cutting edge

## **4.2 Introduction**

In most of the machining research, it is assumed that the cutting edge radius of the tool is either zero (Lee and Shaffer, 1951; Dewhurst, 1978) or is simplified as multiple straight segments (Fang, 2003). This assumption helps to significantly reduce the complexity of analysis of the chip formation process as demonstrated by Merchant's model (Ernst and Merchant, 1941) as well as Lee and Shaffer's model (1951). However, it has been observed based on the cutting experiments that the even a small cutting edge radius has significant effect on the chip formation process especially, at the micro and nano machining scales (Basuray et. al., 1977). Quantifying the effect of the cutting edge radius helps in correct estimation of the shearing force which is used to estimate the flow stress from experiments (Srinivasan and Madhavan, 2010). Also, complete understanding of the flow around the rounded cutting edge can be helpful in designing the ideal geometry of the cutting tool. The effect of cutting edge radius and the flow around the finite cutting edge has been studied by various researchers like Albrecht (1960), Heginbotham and Gogia (1961), Palmer and Yeo (1964), Abdelmoneim and Scrutton (1974), Basuray et. al. (1976), Sarwar and Thompson (1982), Shi and Ramalingam (1991), Waldorf et. al. (1996), Schimmel (1999), Manjunathaiah and Endres (2000), Fang (2003), Karpal and Ozel (2006). Some of the researchers like Dewhurst (1977), Kudo (1965), Fang (2003), Chakrabarty (1979) have developed complete slip-line field models for metal cutting and used them to estimate the ploughing force caused due to finite cutting edge radius of the tool.

## **4.3 Background**

Albrecht (1960) was the first to point out that the ploughing effect of the cutting edge could be a significant contributor to the cutting force in metal cutting. He proposed a new cutting

force diagram which was similar to Merchant's force diagram, but considered forces due to ploughing and forces due to the actual shearing of the material as two separate entities. The resultant force vector acting on the tool was taken to be the vector sum of separate contributions from the shearing action along the shear plane and the ploughing action of the cutting edge of the tool. He assumed that the forces arising due to the finite cutting edge of the cutting tool were the ploughing forces which didn't contribute to the shearing of the material. In the current research, it has been shown that only some fraction of the total force arising due to the finite cutting edge, contributes to the ploughing action of the tool.

Heginbotham and Gogia (1961) extensively studied Built Up Edge (BUE) formation around a rounded cutting edge tool. They provided information about the shape and size of the built up edge observed in machining of ferrous metals. An attempt was made to fit the observed deformation field with slip-lines with the help of photomicrographs. They showed slip-line field with a double curved first boundary and comprised of indentation as well as bending of the chip due to presence of the chip curl. The slip-line field was then used to understand the observed built up edge geometry.

Palmer and Yeo (1964) performed orthogonal cutting experiments with blunt tools and recorded the material deformation on cine film. Reasoning that an abrupt change in material flow at a stagnation point on the tool would violate equilibrium, Palmer and Yeo postulated that a built up edge (BUE, or dead metal zone, DMZ) with an included angle of  $90^\circ$  would exist under most cutting conditions. Coupling such reasoning with their observations, they obtained an approximate slip line field for the metal flow around the cutting edge for a blunt tool when cutting a work hardening material. Based on the streamlines, they concluded that the presence of the BUE tends to increase the depth of cut and decrease the effective rake angle.

Basuray et al. (1976) studied the flow of metal around the rounded cutting edge at small depths of cut. It was shown that the chip formation occurred only if the depth of cut was above a critical value. The point on the cutting edge corresponding to this critical depth of cut was termed as the neutral point. They obtained an expression for the energy expended in ploughing by a finite cutting edge radius tool based on the upper bound solution proposed by Abdelmoneium and Scrutton (1974). This neutral point angle was obtained by equating this energy expended in ploughing with the energy expended in chip formation with a sharp tool. It was concluded that the neutral point angle doesn't depend on the cutting parameters or tool geometry and has a constant value of  $37.6^\circ$ .

Sarvar and Thompson (1982) studied metal cutting with blunt tools, at feeds which were less than or equal to the cutting edge radius of the tool. In photomicrographs obtained with a quick stop device they observed a DMZ occupied the region between the cutting edge and the extension of the rake face and machined surface. A slip line field solution was proposed taking the DMZ into account, with a PSZ of zero thickness. Interestingly, they postulated a fan field PQS extending along the rake face contact. Equations were given for the cutting and thrust forces based on the slip line field solution, including the component arising from the lower boundary of the DMZ, and were found to compare well with experimental data.

Shi and Ramalingam (1991) developed a SLF for machining with chip breaker tools having a finite amount of flank wear. A finite thickness of the PSZ was found, arising from the wear land.

Waldorf et al. (1996, 1998, 1999, 2006) adapted this slip line field for cutting with a blunt cutting edge, by introducing a triangular DMZ ahead of the cutting edge that causes the effective shape of the tool to be the same as that of a sharp tool with flank wear. According to the slip-line

field model proposed by Waldorf, the entire deformation reaching the free surface originates below the DMZ. The PSZ has been shown as a parallel sided zone. There exists a chip prow at the free surface of the chip.

Karpat and Ozel (2006) have modified Waldorf et al.'s field slightly, by considering the lower boundary of the DMZ to be at angle  $\psi$  with respect to the cutting velocity. They assume that the streamlines to the stagnation point are straight (without any retardation zone) and postulate an effective uncut chip thickness that is smaller (by a factor depending on  $\psi$ ) than the actual uncut chip thickness specified, similar to Connolly and Rubenstein (1967). However, Sarvar and Thompson (1982) have presented conclusive evidence against this.

Fang (2003) has given a highly detailed SLF for cutting with blunt tools. However, the curved cutting edge has been assumed to be made up of two straight chords that meet at a stagnation point on the cutting edge and shear deformation arising from all points along the cutting edge is conveyed to the free surface. The analysis is generalized to handle different sticking friction coefficients for each of these two segments.

Kudo (1965) has provided slip-lines for restricted as well as non-restricted contact tools and the frictional resistance was almost constant. He has also given slip-line fields for curled chips. However, the statical admissibility of the slip-line field was not completely determined. His model was able to predict the chip curl, cutting forces, chip thickness and the contact length based on the cutting parameters like the friction stress and the rake angle of the tool. The model is for a zero rake angle tool and for sticking friction condition. It was also suggested that the natural length of contact for an unrestricted tool is about 2.6 times the depth of cut. According to Kudo, since cutting is not an infinitesimal deformation process, the slip-line field solution which gives lower forces can't be necessarily considered to be the more realistic solution even if it is

kinamatically admissible. He has provided several possible slip-line field solutions for the curled chip but there statical admissibility is questionable. It has been claimed that there are many valid slip-line fields for one value of  $\psi$ .

In all of the previous research, either a sharp tool has been used or some approximations of the rounded cutting edge geometry have been made. Also, in most of the previous research, the matrix operator technique developed by Dewhurst and Collins (1973) has been used to generate the slip-line field. This technique is a ‘trial and error’ technique where a slip-line field is first generated and then checked if the force and moment equilibriums are satisfied along with the velocity boundary conditions. The newly developed slip-line field generation technique in this work is based on the results of finite element analysis due to which the force and moment equilibrium and velocity boundary conditions are satisfied automatically.

#### **4.4 Finite Element Analysis and the Slip-Line Field Generation Technique**

The ALE analysis capability available in ABAQUS/Explicit was used to carry out a 2D finite element analysis of orthogonal machining as described in detail elsewhere (Adibi-Sedeh AH, and Madhavan V., 2003). The first model for indentation force was developed based on previous simulations with strain, strain rate and temperature dependent material properties. In those simulations, it was observed that the flow stress in the region of interest is constant (Deshpande *et. al.* 2010). This observation prompted new simulations wherein the work material is approximated as perfectly plastic (without work hardening), which permits interpretation of the observed flow around the cutting edge using the slip-line field theory for perfectly plastic materials. To approximate rigid perfectly plastic behavior, an artificially high value of Young’s modulus ( $E=21,000$  GPa) is used in the simulations. Since the yield strength ( $Y$ ) is only 0.8 GPa, the maximum elastic strain is very small ( $Y/E = 3.81e-5$ ).

The finite element mesh of the regions of the workpiece, chip and tool in the vicinity of the primary and secondary deformation zones is shown in Figure 4.1.

In order to account for the large gradients in the solution variables near the cutting edge and resolve the flow with improved accuracy, the workpiece in this region is meshed finely, with approximately 45 elements around the 6  $\mu\text{m}$  radius cutting edge. A typical 2D model consisted of 7,000 2D elements for the workpiece and an analytical rigid surface for the tool. A purely mechanical FE simulation was carried out using CPE4R (plane strain, quadrilateral, reduced integration) elements, since the material is perfectly plastic, with properties independent of temperature.

The density of the work material was scaled up by a factor of 100 in order to increase the critical time step size for stable explicit integration of the system equations. This caused some inertial effects in the results. The ratio of kinetic energy and the internal energy was found to be more than 10%. In order to reduce this ratio, the ALE simulation was carried out in three steps. In the first step, the cutting speed had a high value of 1m/s. Once a steady chip geometry was observed, the cutting velocity was reduced to 0.1m/s. As expected, the kinetic energy reduced

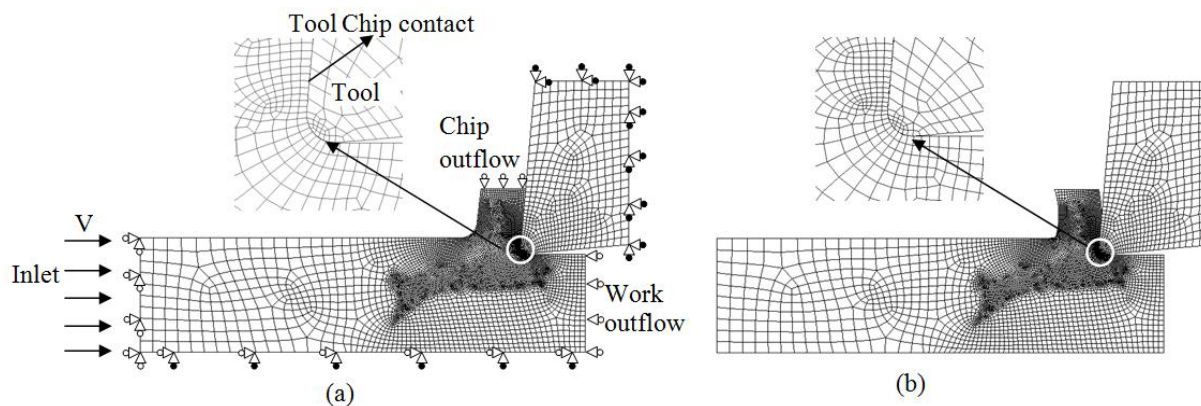


Figure 4.1: Initial and final chip geometry in the ALE thermomechanical analysis step. (a) Initial mesh and boundary conditions, and (b) shape of the chip when mechanical steady state has been attained.  $\circledast$ =Constraint on mesh,  $\circledcirc$ =Constraint on material

drastically but some oscillations were still observed in the velocity field near the cutting edge. In cases where the ratio of the kinetic energy to the internal energy were found to be large even after reducing the velocity to 0.1m/s, a third step of simulation with the cutting velocity further reduced to 0.01m/s, was carried out. Since a perfectly plastic material model was used, the change in velocity is not expected to have any other effects on the cutting process outputs.

Once steady state was reached at the lowest velocity, the velocity, displacement, strain, and stress fields were extracted at multiple times during steady state and averaged to further reduce the noise. In order to completely eliminate inertial effects, a second Lagrangian simulation was carried out. The average displacement fields obtained from the ALE simulation were used as initial values for the Lagrangian simulation so that with a very small amount of incremental deformation, steady state could be achieved in the Lagrangian simulation. This simulation was carried without scaling the density of the workpiece. Also, the element type was changed to a full integration CPE4. The simulation was carried out for a small cutting distance of only 0.12 micrometers. Few simulations were carried out with limiting contact shear stress ( $m=\tau/k$ ) whereas, few simulations were carried out by defining a Coulomb friction coefficient ( $\mu$ ). The type of friction as well as its value has been mentioned during the discussion of results. The stresses, strains and velocities obtained at the end of this Lagrangian step were nearly the same as at the end of the ALE step, but with the inertial oscillations eliminated, and were used to generate the slip-line field solution.

A new FE based slip-line field generation approach has been developed where, the local directions of principal stresses and maximum shear stress were identified for each plastically deforming element based on the stress components  $\sigma_1$ ,  $\sigma_2$ , and  $\sigma_{12}$ . The direction of the principal stresses ( $\theta$ ) is obtained using the following relationship.

$$\theta = \frac{\arctan\left(\frac{\sigma_{12}}{\frac{(\sigma_{11}-\sigma_{22})}{2}}\right)}{2}; \eta_1 = \theta + \frac{\pi}{4}; \eta_2 = \theta + \frac{3\pi}{4} \quad (1)$$

The first and second directions of maximum shear stress ( $\eta_1$  and  $\eta_2$ ) which are the slip line directions for plastically deforming elements were calculated using the symbolic math package MAPLE™. The obtained maximum shear stress directions were then rearranged such that they are aligned to the maximum shear stress directions of the neighboring elements. The results were then imported in Tecplot and streamlines of these directions were plotted, which

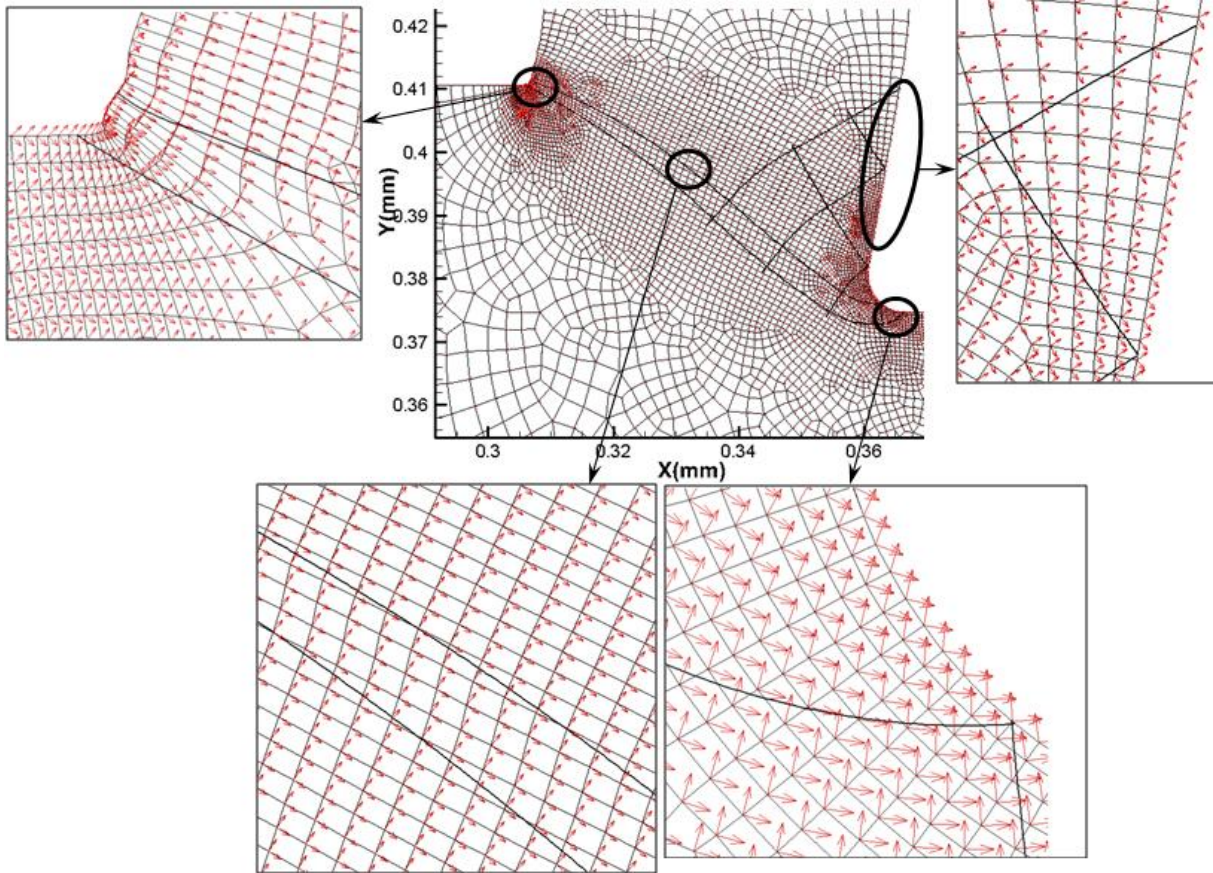


Figure 4.2: The workpiece was densely meshed in the region of interest. The 6  $\mu\text{m}$  edge radius was divided into 45 elements to capture the large deformation gradients in the region. The pair of orthogonal red arrows indicate the first and second direction of the maximum shear stress at each node i.e. the slip-line directions. The insets show the slip-line direction in different regions of interest.

were the slip-lines. Figure 4.2 shows the first and second directions of the maximum shear stress in different regions of interest. This method of generating SLFs by FEA has been validated using the rough punch compression problem discussed elsewhere. The slip-line field and the hodograph obtained from FEA were found to match well with those given by Johnson and Mellor (1973), including the velocity discontinuities.

#### 4.5 Effect of Mesh Alignment

As described previously, the alignment of the mesh with the slip-line field plays an important role in capturing the velocity discontinuities correctly. Hence, one additional iteration of simulations was carried out where the geometry of the slip-lines from the previous Abaqus/Standard results was used to generate a new mesh.

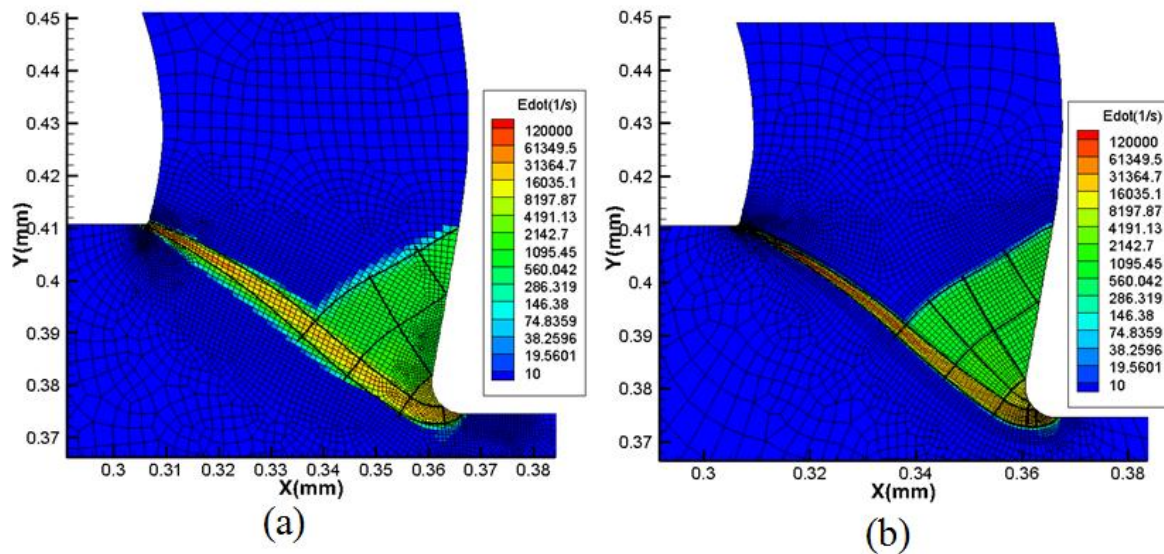


Figure 4.3: The alignment of the mesh is important to capture the velocity discontinuities correctly, as can be seen from (a) The mesh is not along the slip-lines and (b) the mesh is aligned to the slip-lines. The above results are for cutting with a 6 μm edge radius tool having 10 degree rake angle. The depth of cut was 36μm and the friction coefficient was zero.

Figure 4.3 compares the slip-lines obtained from a simulation with regular mesh and the one where the mesh was aligned to the slip-lines. It can be clearly seen that the width of the deformation zone changes significantly when the mesh is aligned with the slip-lines. For this reason, all the results reported are for simulations where the mesh was aligned to the slip-lines.

#### 4.6 Verification of Attainment of Steady State

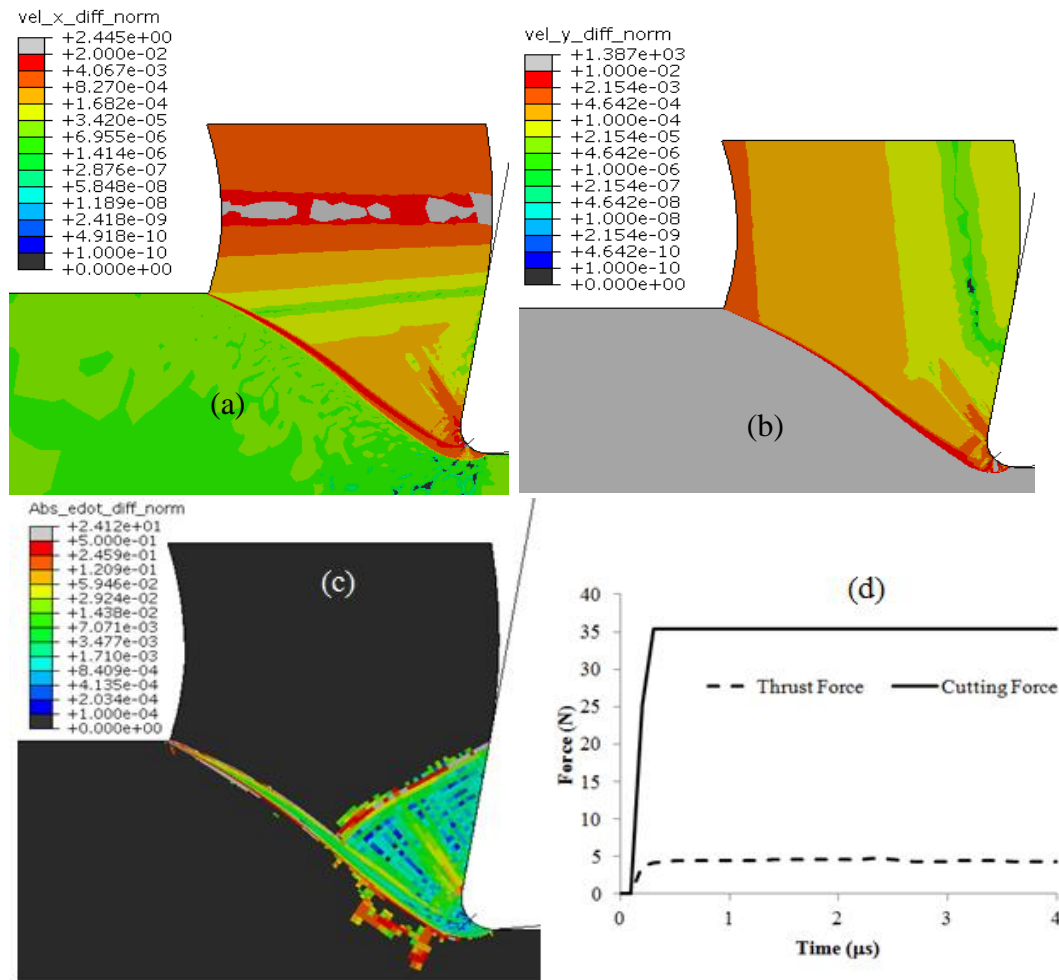


Figure 4.4: The velocity field was obtained at two time intervals in the simulation. For the cutting velocity of 0.1 m/s, (a) The absolute difference in X component of the velocity in the region of interest was extremely small of the order of  $1e-3$  and (b) the absolute difference in Y component of velocities also was very small. Similarly, strain rates were calculated at two different time interval and their difference was divided by the strain rate itself. (c) In the region of interest, this normalized difference in the strain rate is very small. (d) the cutting forces were plotted as a function of time and were found to be constant

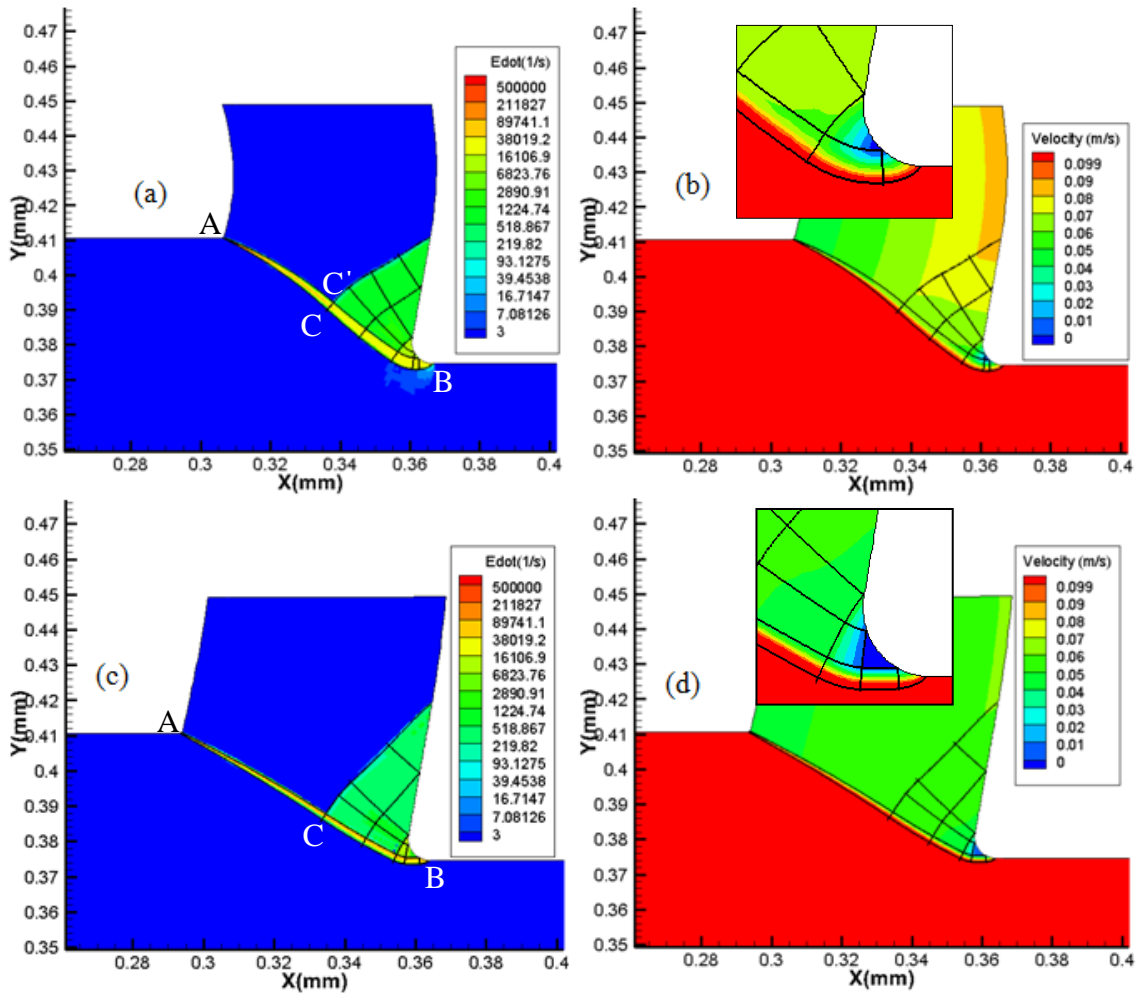


Figure 4.5: The slip-line field obtained for cutting with a tool of 10 degree rake angle and 6  $\mu\text{m}$  edge radius is superimposed on the (a) strain rate for value of  $m=0$ , (b) velocity for value of  $m=0$ , (c) strain rate for value of  $m=0.50$ , and (d) velocity for value of  $m=0.50$ . A constant depth of cut of 36  $\mu\text{m}$  was used in all the simulations

In order to make sure that steady state cutting had been achieved, various checks were carried out for each machining simulation. The velocity field was obtained at two different tool displacements in the simulation. The difference in X component and Y component of velocities was calculated. This difference was then normalized by dividing it with the corresponding velocity component.

This normalized difference in the X and Y component of velocity is shown in Figure 4.4(a) and Figure 4.4(b) respectively and was found to be very small. Similarly, strain rates were

calculated at two different tool displacements in the simulation and their difference was divided by the strain rate itself. This normalized strain rate is shown in Figure 4.4(c). In the region of interest, this normalized difference in the strain rate was found to be very small. The cutting forces were plotted as a function of the cutting tool displacement and were found to be constant as shown in Figure 4.4(d). All these quantities shown in Figure 4.4 are for cutting with a tool having 10 degree rake angle and 6  $\mu\text{m}$  cutting edge radius. The depth of cut was 36  $\mu\text{m}$  and the friction coefficient was zero. This verification of attainment of steady state was carried out for all the cutting simulations reported in this work.

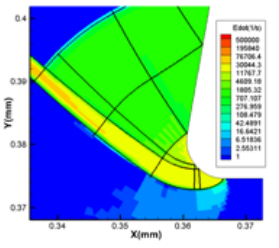
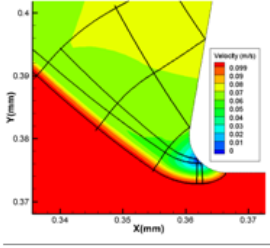
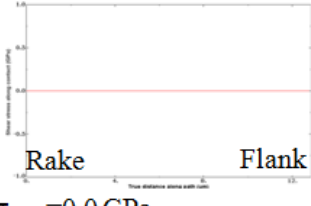
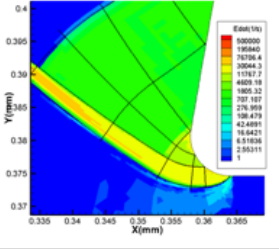
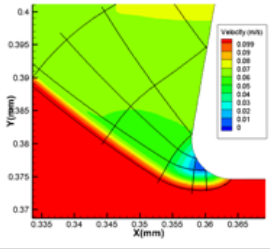
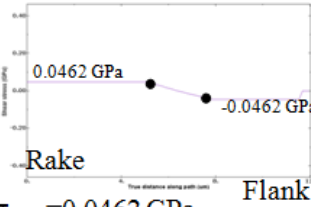
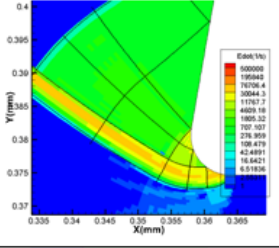
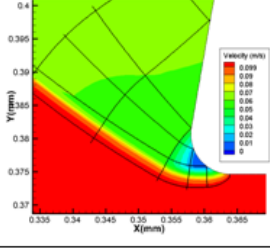
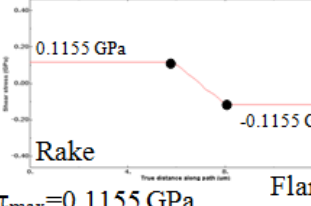
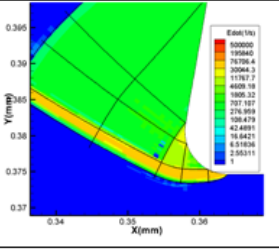
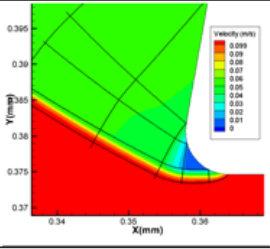
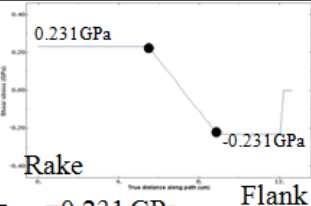
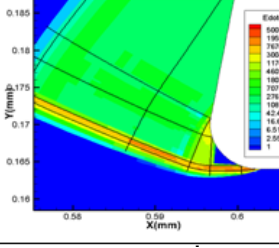
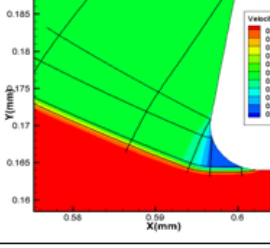
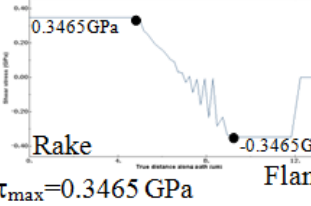
#### **4.7 Effect of Friction Along the Chip-Tool Contact**

In order to study the effect of friction along the chip-tool contact on the slip-line field, various simulations were carried out for different values of ‘ $m$ ’ which is nothing but the ratio of maximum shear stress ( $\tau_{max}$ ) to the shear strength of the material ( $k$ ).

The rake angle of the tool was kept constant at 10 degrees along with 6 $\mu\text{m}$  cutting edge radius. Also, the depth of cut was constant at 36  $\mu\text{m}$ . Figure 4.5(a) and Figure 4.5(b) show the slip-line field for  $m=0$  superimposed on the strain rate and the velocity magnitude respectively. Figure 4.5(c) and Figure 4.5(d) show the slip-line field for  $m=0.50$  superimposed on the strain rate and the velocity magnitude respectively. All the plots are at the same scale as well.

By comparing Figure 4.5(a) with Figure 4.5(c), it is clear that the curl in chip decreases as the value of  $m$  increases. This is reflected from Figure 4.5(b) and Figure 4.5(d) as well. From the contours of velocity in Figure 4.5(b) it can be seen that the chip velocity varies as one moves from the cutting edge to the free surface. Whereas, the variation in the velocity magnitude is very small for  $m=0.50$  case as seen in Figure 4.5(d). The chip thickness increases with increase in friction coefficient.

Table 4.1: The limiting shear stress factor ‘m’ was varied from m=0 to m= 0.75. The slip-line field superimposed on the strain rate and velocity distribution is shown along with the graph of contact shear stress distribution

Shear stress limit	Strain rate in the region of the cutting edge	Strain rate in the region of the cutting edge	Contact shear stress distribution from rake towards the flank
m=0			 $\tau_{max}=0.0 \text{ GPa}$
m=0.10			 $\tau_{max}=0.0462 \text{ GPa}$
m=0.25			 $\tau_{max}=0.1155 \text{ GPa}$
m=0.50			 $\tau_{max}=0.231 \text{ GPa}$
m=0.75			 $\tau_{max}=0.3465 \text{ GPa}$

The curvature of the beta slip-line representing the exit of the PSZ from point A to point C' also decreases as the friction increases. This decrease in the angle causes the exiting chip to be straight. Also, the length of contact increases as the friction increases.

For  $m=0.50$ , it can be observed in the inset that there is a region near the cutting edge where the velocities are extremely small. Corresponding region in the strain rate plot, shows significantly lower values than the neighboring region. This region was termed as the dead metal zone (DMZ). The DMZ collapses to a single point, for the case where  $m=0$  and can be termed as the stagnation point. From the velocity contours, the stagnation point for  $m=0$  and the DMZ for

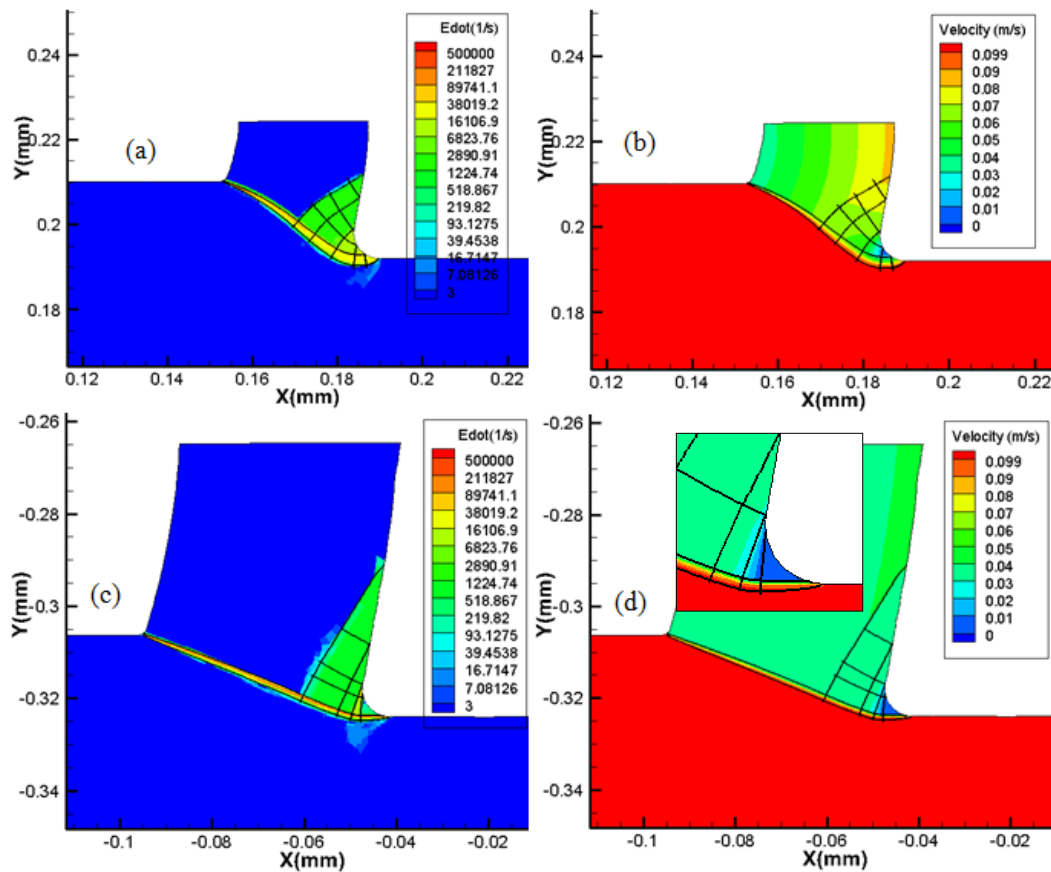


Figure 4.6: The slip-line field obtained for cutting with a tool of 10 degree rake angle and  $6 \mu\text{m}$  edge radius is superimposed on the (a) strain rate for value of  $\mu=0$ , (b) velocity for value of  $m=0$ , (c) strain rate for value of  $\mu=0.50$ , and (d) velocity for value of  $\mu=0.50$ . A constant depth of cut of  $36 \mu\text{m}$  was used in all the simulations

$m > 0$  are clearly visible. These regions have significantly lower velocity compared to the neighboring regions. The extent of the DMZ is found to increase with increase in the  $m$  value as will be shown later.

Figure 4.6 shows the slip-lines generated for simulations where a friction coefficient ( $\mu$ ) was specified rather than the value of the limiting frictional shear stress ( $m = \tau/k$ ). This means that each of the alpha line originating for the rake face of the tool would make a different angle with the rake face based on the local frictional shear stress value. Figure 4.6 (c) and Figure 4.6 (d) are for  $\mu = 0.5$ , and a significantly larger dead metal zone (DMZ) can be observed in the inset of Figure 4.6(d).

#### **4.8 Effect of Friction on the Size and Extent of the Dead Metal Zone (DMZ)**

Based on the initial observations, it appeared that the size and extent of the DMZ was affected significantly by the value of friction coefficient used along the tool-chip contact. Cutting simulations with constant cutting parameters and tool geometry parameters were carried out by varying the shear stress limiting factor ( $m$ ). Table 4.1, shows the strain rate and velocity magnitude for different 'm' values. Also, the distribution of the contact shear stress has been plotted for different values of 'm.' A closer observation of the velocity magnitudes in the region of the cutting edge reveals an almost triangular shaped zone of extremely small velocity. The size of this zone increases as the value of 'm' increases. This zone has been termed as the dead metal zone (DMZ). The same observation can be inferred by the magnitude of strain rates. It can be seen that the region of very small (significantly lower compared to the PSZ) strain rate develops at the cutting edge and its size increases as the value of 'm' increases.

Figure 4.7 has the magnitude of velocity for the same cutting condition of 36  $\mu\text{m}$  depth of cut with a rake angle of 10 degrees and cutting edge radius of 6 $\mu\text{m}$ . The contour values are set

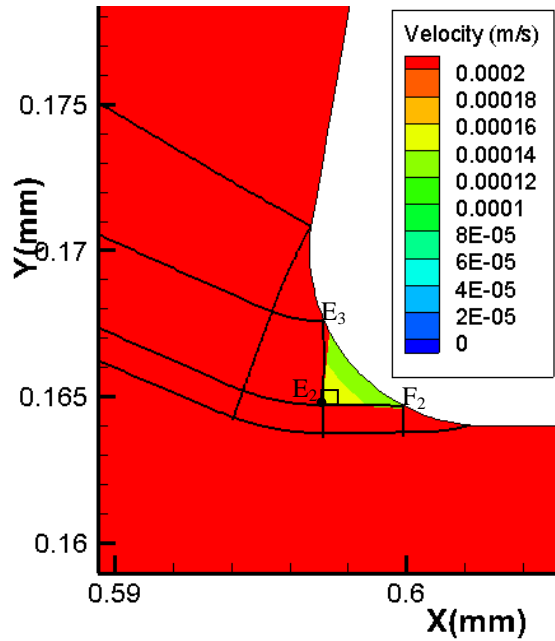


Figure 4.7: The tightened contours of velocity magnitude in the region of the cutting edge show that the velocity magnitude inside the DMZ is less than  $2e-4$  m/s corresponding to the cutting velocity of 1m/s. The rake angle of the tool is 10 degrees and the cutting edge radius is  $6\mu\text{m}$ . The depth of cut is  $36\mu\text{m}$  and the limiting shear stress factor ( $m$ ) = 0.75

such that the variation of velocity inside the DMZ  $F_2E_2E_3$  would be clear. It can be seen that the velocity inside the DMZ is less than  $2e-4$  m/s corresponding to the cutting velocity of 1m/s. Another important thing to note is that the included angle of the DMZ is 90 degrees. This is clear from the slip-lines bounding the DMZ, which intersect each other at 90 degrees at point  $E_2$ .

Further, it can be seen from the contact shear stress distribution along the cutting edge as shown in the third column of Table 4.1, that the shear stress drops below the limiting value.

Initially, it was thought that this is due to the contact region being inside the DMZ. In the process of detailed investigation it was found that the length along the cutting edge where the contact shear stress is below the maximum shear stress limit is also affected by the value of slip tolerance used in Abaqus simulations. The default value of  $5e-3$  for slip tolerance was used for all the simulations. Tightening the slip tolerance value too much resulted in simulation convergence problems. Hence, the value of the slip tolerance was reduced to  $1e-5$ . Figure 4.8 shows the effect of tightening the slip tolerance on the contact shear stress distribution. Tightening the slip tolerance by a factor of 500 led to about  $0.75 \mu\text{m}$  decrease (equivalent to about length of three elements) in the region where the contact shear stress was less than the expected value of 0.231 GPa. In Figure 4.9, it can be seen that by

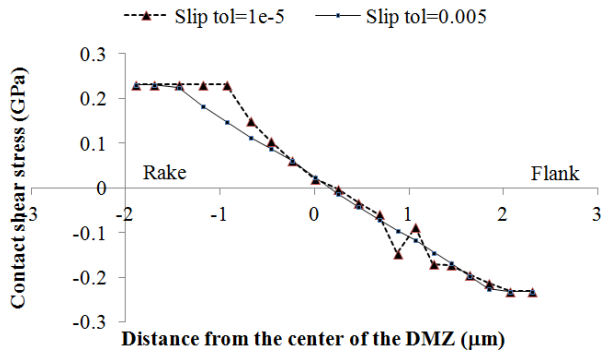


Figure 4.8: The contact shear stress was plotted along the cutting edge for simulations with slip tolerance values of  $5e-3$  and  $1e-5$  respectively. The cutting condition was  $36\mu\text{m}$  depth of cut with a cutting tool having 10 degree rake angle and  $6\mu\text{m}$  edge radius

DMZ might be non zero.

#### 4.9 Effect of the Depth of Cut and the Radius of the Cutting Edge

Another important factor affecting the slip-lines for metal cutting would be the depth of cut (DOC) and the radius of the cutting edge ( $r_c$ ). In order to investigate the effect of the depth on the slip-line field, additional simulations were carried out by varying the depth of cut and

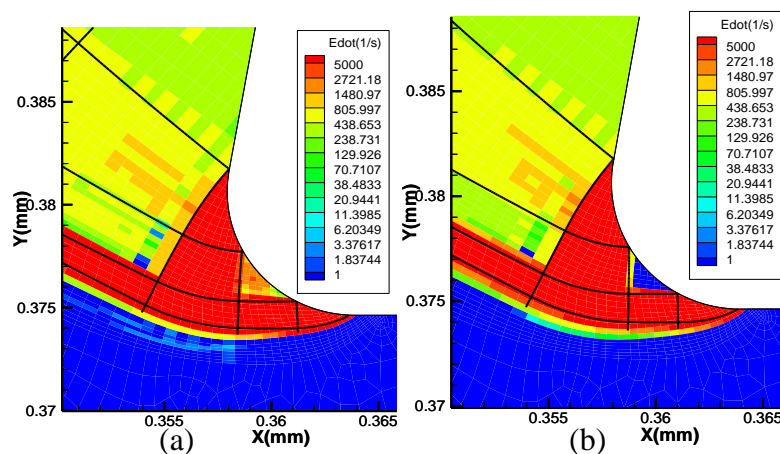


Figure 4.9: Comparison of the strain rate with slip-tolerance of (a)  $5e-3$  and (b)  $1e-5$ , shows that the indeed, the strain rate inside the dead metal zone drops to zero. With the default value, the strain rates have small non zero value.

tightening the slip tolerance by 5,000 gave zero strain rates in the DMZ as expected. The difference might not seem to be significant in case where the DMZ is large (i.e. large values of ' $m$ ') and its bounds exceed the contact area affected by the slip tolerance. However, for smaller values of friction, the DMZ is small compared to the contact area affected by the slip tolerance. Hence, the velocities inside the

keeping the other parameters like the radius of the cutting edge, rake angle, and friction coefficient constant. Figure 4.10 shows the overlapped slip-line fields obtained for depth of cut values of  $18\mu\text{m}$  and  $36\mu\text{m}$ . The radius of the cutting edge was held constant at  $6\mu\text{m}$ . From Figure 4.10(a),

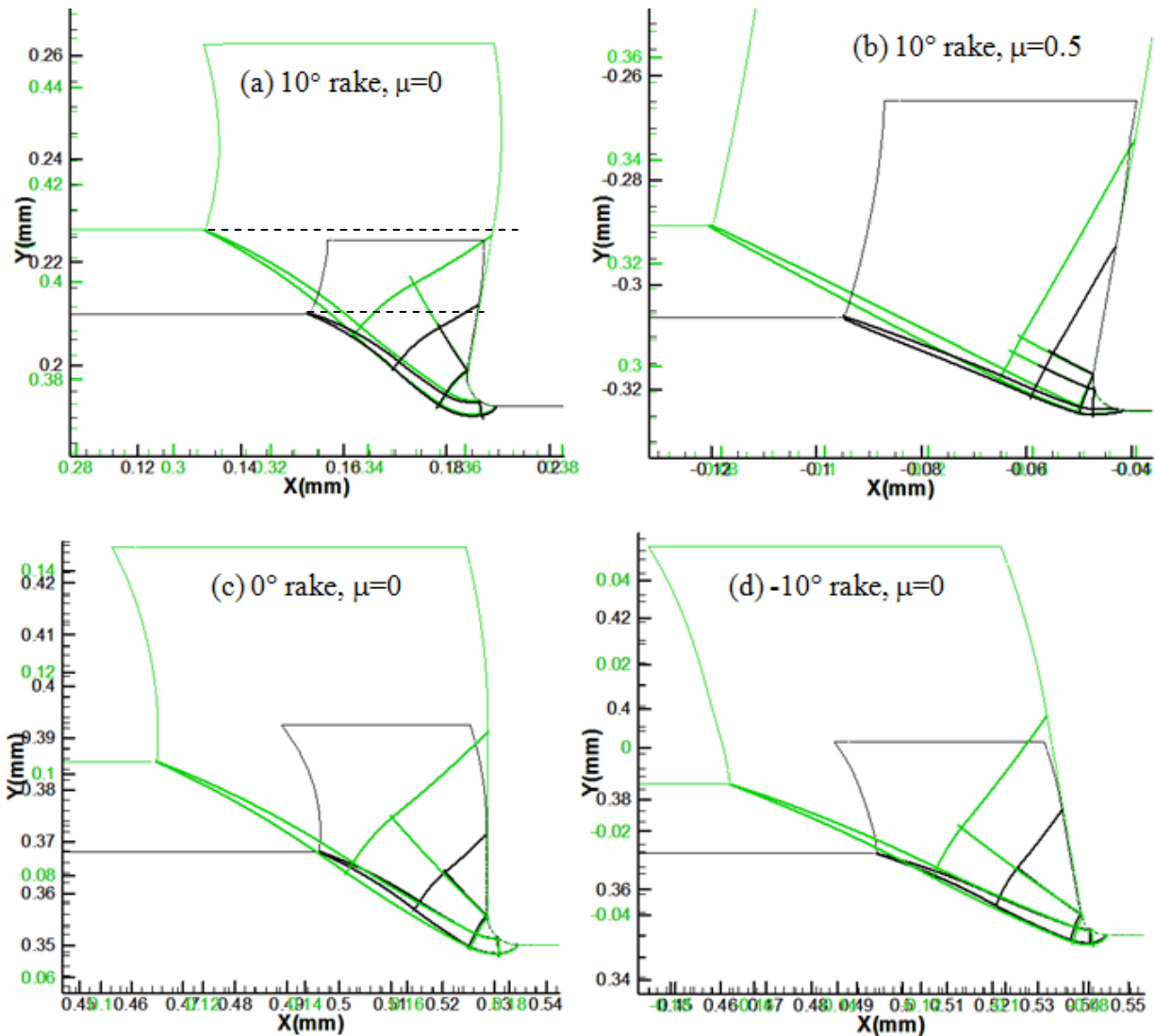


Figure 4.10: In order to understand the effect of the depth of cut, the slip-line fields obtained for depth of cut of  $18\mu\text{m}$  (black color field) and  $36\mu\text{m}$  (green color field), were overlapped on one another for (a)  $10^\circ$  rake and  $\mu=0$ , (b)  $10^\circ$  rake and  $\mu=0.50$ , (c)  $0^\circ$  rake and  $\mu=0$ , and (d)  $-10^\circ$  rake and  $\mu=0$

which is for the rake angle of  $10^\circ$  and friction coefficient ( $\mu$ ) of zero, it can be seen that the slip-lines obtained from both the depth of cuts match exactly with each other in the region of the cutting edge. In Figure 4.10(b), where the friction coefficient ( $\mu$ ) is 0.50, the geometry of the DMZ observed matches exactly for both the depth of cut values. From Figure 4.10(a), Figure 4.10(c), and Figure 4.10(d), which are for  $10^\circ$ ,  $0^\circ$ , and  $-10^\circ$  rake angle respectively, there is exact matching of the slip-line field in the vicinity of the cutting edge.

Since the contact length almost doubles for the 36 $\mu\text{m}$  depth of cut compared to the 18 $\mu\text{m}$  depth of cut, the alpha slip-lines in the secondary shear zone (SSZ) do not overlap. However, the changes in angles for the slip-lines for 18 $\mu\text{m}$  DOC are same as that for the 36 $\mu\text{m}$  DOC. This can be inferred from the fact that in the SSZ region, the alpha slip-lines for the 18 $\mu\text{m}$  DOC are parallel to the slip-lines for 36 $\mu\text{m}$  DOC.

Another interesting thing to note is that the maximum width of the primary shear zone (PSZ) is same at all the DOCs. This indicates that the maximum width of the PSZ is governed only by the value of the radius of the cutting edge. Based on the various observations above, it can be said that the slip-line field can be scaled for different DOCs and hence, is independent of the DOC.

In order to evaluate the effect of the radius of the cutting edge on different parameters of the slip-line field it was required to carry out simulations at different values of the radius of the

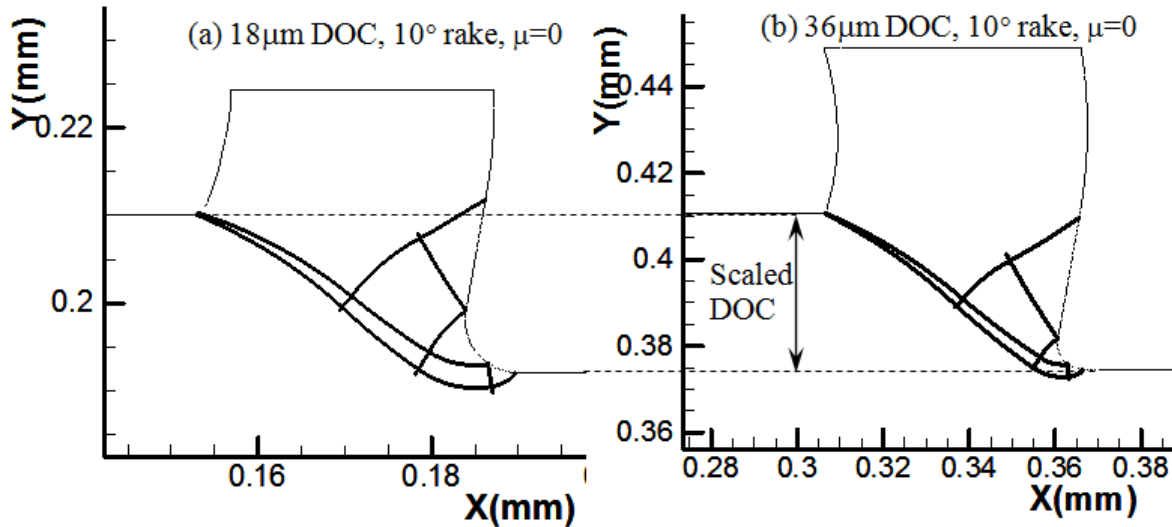


Figure 4.11: The slip-line field for the depth of cut of (a) 18 $\mu\text{m}$  DOC was compared with (b) the scaled down field of 36 $\mu\text{m}$  DOC. The 36 $\mu\text{m}$  DOC field was scaled down by a factor of two so that the 36 $\mu\text{m}$  DOC would appear to be 18 $\mu\text{m}$ . This way, the radius of the cutting edge would also scale down by the same factor. The rake angle was 10 $^\circ$  and the friction coefficient ( $\mu$ ) was zero.

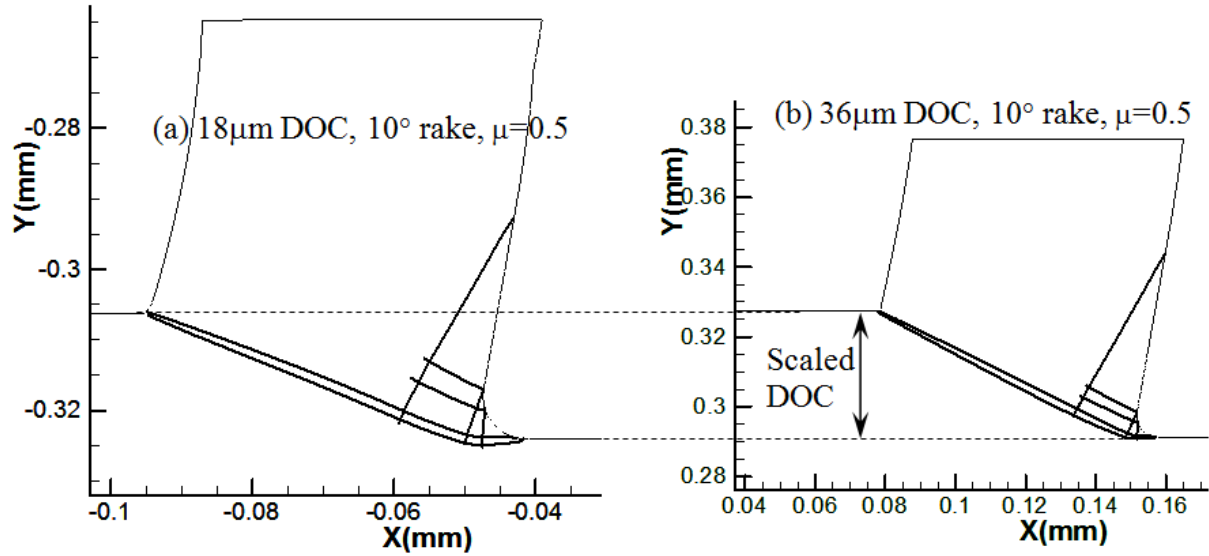


Figure 4.12: The slip-line field for the depth of cut of (a)  $18\mu\text{m}$  DOC was compared with (b) the scaled down field of  $36\mu\text{m}$  DOC. The  $36\mu\text{m}$  DOC field was scaled down by a factor of 2 so that the  $36\mu\text{m}$  DOC would appear to be  $18\mu\text{m}$ . This way, the radius of the cutting edge would also scale down by the same factor. The rake angle was  $10^\circ$  and the friction coefficient ( $\mu$ ) was 0.50

cutting edge. Each simulation is computationally very expensive and adding one more factor like the radius of the cutting edge would increase the number of required simulations. The previous observation of the slip-line field being independent of the depth of cut was utilized to full advantage. As can be seen in Figure 4.11, the slip-line field obtained for a DOC of  $36\mu\text{m}$  was scaled down by a factor of two, so that the scaled DOC would be equal to  $18\mu\text{m}$ . Figure 4.11(a) is the simulation with  $18\mu\text{m}$  DOC and Figure 4.11(b) is the simulation with DOC scaled down to  $18\mu\text{m}$ . In the process of scaling the slip-line field, even the radius of the cutting edge get scaled down by a factor of two as well. Now a one to one comparison can be carried out between Figure 4.11(a) and Figure 4.11(b) to understand the effect of the radius of the cutting edge. While Figure 4.11 corresponds to a friction coefficient of zero, Figure 4.12 corresponds to a friction coefficient of  $\mu=0.50$ . The rake angle of the tool was  $10^\circ$ .

From the comparison in Figure 4.11, it can be seen that the maximum width of the PSZ is directly proportional to the radius of the cutting edge. It is also clear that the chip thickness is

proportional to the cutting edge radius. For smaller value of the cutting edge radius, the chip appears to be thinner i.e. the shear plane angle decreases as the radius of the cutting edge increases. From Figure 4.12 it can also be inferred that the size of the DMZ is proportional to the radius of the cutting edge.

#### 4.10 Effect of the Rake Angle

Another important cutting tool parameter is the rake angle of the tool. A set of simulations was carried out keeping the depth of cut, the friction coefficient, and the radius of the cutting edge constant. Three values of rake angle i.e.  $10^\circ$ ,  $0^\circ$ , and  $-10^\circ$  were simulated.

One such data set is shown in Figure 4.13. It can be observed from Figure 4.13 (a1), (b1), and (c1), that the chip thickness increases as the rake angle decreases. Also, from the contours of velocity in Figure 4.13 (a2), (b2), and (c2), the curl in the chip decreases as the rake angle decreases. However, the maximum width of the PSZ appears to be constant irrespective of

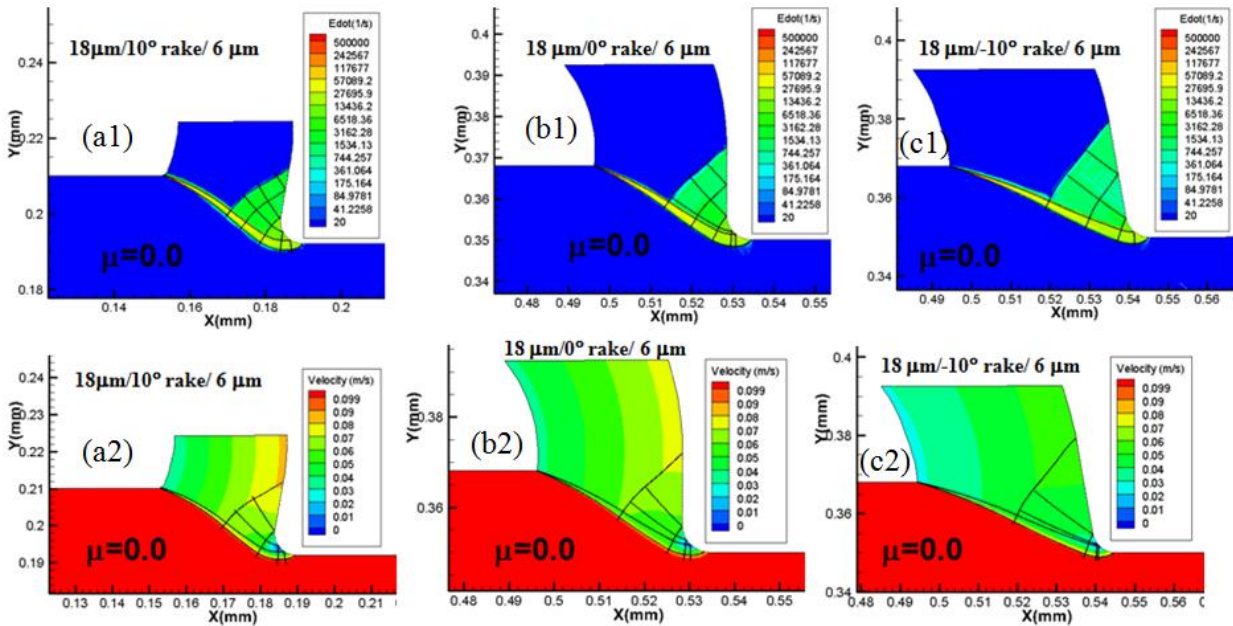


Figure 4.13: Simulations with a depth of cut of  $36 \mu\text{m}$  and friction coefficient of  $m=0$  were carried out at rake angles of (a)  $+10$  degrees, (b)  $0$  degrees, and (c)  $-10$  degrees

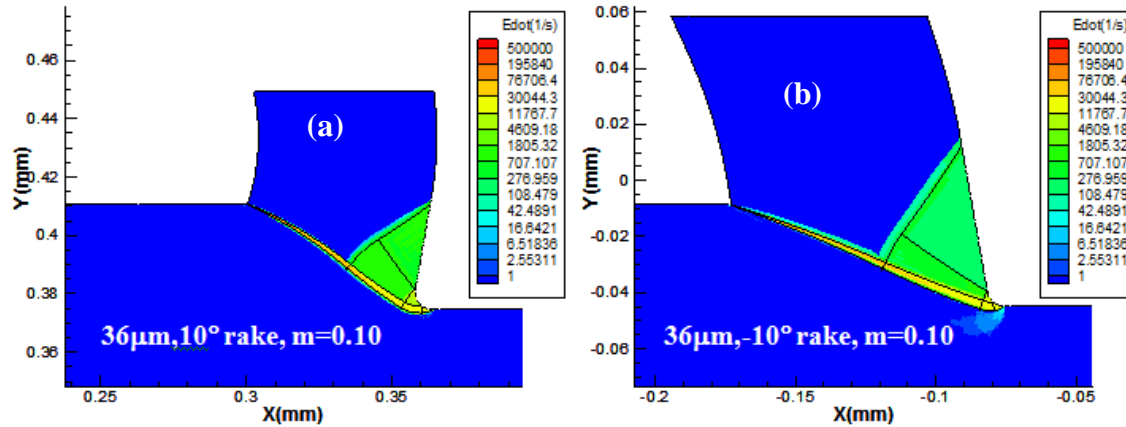


Figure 4.14: Simulations with a depth of cut of 36  $\mu\text{m}$  and limiting contact shear stress factor ‘ $m$ ’ of 0.1 were carried out at rake angles of (a)  $+10^\circ$ , (b)  $-10^\circ$

the rake angle. The depth of cut of 18  $\mu\text{m}$  and the friction coefficient of  $\mu=0.0$  were kept constant for all the simulations in Figure 4.13. A set of simulations with rake angles of  $10^\circ$  and  $-10^\circ$  with DOC of 36  $\mu\text{m}$  and cutting edge radius of 6 $\mu\text{m}$  were carried out. The contact shear stress limiting factor was ‘ $m$ ’ was constant at 0.1. As can be seen in Figure 4.14(a) and Figure 4.14(b), even for non zero friction, the same observations are valid. The chip curl decreases as the rake angle decreases. The shear plane angle decreases as the rake angle decreases, making the chip thicker.

Also, since the friction along the chip-tool contact is same for all the conditions, the angles made by the alpha slip-line with the rake face of the tool is same in all the cases.

#### 4.11 Discussion on Different Regions of the Field

An attempt has been made to develop a generalized slip-line model for metal cutting, based on the results of multiple FE simulations under varying rake angle, friction coefficient, and the DOC. This generalized slip-line field model is shown in Figure 4.15. The most important aspects of this slip-line field are the regions near the cutting tool tip. The  $E_3E_2F_2$  is termed as the dead metal zone. The strain rates inside the DMZ are almost equal to zero as can be seen from figure Figure 4.9 It should be noted that the DMZ is not symmetric along the entire included

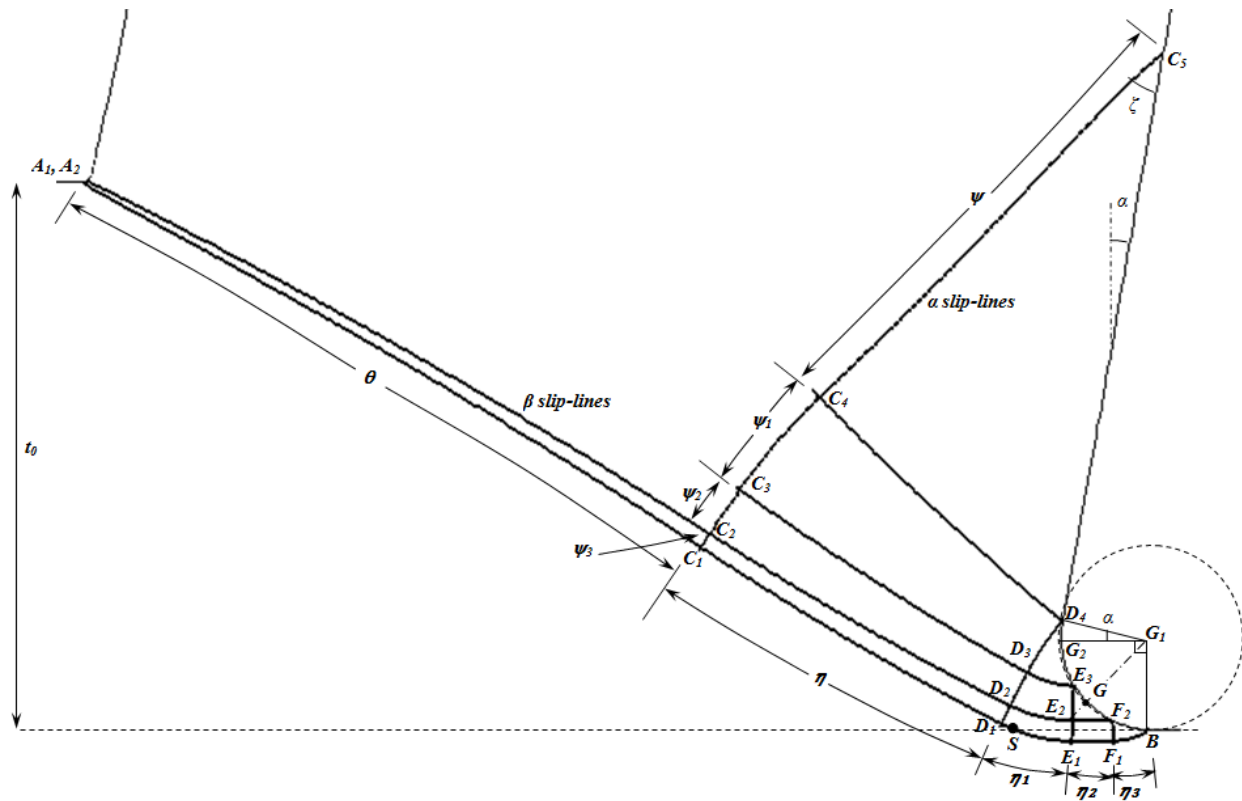


Figure 4.15: The slip-line field model for a tool with finite cutting edge radius developed based on the stress and velocity data obtained from the Finite Element Analysis simulations. It can be seen that the entire deformation reaching the free surface of the chip originates below the lower boundary of the Dead Metal Zone.

angle of the cutting edge, but symmetric about  $GG_1$ , i.e. along the angle bisector of the 90 degree included angle. The slip-lines  $E_2F_2$  and  $E_2E_3$  form the boundaries of the DMZ. Both the lines meet each other orthogonally at point  $E_2$ , which is the tip of the DMZ. These slip-lines make an angle of  $\zeta$  with the tangent of the cutting edge in order to satisfy the imposed friction condition. The points  $E_3$  and  $F_2$  move further away from the center  $G$  as the value of limiting frictional shear stress 'm' increases. It has been found that the DMZ exists under all friction conditions where  $m > 0$ . Another observation shows that the slip-lines  $E_2E_3$  and  $E_1F_1$  are straight. This means that under most cutting conditions the angle subtended by these lines i.e.  $\eta_2$  and  $\psi_2$ , are zero.

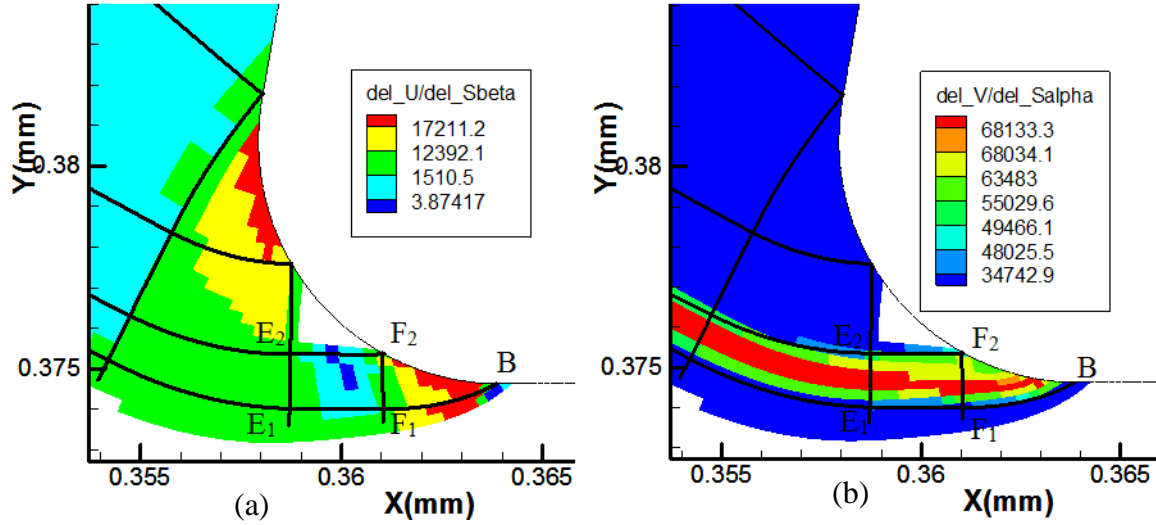


Figure 4.16: The components of the strain rate (a)  $\frac{\partial u}{\partial s_\beta}$  and (b)  $\frac{\partial v}{\partial s_\alpha}$  were plotted for the  $E_2F_2BF_1E_1$  region. It can be seen that the  $\frac{\partial v}{\partial s_\alpha}$  component is the main contributor for the strain rate in this region of the slip-line field. The plots were generated for  $36\mu\text{m}$  DOC,  $10^\circ$  rake,  $6\mu\text{m}$  cutting edge and  $m=0.5$

The DMZ is surrounded by the retarded flow zones on either sides. The region  $E_1E_2F_2BF_1$  is the retarded flow zone along the lower boundary of the DMZ. This retarded flow zone can be divided in to two regions i.e.  $F_1F_2B$  and region  $E_1E_2F_2F_1$ . The change of angle from  $F_1$  to  $F_2$  is termed as  $\psi_3$ . Since the length  $F_1F_2$  is very small, it can be assumed that the angle  $\psi_3$  is equal to zero. This helps in estimating the length  $F_1F_2$ , which also happens to be the maximum width of the PSZ. The horizontal line from B bisects the segment  $F_1F_2$ . It is easy to estimate the half length of segment  $F_1F_2$  based on trigonometry. The angle  $F_2G_1B$  is  $\zeta = \frac{1}{2} \cos^{-1}(m)$ . This gives the angle  $SBF_2$ , to be equal to  $\frac{\zeta}{2}$ . If  $r_e$  is the radius of the cutting edge, the half length of  $F_2F_1$  can be given by following equation

$$\frac{\text{length}(F_2F_1)}{2} = r_e * \zeta * \cos\left(\frac{\zeta}{2}\right) \quad (2)$$

Thus, the maximum width of the PSZ i.e. length  $(F_2F_1)$ , can be easily determined by the above equation. It is also clear that the maximum width of the PSZ depends only on the radius

of the cutting edge and the friction along the chip-tool interface. In  $F_1F_2B$  RFZ region, the PSZ deformation originates and the maximum shearing happens along the beta slip-lines. For this reason, the total strain rate is dominated by the  $\frac{\partial v}{\partial S_\alpha}$  term, which is the gradient of the velocity along the beta slip-line in the direction of the alpha slip-line as can be seen in Figure 4.16.

The next region is  $E_1E_2F_2F_1$ , which can be treated as a rectangular region since all the angles are very small. Similar to the  $F_1F_2B$  region, even in  $E_1E_2F_2F_1$  region of the slip-line field, the total strain rate is dominated by the  $\frac{\partial v}{\partial S_\alpha}$  term, which is the gradient of the velocity along the beta slip-line in the direction of the alpha slip-line. Figure 4.16 shows the plots of  $\frac{\partial v}{\partial S_\alpha}$  and  $\frac{\partial u}{\partial S_\beta}$  with contours set to reflect the values in region  $E_1E_2F_2F_1$ . Since, the angle  $\psi_3$  is zero,  $\text{length}(E_1E_2)=\text{length}(F_1F_2)$ , which implies that the width of the PSZ is constant in this slip-line region.

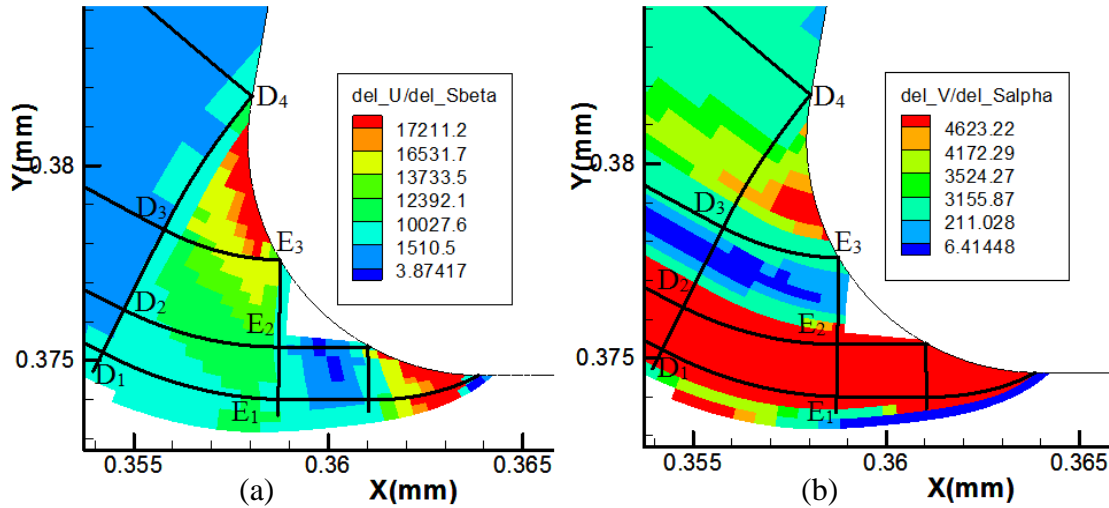


Figure 4.17: The components of the strain rate (a)  $\frac{\partial u}{\partial S_\beta}$  and (b)  $\frac{\partial v}{\partial S_\alpha}$  were plotted for the  $D_4D_3D_2E_2E_3$  region. It can be seen that the  $\frac{\partial v}{\partial S_\alpha}$  component is the main contributor for the strain rate in this region of the slip-line field. The plots were generated for 36 $\mu$ m DOC, 10 $^\circ$  rake, 6 $\mu$ m cutting edge and  $m=0.5$

The RFZ region  $D_4D_3D_2E_2E_3$  is located along the vertical boundary of the DMZ. The strain rate term  $\frac{\partial u}{\partial s_\beta}$  dominates in this region as can be seen in Figure 4.17. This region can be split in two regions i.e.  $D_3D_2E_2E_3$  and  $D_4D_3E_3$ . Since the angle  $\psi_2$  is found to be very small under almost all cutting conditions, the segments  $D_2D_3$  and  $E_2E_3$  are straight. The segments  $D_2E_2$  and  $D_3E_3$  are shown to be curved by angle  $\eta_1$ . The significance of this angle, which is also termed as the equivalent shear plane angle, is discussed in the later sections.

In the region  $D_3D_4E_3$ , the change in angle along the slip-line  $D_3D_4$  is  $\psi_1$  and the change in angle along the slip-line  $D_3E_3$  is  $\eta_1$ . By going around the loop  $D_3D_4E_3$  in this slip-line region, a simple relationship between these angles can be developed as given in equation below.

$$\zeta + \alpha = \eta_1 + \psi_1 \quad (3)$$

This angular relationship is extremely important to understand the effect of friction and rake angle on the shear plane angle, which is discussed later.

The next important region of the slip-line field is the  $E_1E_2D_2D_1$  region. This region is located on the boundary of both the retarded flow zones. It is here, that the shear originating from the cutting edge rotates upwards and reaches to the free surface forming the remaining of the primary shear zone.

Another interesting thing to note, is about the presence of point ‘S’, which is termed as the splitting point. This point is located at the intersection of the horizontal line drawn from the machined workpiece and the slip-line  $D_1E_1$ . Any material entering the shear zone above the point ‘S’ ends up being a part of the chip and any material which enters the shear zone below the point ‘S’ ends up in the machined workpiece. Figure 4.19 shows the streamlines of material flow indicating that the streamlines, which originates above the point S ends up in the chip and the ones originating below go to the machined workpiece. This region is in the primary shear zone

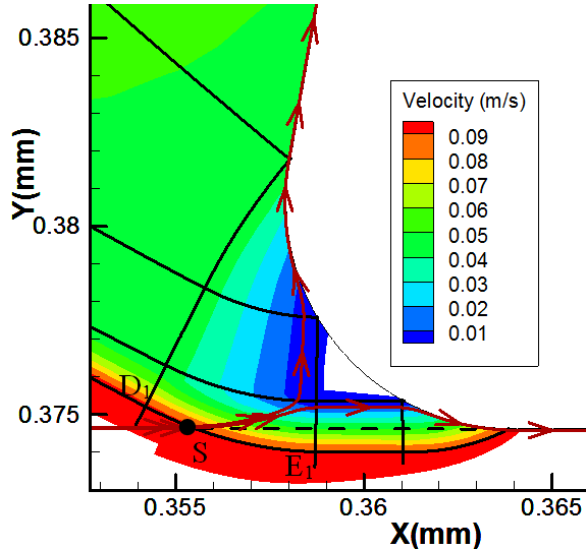


Figure 4.19: The lines with arrow marks, are the streamlines of velocity for the material passing just above and below the point ‘S’ which is termed as the splitting point. From the streamlines, it is clear that indeed, the material going above the point ‘S’ ends up in the chip and the material passing below the point ‘S’ ends up in the machined workpiece. The plots were generated for 36 $\mu$ m DOC, 10 $^\circ$  rake, 6 $\mu$ m cutting edge and m=0.5

and hence significant plastic deformation is induced in this region. Again, Figure 4.18 shows that the  $\frac{\partial v}{\partial s_\alpha}$  term is the dominating term indicating that significant amount of shear travels along the PSZ.

The region  $D_1C_1AC_2D_2$  is termed as the primary shear zone. The width of this zone decreases from length  $(D_1D_2)$  to zero at point in a linear fashion. As the width decreases linearly, the shear strain rate across this zone can be shown to increase linearly. This shear zone can be divided in

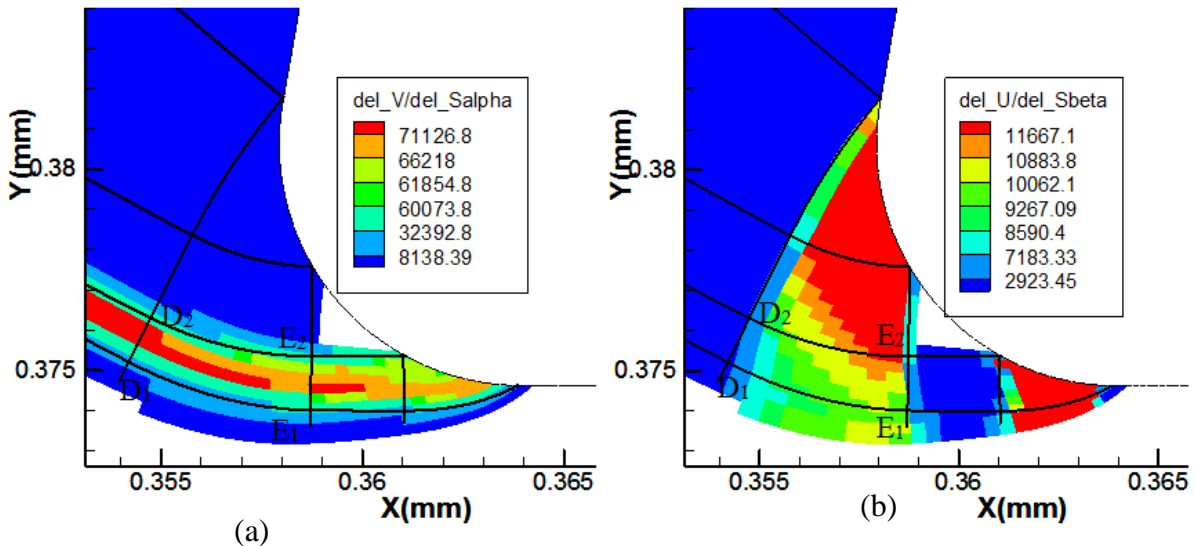


Figure 4.18: The components of the strain rate (a)  $\frac{\partial u}{\partial s_\beta}$  and (b)  $\frac{\partial v}{\partial s_\alpha}$  were plotted for the  $D_4D_3D_2E_2E_3$  region. It can be seen that the  $\frac{\partial v}{\partial s_\alpha}$  component is the main contributor for the strain rate in this region of the slip-line field. The plots were generated for 36 $\mu$ m DOC, 10 $^\circ$  rake, 6 $\mu$ m cutting edge and m=0.5

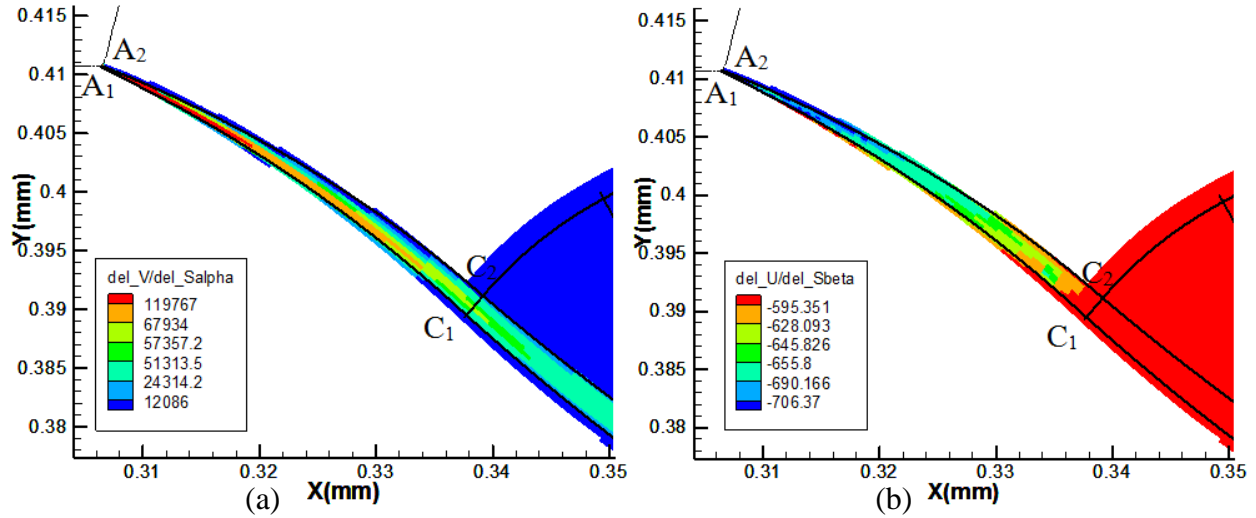


Figure 4.20: The components of the strain rate (a)  $\frac{\partial u}{\partial s_\beta}$  and (b)  $\frac{\partial v}{\partial s_\alpha}$  were plotted for the  $D_4D_3D_2E_2E_3$  region. It can be seen that the  $\frac{\partial v}{\partial s_\alpha}$  component is the main contributor for the strain rate in this region of the slip-line field. The plots were generated for  $36\mu\text{m}$  DOC,  $10^\circ$  rake,  $6\mu\text{m}$  cutting edge and  $m=0.0$

to  $C_1C_2D_2D_1$  and  $C_1AC_2$ . The region  $C_1C_2D_2D_1$  further rotates upwards by angle  $\eta$ . It can be noted that this angle  $\eta$ , is significantly smaller compared to the angle  $\eta_1$  seen in the previous region of the plastic deformation. The included angle  $\psi_3$  has been already assumed to be zero. This assumption has been made since not only the change in angle is small, but also the distance between the two beta slip-lines ( $C_1C_2$  or  $D_1D_2$ ) is very small.

Further, the slip-line region  $C_1AC_2$  is the remaining part of the primary shear zone. Its shape can be said to be similar to a doubly curved centered fan field. The width of the PSZ becomes zero at the free surface as the point  $A_1$  and  $A_2$  collapse on each other. This gives rise to a stress singularity at the point A. The angle change from A to C is  $\theta$ . The curvature of the chip is determined by this angle. For lower friction, the angle  $\theta$  is found to be higher, indicating larger chip curl. As the friction increases, the change in angle  $\theta$  decreases making the chip almost straight. The dependency of angle  $\theta$  has been discussed later. Figure 4.20, shows the

plots of two main strain rate terms i.e.  $\frac{\partial u}{\partial s_\beta}$  and  $\frac{\partial v}{\partial s_\alpha}$ . The contribution of the  $\frac{\partial v}{\partial s_\alpha}$  term is significantly higher than the  $\frac{\partial u}{\partial s_\beta}$  term. The contribution of the  $\frac{\partial u}{\partial s_\beta}$  term is almost zero. The small negative value indicates shear in the opposite direction.

The field  $C_5C_4D_4$  is termed as the secondary shear zone (SSZ). This region of the slip-line field is straightforward. All the alpha lines originating from the chip tool contact are inclined to the rake face at an angle of  $\zeta$ , which is the friction angle. The slipline  $C_5C_4$  forms the boundary of the SSZ. The change in angle from  $C_5$  to  $C_4$  is shown to be  $\psi$ . The lower boundary of this zone is formed by the slip-line  $C_4D_4$ . The change in angle of this lower boundary is  $\eta$  as

shown earlier. Even for very small friction, where the friction angle is almost equal to  $45^\circ$ , the angle  $\psi$  and  $\eta$  are found to be very small. By going around the loop of slip-lines in this region, a relationship between different angles was developed as shown below

$$\eta = \psi \quad (4)$$

Figure 4.21 shows the difference in the strain rate magnitudes for different regions in the slip-line field. The strain rates in the primary shear zone and the retarded flow zones are significantly higher than the strain

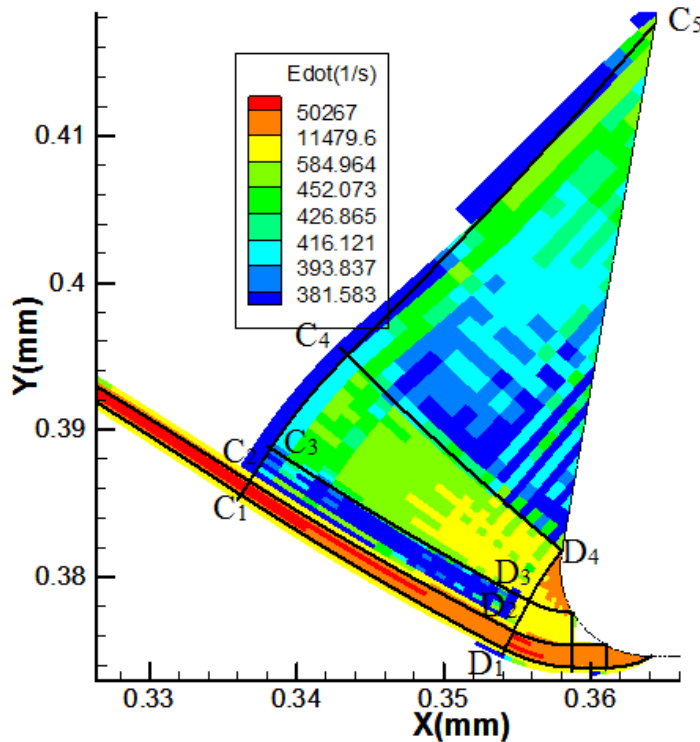


Figure 4.21: The strain rate in the secondary shear zone is very small in the range of 500/s whereas, in the primary shear zone, it is  $>50,000/s$ . The RFZ in front of the DMZ shows strain rate of the order of 10,000/s. The plots is for  $36\mu\text{m}$  DOC,  $10^\circ$  rake,  $6\mu\text{m}$  cutting edge and  $m=0.5$

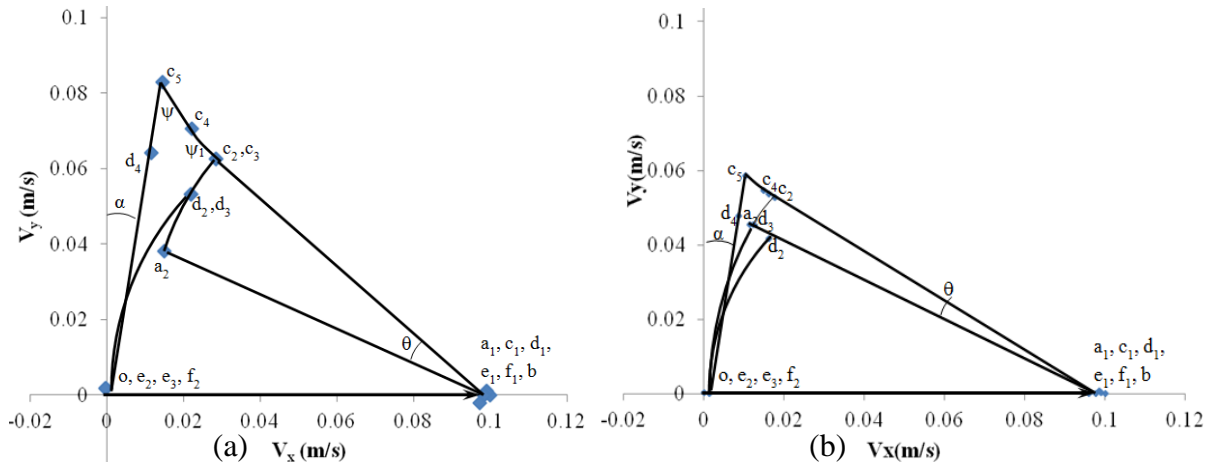


Figure 4.22: The hodograph was generated for (a)  $m=0$  and (b)  $m=0.50$  friction. The velocity values at different points in the slip-line field were obtained from FEA. The other cutting parameters were  $36 \mu\text{m}$  DOC,  $10^\circ$  rake, and  $6 \mu\text{m}$  edge radius of the tool. The cutting velocity was  $0.1 \text{ m/s}$

rates observed in the secondary shear zone. This indicates that most of the deformation happens in these zones itself. The slip-line region  $C_2D_2D_3C_3$  shows extremely small strain rates. The region  $D_3D_4C_4C_3$ , which corresponds to the field originating from the upper region of the cutting edge shows high strain rates.

After discussing about the deformation and the strain rate patterns in different regions of the slip-line field it would be interesting to study the velocities with the help of hodographs. The hodographs were generated for different cutting conditions by obtaining the velocity components from the FE simulations under different cutting conditions. Figure 4.22 (a) and Figure 4.22 (b) shows the hodographs obtained under different values of friction. The effect of friction on different angles in the slip-line field can be studied by comparing the two hodographs. The angle  $\theta$  decreases as the friction increases. It can also be seen that, since there is no dead metal zone for  $m=0$  case, the point  $D_3$  collapses on  $D_2$  and similarly  $C_3$  merges with  $C_2$ . Also, the point  $E_3$  and  $E_2$  become the same point. DMZ collapses to a single point on the cutting edge at G.

The hodograph obtained from simulations with two different depths of cut were overlapped on one another in order to understand the chip curl as shown in Figure 4.23. The

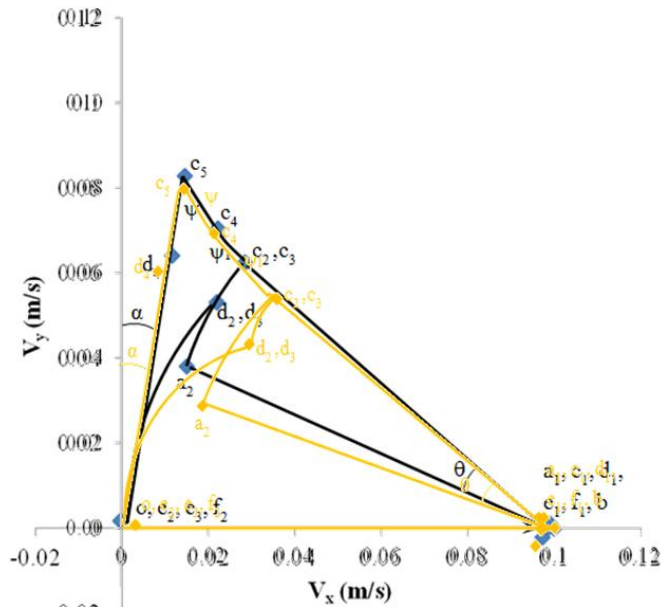


Figure 4.23: The hodograph obtained from simulations for 18  $\mu\text{m}$  DOC and 36  $\mu\text{m}$  DOC were overlapped on one another in order to understand the effect of the depth of cut on different angles in the hodograph. The cutting tool of  $10^\circ$  rake and  $6\mu\text{m}$  edge radius was used. The friction coefficient was kept constant at  $m=0.0$

hodograph with black lines is the one for depth of cut of 36  $\mu\text{m}$  and the one with orange lines is for 18 $\mu\text{m}$  depth of cut. The rake angle was  $10^\circ$  and the cutting edge radius of  $6\mu\text{m}$  along with friction of  $m=0$  was held constant for both the conditions.

It is clear that the angle  $\theta$  is larger for the smaller depth of cut simulation indicating that the chip curl is higher for this case. Also, comparing the  $a_2c_2c_5$  regions of both the hodographs, the region for smaller depth of cut appears to be scaled up.

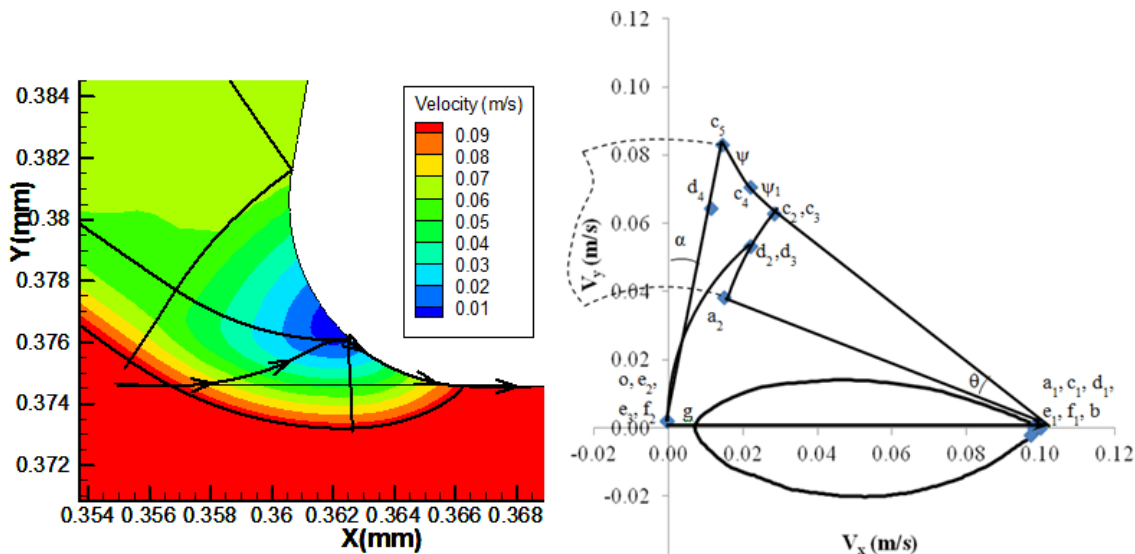


Figure 4.24: The hodograph showing the velocities for the streamline passing through the splitting point. This streamline travels very close to the stagnation point for this  $m=0.0$  case. The rake angle is  $10^\circ$  and the cutting edge radius is  $6\mu\text{m}$ . The depth of cut is  $36\mu\text{m}$ .

In order to understand the flow in the region below the cutting edge, the velocity along the streamline just below the stagnation point ‘S’ was plotted on the hodograph for the cutting condition mentioned in Figure 4.24.

#### **4.12 Equilibrium Based Explanation for Dependence of Shear Plane Angle on the Friction**

As the friction along the chip-tool interface decreases, the friction angle  $\zeta$  increases as per the relation  $\zeta = \frac{1}{2} \cos^{-1}(m)$ . In turn increasing  $(\alpha + \zeta)$ . The sum of friction angle and the rake angle is equal to  $\eta_1 + \psi_1$ , from equation 3. This means that both these angles have to increase to account for the increase in friction angle. Angle  $\eta_1$  is nothing but the equivalent term for the shear plane angle. Hence, as the friction decreases the shear plane angle has to increase. Also, the contact length D4C5 decreases as the friction decreases.

#### **4.13 Significance of the New Slip-Line Field Model**

The most important significance of this newly proposed slip-line field model is that the finite radius of the cutting edge has been accounted accurately without any assumptions about its shape. It has been shown that the primary shear zone has a finite width, which arises due to the cutting edge radius not being zero. The model has also accounted for the interaction between the deformation in the primary and secondary shear zones. Since in the previous models the PSZ was a straight line and not a zone there was no region which was common to the primary as well as secondary shear zone. Since the PSZ has a finite width the region  $C_1C_2D_1D_2$  is common to the PSZ as well as SSZ. The convex slip-line  $A_2C_2$  accurately accounts for the chip curl. Thus, most of the assumptions from the previous metal cutting slip-line field research about the finite cutting edge, width of the PSZ, and chip curl have been eliminated.

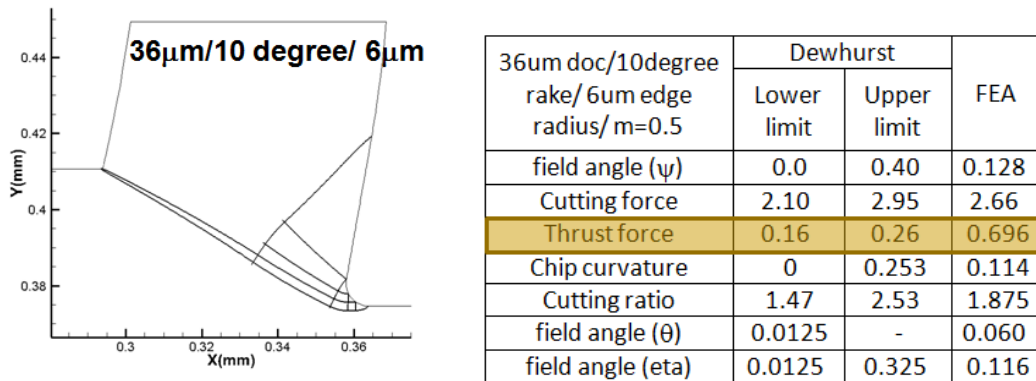


Figure 4.25: The new slip-line field model is similar to the model proposed by Dewhurst (1978)

The field looks very similar to the one proposed by Dewhurst (1978) except that Dewhurst's field was for a sharp tool. In spite of the fact that the slip-line field model proposed by Dewhurst was for a sharp tool, the slip-lines in the SSZ region are very similar. The width of PSZ is zero in case of Dewhurst because of the sharp tool whereas the width of PSZ in the new model is finite due to finite cutting edge radius. Figure 4.25 compares the Dewhurst's model with the new model. The forces obtained from FE simulation were found to fall within the bounds given by Dewhurst.

#### 4.14 Variation of the different angles in the proposed slip-line field

Figure 4.26 presents the generalized slip-line field for curled chips. Different angles shown in the field were measured and plotted as a function of the contact shear stress limiting factor 'm'. The values plotted in the graph were for the tool with rake angle of 10° and cutting edge radius of 6µm. The data is for simulations with a constant depth of cut of 36µm. All the angles in Figure 4.26 are in degrees. From Figure 4.26(a), it can be seen that the angle  $\theta$  decreases from 20° for m=0 to 0.2° for m=0.75 in an exponential manner. The angle  $\theta$ , represents the chip curl and hence as the angle decreases, the curvature of the chip decreases.

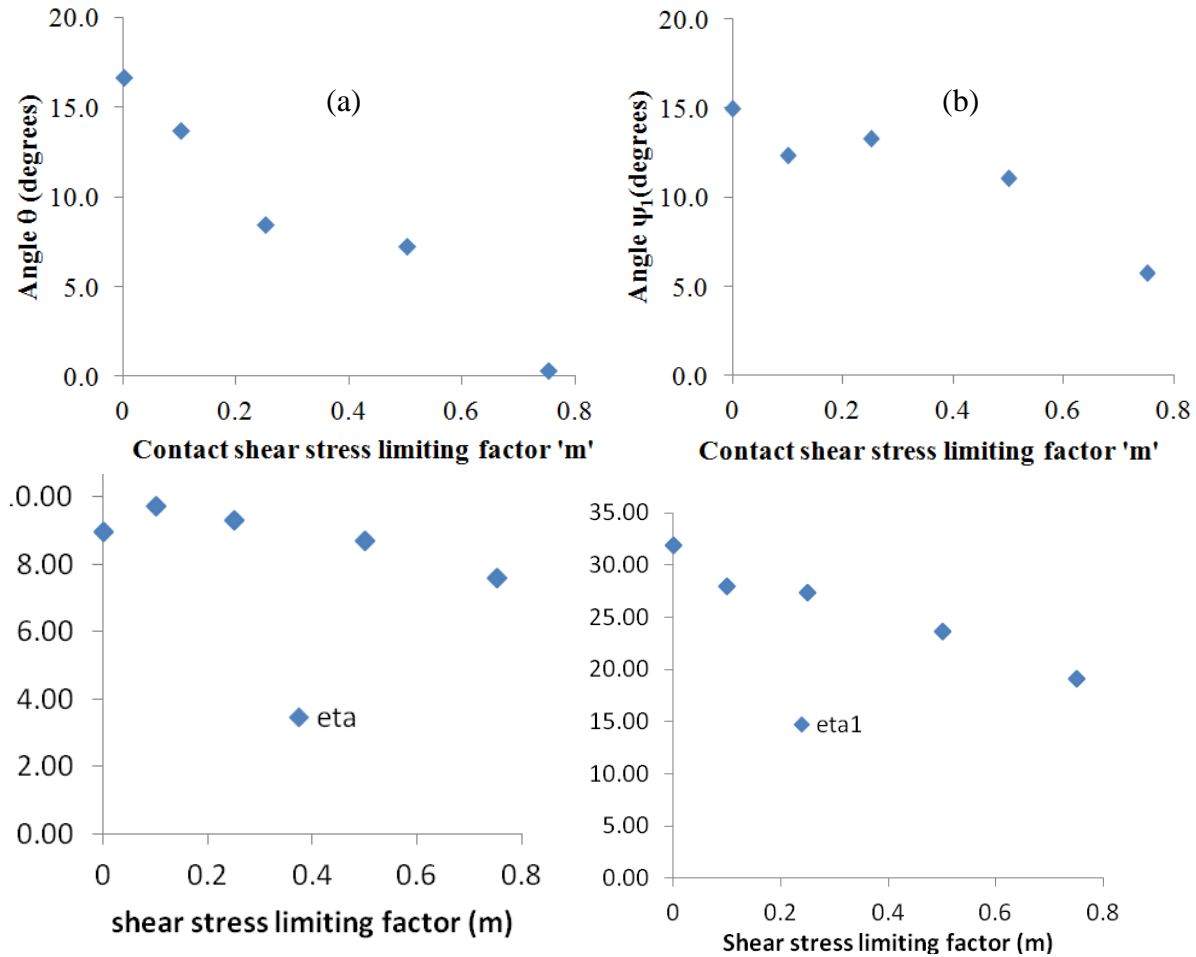


Figure 4.26: Variation of the different angles in the slip-line field (a)  $\theta$ , (b)  $\psi_1$ , (c)  $\eta$ , and (d)  $\eta_1$  with respect to the friction coefficient (m)

Figure 4.26(b) shows the SSZ angle  $\psi_1$  as friction increases the chip curl decreases. The angle  $\psi_1$  is also found to decrease as the friction increases.

#### 4.15 Estimation of the Indentation force Component

Researchers are using metal cutting test as a standard test at high strain and strain rates for material model development. In order to obtain accurate estimates of the flow stress, it is necessary to account for the indentation force component correctly. Indentation force is an additional force arising due to the non zero radius of the cutting edge which does not contribute

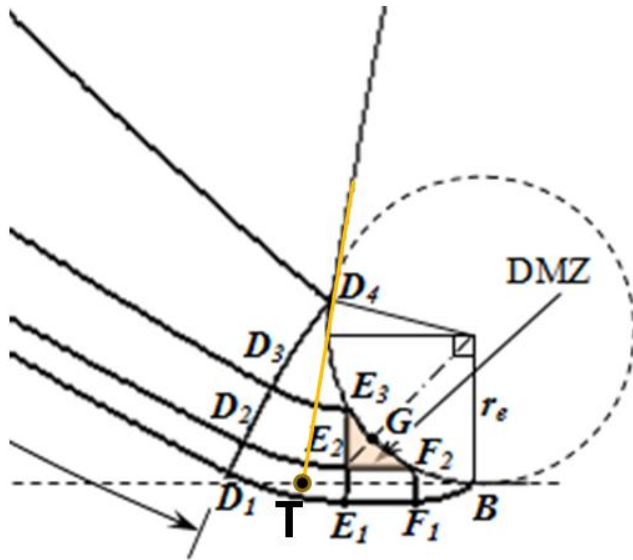


Figure 4.27: For a sharp cutting tool, all the points in the region of influence of the cutting edge would collapse at location ‘T’. In that case the indentation force contribution i.e. the force not accounting towards shearing would come from the additional contact length  $TE_1F_1B$  on the flank side of the tool.

i.e.  $D_4, D_3, D_2,$  and  $D_1$  all meet at point ‘T’. It is known that the total force in metal cutting is the summation of force along the lower bound of the primary shear zone (PSZ). The additional length of the lower bound of the PSZ would be  $TE_1F_1B$ , which would not be present in case of a sharp tool. Thus, the additional force due this additional length is termed as the indentation force. The indentation force component in the cutting and thrust direction are given by equation (2) and equation (3) respectively.

$$I_c = k * l(TE_1F_1B) \quad (2)$$

$$I_t = p * l(TE_1F_1B) \quad (3)$$

Here, ‘k’ is the shear stress and ‘p’ is the hydrostatic pressure in the material. An estimate for the value of the indentation has been obtained below for the tool with  $6\mu\text{m}$  edge

in the shearing of the material. For this reason, it should to be compensated from the total cutting force before obtaining the flow stress estimate.

The slip-line field generated can be used to get an estimate for the indentation force. From Figure 4.27, it can be seen that as the cutting edge radius ( $r_e$ ) tends to zero, the points in the cutting edge region of influence

radius and  $10^\circ$  rake angle. The DOC was  $36\mu\text{m}$  and the cutting velocity was  $1\text{m/s}$  and the shear stress limiting friction factor was  $m=0.75$ .

#### 4.16 Slip-Line Field for Straight Chips

All the slip-line fields obtained so far were for the curled chips. The fields were similar to the one proposed by Dewhurst (1978). In order to obtain the slip-line field for straight chips, finite element simulations with large friction coefficients were carried out. One such simulation is shown in Figure 4.28. Straight chip was obtained for  $18\mu\text{m}$  DOC,  $10^\circ$  rake,  $6\mu\text{m}$  edge radius, and friction coefficient of  $\mu=2.0$ .

The slip-line field obtained was different from the previously discussed field. In this case, the field consists of a PSZ made up of a centered fan field with an included angle of  $17^\circ$ . There exists a velocity discontinuity at the entrance of the PSZ, which is the lowermost radial

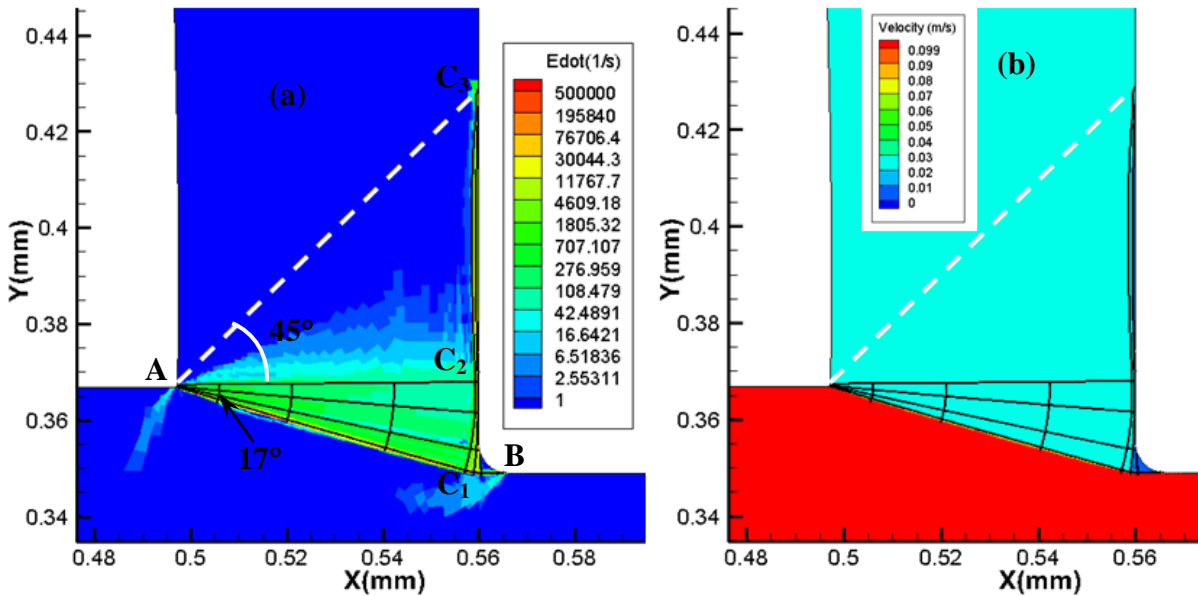


Figure 4.28: A slip-line field was generated for a simulation with  $18\mu\text{m}$  DOC,  $0^\circ$  rake,  $6\mu\text{m}$  edge radius, and friction coefficient of  $\mu=2.0$ . A straight chip was obtained under these cutting conditions. The slip-line field superimposed on (a) strain rate distribution and (b) velocity magnitude has been shown

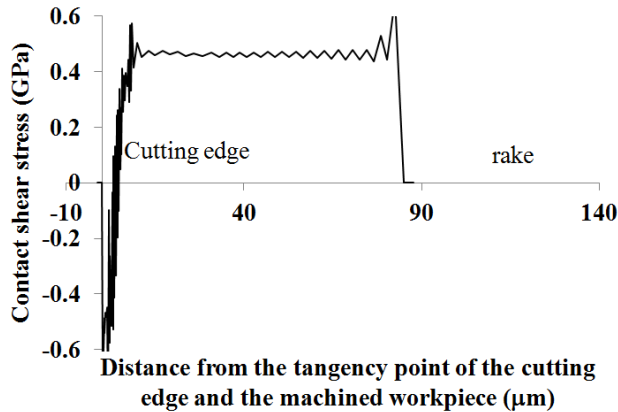


Figure 4.29 The contact shear stress was plotted along the chip-tool contact. The contact shear stress along the rake face was found to be  $\sim 450\text{MPa}$ , which is very close to the shear strength of the material of  $462\text{MPa}$ . This indicated that indeed sticking friction conditions exists along the chip-tool contact

to the length  $C_2C_3$ .

In order to check if the contact shear stress along the chip-tool contact is equal to the

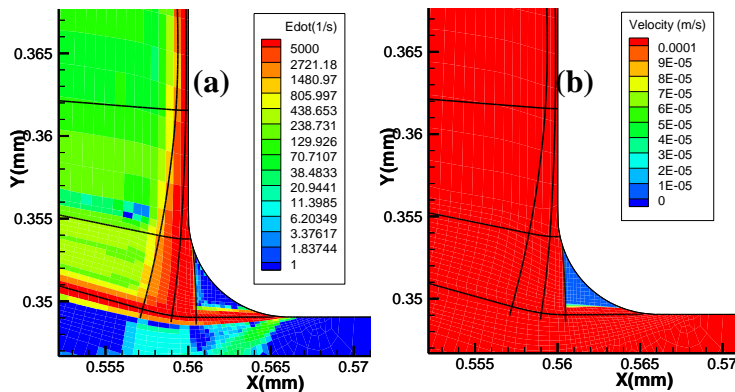


Figure 4.30: The slip-line field for straight chip was superimposed on (a) the strain rate distribution and (b) the velocity magnitude in the region of the cutting edge. A DMZ exists in front of the cutting edge. Also, the strain rate along the lowermost beta slip-line is extremely high indicating the presence of a velocity discontinuity. It can also be seen that the lowermost beta slip-line coming from the free surface changes angle and meets the cutting edge horizontally.

beta slip-line in the centered fan field. The last radial slip-line, which is also the exit of the PSZ, is normal to the rake face of the tool. This is because all the alpha slip-lines originating from the chip-tool contact are parallel to the rake face. Thus, the secondary shear zone has zero width. The last point on contact on the rake face is such that the length of the slip-line  $AC_2$  is equal

shear strength of the material, the

contact shear stress was plotted as a function of the distance from the lower point of tangency of the cutting edge. From Figure 4.29, it can be seen that, indeed the contact shear stress is equal to  $\sim 450\text{MPa}$

which is very close to the shear strength value of  $462\text{MPa}$ . The sticking friction condition is one of

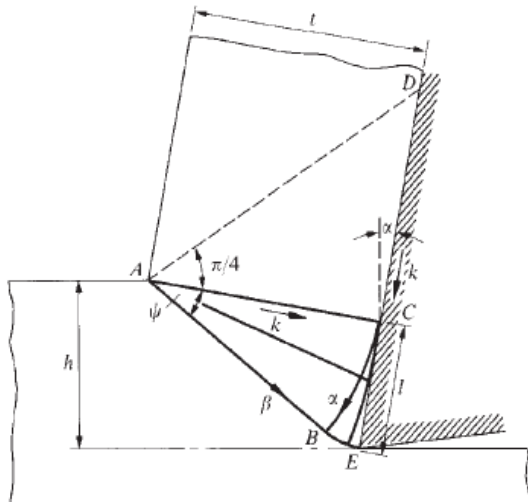


Figure 4.31: The slip-line field proposed by Kudo (1964) showing a centered fan field in the PSZ along with the end of contact being at 45 degrees to the beta slip-line at the exit of the PSZ. This proposed slip-line field is for a sharp tool

of zero degrees, Kudo's model gives the value of  $\psi$  to be  $39.8^\circ$ . However, the stress singularity arising at the point A near the free surface was not accounted for in Kudo's calculations. After applying Hill's calculations for stress singularity, the value of angle  $\psi$  equals  $22.5^\circ$ . The value obtained from FEA is  $17^\circ$ . This difference between the values of  $\psi$  from FEA and  $\psi$  after applying Hill's calculations for stress singularity can be attributed to the presence of the finite radius of the cutting edge.

#### 4.17 Discussion

The slip-lines were obtained from the results of finite element simulations of metal cutting. Based on the slip-lines generated under several machining conditions, a new slip-line field model has been put forward for metal cutting. The newly proposed SLF model has few commonalities and differences about features like the shape and extent of the DMZ, the PSZ and

the most important characteristic of a straight chip.

Closer inspection in the region of the cutting edge reveals the presence of a dead metal zone as shown in Figure 4.30. Also, the strain rate along the lowermost beta slip-line is extremely high indicating the presence of a velocity discontinuity. It can also be seen that the lowermost beta slip-line coming from the free surface changes angle and meets the cutting edge horizontally.

The slip-line field obtained for straight chip is very similar to the one proposed by Kudo (1964) as seen in Figure 4.31. For a tool with a rake angle

the SSZ. The shape of the DMZ is similar to the one proposed by Palmer and Yeo (1963). They showed that the included angle of the DMZ should be  $90^\circ$ , which was the case in the new model proposed here. However, in Palmer and Yeo's work, the upper boundary of the PSZ originated from the point where the cutting edge met the rake face. This was not found to be the case in the newly proposed model. Here, the entire PSZ originated below the DMZ. The upper boundary of the PSZ was the extension of the lower boundary of the DMZ.

Sarvar and Thompson (1982) showed the slip-line field for the case of rake angle being zero degrees. The DMZ was shown to be the extension of the rake face and the machined workpiece. Hence, the lower boundary of the DMZ was horizontal and the upper boundary was shown to be vertical and in line with the rake face. Although, the general location and the included angle of the DMZ were as per the newly proposed model, the shape and the extent of the DMZ are completely different. However, in their work, the indentation force was calculated by taking into account the lower bound of the DMZ, which is horizontal. Same approach of calculating the indentation force, wherein, the points in the region of the cutting edge collapse at one point as shown in Figure 4.27, is used in the current work.

As per the slip-line model proposed by Waldorf et. al. (1998), for the condition of sticking friction, the width of the PSZ would be zero. Also, the shape of the DMZ is such that the included angle is more than  $90^\circ$  which is not possible. There are no retarded flow zones surrounding the DMZ as were observed in the present work. They have modeled the PSZ as a parallel sided zone with the width being constant throughout its length. Also, a chip prow angle has also been added at the free surface by them. From the current work, it is clear that chip prow does not exist at the free surface. In fact, it has been shown that there is a stress singularity at the free surface where the upper and lower boundaries of the narrowing PSZ meet. However, even

in Waldorf's work, it has been shown that the entire deformation reaching the free surface originates below the DMZ, which is same as the observation in the current work. Karpat and Ozel (2006) model is very similar to the one proposed by Waldorf. The only difference is that in Karpat and Ozel's work, the PSZ doesn't collapse to zero width under sticking friction conditions. The slip-line field model proposed in the PhD dissertation of Zhang (2008) is also very similar to the model proposed by Waldorf (1998). The included angle of the DMZ is greater than  $90^\circ$ . A chip prow angle of  $45^\circ$  was assumed in Zhang's model, which was not found to be the case in the current work.

Fang (2003) had proposed a slip-line field for cutting with tools having finite radius of the cutting edge. However, in order to make the analytical calculations simple, the cutting edge was approximated as being made up of two segments meeting at the point of stagnation. This was one of the major differences between the current work and the model proposed by Fang. Other key differences were that there was no DMZ in Fang's model. Also, since the DMZ was absent, the upper boundary of the PSZ originated from the upper point of tangency of the cutting edge and the rake face as opposed to the current work where a DMZ has been shown to exist for all value of friction greater than zero and the PSZ originating below the DMZ.

Thus, the slip-line field model proposed in this current research overcomes the shortfalls of all the previous models. This is the only work, which takes into account the exact shape of the cutting edge radius and shows the presence of the DMZ even for small values of friction coefficients.

#### **4.18 Conclusion**

A Slip-line field model for metal cutting with a tool of finite cutting edge radius has been developed. The slip-lines were generated based on the results of the finite element simulations

using MAPLE. It has been shown that the width of the primary shear zone region is finite and the entire plastic deformation reaching the free surface originate below the lower boundary of the dead metal zone for the case where the chips are curled. Also, it has been shown that there are retarded flow zones present for even a very small value of friction. As the friction is increased, the retarded flow zones are converted to dead metal zones. The exact extents of the dead metal zone can be obtained based on the contours of the strain rate. Unlike previous researchers who have expressed a need of chip pre-flow at the free surface, it has been shown that there exists a point of stress singularity at the free surface rather than a pre-flow region. Thus, the understanding of the large plastic deformations in metal cutting has been improved significantly.

#### **4.19 Acknowledgement**

This material is based upon work supported by the National Science Foundation under grant number EIA-0216178 and grant number EPS-0236913, matching support from the State of Kansas and the Wichita State University High Performance Computing Center. NSF support under grant number DMI-0621174 is also acknowledged.

#### **4.20 References**

Adibi-Sedeh A.H., and Madhavan V., 2003, "Understanding of Finite Element Analysis Results Under the Framework of Oxley's Machining Model," Proceedings of the 6<sup>th</sup> CIRP International Workshop on Modeling of Machining, Hamilton, Ontario, pp 1-15.

Albrecht P., 1960, "New Developments in the Theory of Metal Cutting Process, Part 1: The Ploughing Process in Metal Cutting," Transactions of the ASME, v. 82, pp. 348-358.

Bailey J.A., and Bhanavadia D.G., 1973, "Correlation of Flow Stress with Strain Rate and Temperature During Machining," J. Eng. Mat. Tech., pp. 94-98.

Basuray P.K., Misra B.K., and Lal G.K., 1976, "Transition from Ploughing to Cutting During Machining with Blunt Tools," Wear, v43, n3, pp.341-349.

Challen J.M. and Oxley P.L.B., 1984, "A Slip Line Field Analysis of the Transition from Local Asperity Contact to Full Contact in Metallic Sliding Friction," Wear, v100, pp. 171-193.

Connolly R. and Rubenstein C., 1967, "The Mechanics of Continuous Chip Formation in Orthogonal Cutting," *International Journal of Machine Tool Design*, v8, pp. 159-187.

Deshpande A., Madhavan V., and Al-Bawaneh M., 2010, "Determination of Johnson-Cook Material Model Constants for AISI 4340 HR by Metal Cutting," *Transactions of NAMRI/SME* 38, pp. 25-32.

Fang N., 2003, "Slip-Line Modeling of Machining with a Rounded-Edge Tool – Part 2: Analysis of the Size Effect and the Shear Strain-Rate," *Journal of the Mechanics and Physics of Solids*, v51, pp. 743-762.

Fang N., 2003, "Slip-Line Modeling of Machining with a Rounded-Edge Tool - Part I: New Model and Theory," *Journal of the Mechanics and Physics of Solids*, v51, pp. 715-742.

Fang N., Dewhurst P., 2005, "Slip-Line Modeling of Built-Up Edge Formation in Machining," *International Journal of Mechanical Sciences*, v47, pp. 1079-1098.

Fang N., Jawahir I.S., 2002, "Analytical Predictions and Experimental Validation of Cutting Force Ratio, Chip Thickness, and Chip Back-Flow Angle in Restricted Contact Machining Using the Universal Slip-Line Model," *International Journal of Machine Tools and Manufacture* , v42, pp. 681-694.

Johnson G.R., and Cook W.H., 1983, "A Constitutive Model and Data for Metals Subjected to Large Strains, High Strain Rates and High Temperatures," *Proceedings of the 7<sup>th</sup> International Symposium on Ballistics*, The Hague, Netherlands, pp. 541-547.

Johnson W. and Mellor P.B., *Engineering Plasticity*, Ellis Horwood, 1983.

Karpat Y. and Ozel T., 2006, "Identification of Friction Factors for Chamfered and Honed Tools Through Slip-Line Field Analysis," *Proceedings of the ASME International Conference on Manufacturing Science and Engineering*, pp. 461-470.

Oxley P.L.B., *The Mechanics of Machining: An Analytical Approach to Assessing Machinability*, Ellis Horwood, 1989.

Ozel T. and Zeren E., 2006, "A Methodology to Determine Work Material Flow Stress and Tool-chip Interfacial Friction Properties by Using Analysis of Machining," *ASME Transactions, Journal of Manufacturing Science and Engineering*, v128, pp. 119-129.

Palmer W.B. and Yeo R.C.K., 1963, "Metal Flow Near the Tool Point During Orthogonal Cutting with a Blunt Tool," *Proc. 4<sup>th</sup> International MTDR Conference*, pp. 61-71.

Pujana J., Arrazola P.J., M'Saoubi R., and Chandrasekaran H., 2007, "Analysis of the Inverse Identification of Constitutive Equations Applied in Orthogonal Cutting Process," *International Journal of Machine Tools and Manufacture*, v47, pp. 2153-2161.

Roth R.N. and Oxley P.L.B., 1972, "Slip-Line Field Analysis for Orthogonal Machining Based upon Experimental Flow Fields," *Journal of Mechanical Engineering Science*, v14, pp. 85-97.

Sarwar M. and Thompson P.J., 1982, "Cutting Action of Blunt Tools," *Proceedings of the 22<sup>nd</sup> International MTDR conference*, pp.295-304.

Shatla M., Kerk C., and Altan T., 2001, "Process Modeling in Machining Part I: Determination of Flow Stress Data," *International Journal of Machine Tool and Manufacture*, v41, pp. 1511–1534.

Shi T. and Ramalingam S., 1991, "Slip-Line Solution for Orthogonal Cutting with a Chip Breaker and Flank Wear," *International Journal of Mechanical Sciences*, v33, n9, pp.689-704.

Srinivasan K. and Madhavan V., 2010, "Experimental Determination of Strain Rate and Flow Stress in the Primary Shear Zone While Machining Hot Rolled AISI 4340," *Transactions of NAMRI/SME* 38, pp. 213-220.

Stevenson M.G. and Oxley P.L.B., 1969, "An Experimental Investigation of the Influence of Speed and Scale on the Strain-Rate in a Zone of Intense Plastic Deformation," *Inst Mech Eng Proc (Part 1) Gen Proc*, pp. 561-176.

Waldorf D.J., 2006, "A Simplified Model for Ploughing Forces in Turning," *Journal of Manufacturing Processes*, v8, pp. 76-82.

Waldorf D.J., DeVor R.E., and Kapoor S.G., 1999, "An Evaluation of Ploughing Models for Orthogonal Machining," *Transactions of ASME*, v121, pp. 550-558.

Waldorf D.J., DeVor R.E., and Kapoor S.G., 1998, "A Slip-Line Field for Ploughing During Orthogonal Cutting," *Journal of Manufacturing Science and Engineering*, v120, pp. 693-699.

Waldorf D.J., DeVor R.E., and Kapoor S.G., 1999, "Worn Tool Forces Based on Ploughing Stresses," *Transactions of the North American Manufacturing Research Institution of SME* 27, pp. 165-170.

## CHAPTER 5

### CONCLUSIONS AND FUTURE WORK

#### 5.1 Conclusions

The main aim of this research was to improve the understanding of metal cutting by developing new slip-line fields for cutting with tools of finite edge radius. The first task was to develop and validate a robust slip-line field generation approach. Since machining is a very complex deformation process, the next task was to develop an analogy of machining with a simpler and better understood process like the flat punch compression problem. This would help in understanding the variation of pressure in the cutting tip region in machining. The last task was to generate a new slip-line field for machining with finite edge radius tools, under different cutting conditions and tool geometries. The result of the tasks mentioned above comprise the individual chapters of this dissertation and the key conclusions and findings are summarized below.

A new slip-line field generation approach based on the results of the finite element simulations was first developed and then validated with the aid of a rough punch compression problem. The slip-line field obtained from FEA of rough punch compression was compared with the theoretical slip-line field provided by Johnson and Mellor (1973). The key conclusions are as follows:

- 1) Significance of mesh alignment: It was shown that the alignment of the mesh with the slip-line field is important in order to resolve velocity discontinuities. With the mesh exactly aligned to the slip-line field, it was shown that for the ratio of the punch width to the height of the plate,  $2w/2h=1.6$ , the width of the discontinuity was just two elements wide.

- 2) Mesh size effect: The mesh along the velocity discontinuity was refined by dividing each element along the boundary into eight thin elements in the direction perpendicular to the discontinuity. This simulation with this refined mesh showed that, again, the discontinuity was two elements wide. Thus, it was concluded that irrespective of the size of the elements, the discontinuity was always captured within the width of two elements. Also, the shape and the extent of the dead metal zone was captured accurately by using these elements with a small mesh size perpendicular to the discontinuity. This is very important, since in machining, the regions of discontinuities are localized. The mesh in those local regions can be modified to better resolve the velocity field.
- 3) Validity of the rigid perfectly plastic material assumption: Slip-line field theory is valid only for rigid perfectly plastic material. Implementing a rigid perfectly plastic material in finite element software like Abaqus was not directly possible. In order to overcome this challenge, the Young's modulus of the material was scaled to a very large value of 210,000 GPa compared to the yield strength of 0.8 GPa. This resulted in the elastic strains being very small ( $< Y/E$ ). Also, the material was made incompressible by modifying the Poisson's ratio to 0.499. Plots of the ratio of the plastic strain to the elastic strain showed that the plastic strains were 100 to 1,000 times higher than the elastic strains in the region of interest. Further, the achievement of steady state was also verified by plotting the reaction forces as a function of the punch displacement. It was also verified that the velocity and strain rate fields were independent of the punch displacement. Thus, the material assumptions were valid and the slip-line field theory could be applied.

- 4) Satisfaction of characteristic equations of slip-lines: Hencky's equations, which are derived from the equilibrium equations, and Geiringer's equations which are derived from the compatibility equations, were found to be satisfied everywhere in the region of plastic deformation.

The flat punch indentation simulations were continued further, with focus on the confinement ratio, which is the ratio of the contact length and width of the plate; instead of height as in task one. This was done to understand the transition from the indentation slip-line field given by Prandtl (1920) to the machining slip-line field and to understand the reason for the fairly low pressure at the tip of the cutting tool in machining. The key conclusions are as follows:

- 1) Critical confinement ratio: The slip-line field generated from the results of finite element simulations of flat punch indentation showed that Prandtl's field was obtained only when the confinement ratio was above a critical confinement ratio of 8.75. For confinement ratios  $\leq 8.75$ , the slip-line field was similar to the one observed in metal cutting and an 'S' shaped shear plane was present. The plastic deformation traveled to the side of the block instead of reaching the top surface, forming this 'S' shaped slip line.
- 2) Critical confinement ratio from literature: The value of the critical confinement ratio given by Chakrabarty (1987) is 8.593. The difference between the obtained value of 8.75 and the value from literature was investigated further. It was suspected that this difference was due to the sharp corner of the flat punch. In order to investigate this further, a simulation was carried out with a very small inclination of the punch to the surface, of  $0.05^\circ$ . The main difference was the elimination of the sharp corner.

Indeed the critical confinement ratio dropped from the previously observed value of 8.75, to 8.59 for the case where the punch was inclined, very close to Chakrabarty's value of 8.593. Thus, the higher critical confinement ratio value observed before may be attributed to the excessive deformation arising from the sharp punch corner.

- 3) Pressure at the tip of the cutting tool with finite radius of the cutting edge: Another advantage of the inclined punch simulation was that the contact length increases as the punch displaces. This led to reduction in the confinement ratio as a function of punch displacement. The graph of indentation force as a function of punch displacement was plotted. A drop in the slope was observed as soon as the critical confinement ratio was reached. Also, lower indentation pressures were observed for lower confinement ratios. The confinement ratios in metal cutting are typically less than one, i.e., the depth of cut is less than the tool-chip contact length. This observation of the indentation pressure being lower for smaller confinement ratios explains the lower pressure at the tool tip.

Next task was to develop slip-line field for machining with a tool of finite cutting edge radius. The key conclusions from this work are as follows:

- 1) Slip-line field for cutting with a tool with finite cutting edge radius: For the first, time a slip-line field has been proposed for cutting with a tool of finite cutting edge radius. Previous researchers proposed slip-line fields for machining either assuming the cutting tool to be sharp or simplifying the cutting tip into a few straight segments. The exact shape of the dead metal zone, the retarded flow zones, the primary shear zone and the secondary shear zone have been obtained without making any assumptions about the cutting tool geometry.

- 2) Shape of the primary shear zone: It has been shown that the primary shear zone is a zone of finite width. The maximum width is at the cutting tip and decreases to zero at the free surface, i.e. a pressure singularity. The maximum width of the PSZ decreases as the friction along the chip-tool interface increases. The centered fan field originating from the singularity at the free surface is doubly curved. Also, the angle  $\theta$  of this field along the PSZ decreases as the friction increases and PSZ becomes straight. This decreases the chip curl as well. Another important finding is that the entire deformation reaching the free surface (i.e. the shear velocity added along all points of the PSZ) originates below the dead metal zone.
- 3) Extent of the dead metal zone: The dead metal zone starts as a stagnation point for the case of zero friction. As the friction coefficient along the chip-tool contact increases, the stagnation point expands into a triangular dead metal zone. It has been shown that the dead metal zone is present for all values of friction greater than zero. The location of the boundaries of the DMZ along the cutting edge radius have been established to be the points where the tangent to the cutting edge makes an angle equal to the friction angle with the horizontal and vertical directions. Also, it has been shown that there are retarded flow zones surrounding the dead metal zone.
- 4) Slip-line field for straight chips: An attempt has been made to develop a slip-line field for conditions under which straight chips are formed. It has been shown that the PSZ comprises of a centered fan field with its center located at the free surface. The field is similar to the one proposed by Kudo (1965). However, Kudo (1967) has not applied the stress singularity at the free surface, which results in the prediction of higher shear plane angle in his model. The slip-lines in the secondary shear zone are

parallel to the rake face and the contact length is equal to the maximum radius of the center fan field observed in the PSZ. Further analyses are required to better understand the variation of the slip-line field under different cutting conditions and the tool geometry.

## 5.2 Future Work

The ability to generate slip-lines from the results of finite element simulations has opened the doors to many opportunities. Some immediate work, that can complement the current work, are as follows:

- 1) Straight chips with stress singularity: It is required to develop a capability to implement sticking friction in Abaqus so that simulations with straight chips can be carried out without elastic effects. These simulations can then be used to validate the slip-line field under sticking friction (straight chip) conditions.
- 2) Study the deformation due to restricted contact tools or tools with edge preps: The same approach can be used to study the deformation with more complex cutting tool geometries. The slip-line models can then be used to optimize the design of the cutting tools.
- 3) Apply the slip-line field theory for work hardening material: This new approach of obtaining machining slip-lines can be implemented along with the slip-line field theory extended to the work hardening materials (Oxley, 1989).

## **BIBLIOGRAPHY**

## BIBLIOGRAPHY

Adibi-Sedeh A.H., and Madhavan V., 2003, "Understanding of Finite Element Analysis Results Under the Framework of Oxley's Machining Model," Proceedings of the 6<sup>th</sup> CIRP International Workshop on Modeling of Machining, Hamilton, Ontario, pp 1-15.

Adibi-Sedeh A.H., Madhavan V., and Bahr B., 2003, "Extension of Oxley's Analysis of Machining to use Different Material Models," Journal of Manufacturing Science and Engineering, v125, n4, pp. 656-666.

Albrecht P., 1960, "New Developments in the Theory of Metal Cutting Process, Part 1: The Ploughing Process in Metal Cutting," Transactions of the ASME 82, 348-358.

Basuray P.K., Misra B.K., and Lal G.K., 1976, "Transition from Ploughing to Cutting During Machining with Blunt Tools." Wear 43, n 3, pp.341-349.

Chakrabarty, J., 2006, "Theory of Plasticity", 3rd Ed, Elsevier Butterworth-Heinemann.

Childs T.H.C., Maekawa K., Obikawa T. And Yamane Y., 2000, "Metal Machining Theory and Applications", Publisher: Arnold Publishers

Collins I. F., 2011, "The Algebraic-Geometry of Slip Line Fields with Applications to Boundary Value Problems," Proceedings of the Royal Society of London, Series A: Mathematical and Physical Sciences, v 303, n 1474, pp 317-338.

Connolly R. and Rubenstein C., 1967, "The Mechanics of Continuous Chip Formation in Orthogonal Cutting," International Journal of Machine Tool Design 8, pp. 159-187.

Deb A., Prevosta J.H., Loretb B., 1996, "Adaptive meshing for dynamic strain localization," Computational Methods in Applied Mechanics and Engineering, v137, pp 285-306.

Deshpande A., Madhavan V., and Al-Bawaneh M., 2010, "Determination of Johnson-Cook Material Model Constants for AISI 4340 HR by Metal Cutting.", Transactions of NAMRI/SME 38, pp. 25-32.

Deshpande A., Madhavan V. and Adibi-Sedeh A.H., 2011, "Models for the Indentation Force in Metal Cutting," Transactions of the North American Manufacturing Research Conference, Corvallis, OR, v39, pp 233-242

Dewhurst P. and Collins, I. F., 1973, "A Matrix Technique for Constructing Slip-Line Field Solutions to a Class of Plane Strain Plasticity Problems," International Journal of Numerical Methods in Engineering, v7, pp 357-378.

- Dewhurst, P., 1985, "A general matrix operator for linear boundary value problems in slip-line field theory", *International Journal for Numerical Methods in Engineering* V21,n1, pp 169-182.
- Dewhurst, P., 1978, "On the Non-Uniqueness of the Machining Process," *Proceedings of the Royal Society, London A*, v360, n1703, pp.587-610.
- Ernst H. J., Merchant M. E., 1941, *Trans. Am. Soc. Metals* v29, pp.299
- Ewing D. J. F., 1967, "A Series-Method for Constructing Plastic Slipline Fields," *Journal of Mechanics and Physics of Solids*, v 15, pp 105-114.
- Fang N., 2003, "Slip-Line Modeling of Machining with a Rounded-Edge Tool – Part 2: Analysis of the Size Effect and the Shear Strain-Rate.," *Journal of the Mechanics and Physics of Solids* 51, pp. 743-762.
- Fang N., 2003, "Slip-Line Modeling of Machining with a Rounded-Edge Tool - Part I: New Model and Theory." *Journal of the Mechanics and Physics of Solids* 51, pp. 715-742.
- Gutierrez M.A., De Borst R., Schellekens J.C.J., Sluys L.J., 1995, "An algorithm for mesh rezoning with application to strain localization problems," *Computers and Structures*, v55, n2, pp. 237-247.
- Hencky H., 1923, "Über Einige Statisch Bestimmte Fälle Des Gleichgewichts In Plastischen Körpern", *Zeitschrift für Angewandte Mathematik und Mechanik*, v3, n4, pp 241-251
- Hill R., 1950, "The Mathematical Theory of Plasticity," Clarendon Press, Oxford.
- Haddow J.B., Johnson W. 1962, "Experiments in the piercing of soft metals," *International Journal of Machine Tool Design and Research*, v2, n1, pp 1-18.
- Heginbotham W. B., Gogia S. L., 1961, "Proceedings of the Institution of Mechanical Engineers, Metal cutting and the buildup nose, pp 892-917.
- Simo J.C., Oliver J., Armero F., 1993, "An analysis of strong discontinuities induced by strain-softening in rate independent inelastic solids", *Comput. Mech*, v12, pp 277-296.
- Manjunathaiah J., Endres W.J. 2000, "A New Model and Analysis of Orthogonal Machining With an Edge-Radiused Tool," *Transactions of the ASME*, v 122.
- Johnson, W., and Mellor, P. B., 1973, "Engineering Plasticity", 1st Ed, Van Nostrand Reinhold.
- Karpat Y. and Ozel T., 2006, "Identification of Friction Factors for Chamfered and Honed Tools Through Slip-Line Field Analysis." *Proceedings of the ASME International Conference on Manufacturing Science and Engineering*, pp. 461-470.
- Kudo H., 1965, "Some new slip-line solutions for two-dimensional steady-state machining" *Int. J. Mech. Sci.* v7, pp. 43–55.

Lyamin A.V., Sloan S.W., Krabbenhøft K., and Hjjaj M., 2005, “Lower bound limit analysis with adaptive remeshing,” *International Journal for Numerical methods in Edngineering*, v 63, pp 1961–1974.

Madhavan V. and Hijazi A., 2004, “Use of Ultra High Speed Imaging to Study Material Deformation during High Speed Machining,” *Proceedings of the 2004 NSF Design, Service and Manufacturing Grantees and Research Conference*

Oxley P.L.B., *The Mechanics of Machining: An Analytical Approach to Assessing Machinability*, Ellis Horwood, 1989.

Palmer W.B. and Yeo R.C.K., 1963, “Metal Flow Near the Tool Point During Orthogonal Cutting with a Blunt Tool,” *Proc. 4th Int. MTDR Conference*, pp. 61-71.

Peraire J., Vahdati M., Morgan K. and Zienkiewicz O.C., 1987, “Adaptive remeshing for compressible flow computations”, *Journal of Computational Physics*, v72, pp. 449-466.

Petryk H., 1987, “Slip Line Field Solutions for Sliding Contact,” *Proceedings of International Conference on Tribology - Friction, Lubrication and Wear Fifty Years On*, pp 987–994.

Prandtl L., 1920, “Über die Härte plastischer Körper,” *Göttingen Nachr, Math. Phys. K1*, v12, pp. 74-85.

Regueiro R.A., Borja R.I., 1999, “A finite element model of localized deformation in frictional materials taking a strong discontinuity approach,” *Finite Elements in Analysis and Design*, v 33, pp 283-315.

Sandvik Coromant, *Modern Metal Cutting: a Practical Handbook*, 1<sup>st</sup> Ed., 1996

Sarwar M. and Thompson P.J., 1982, “Cutting Action of Blunt Tools,” *Proceedings of the 22<sup>nd</sup> International MTDR conference*, pp.295-304.

Schimmel R.J., Manjunathaiah J., and Endres, W.J., 2000, “Edge Radius Variability and Force Measurement Considerations,” *Journal of Manufacturing Science and Engineering*, v122, pp. 590-594.

Shi T. and Ramalingam S., 1991, “Slip-Line Solution for Orthogonal Cutting with a Chip Breaker and Flank Wear,” *International Journal of Mechanical Sciences*, v33, n9, pp.689-704.

Sloan S.W., 2008, “Limit Analysis With Adaptive Mesh Refinement,” 8<sup>th</sup> World Congress on Computational Mechanics (WCCM8)

Smith C.C. and Gilbert M., 2007, Application of discontinuity layout optimization to plane plasticity problems,” *Proc. R. Soc. A*, v463, pp. 2461–2484.

Srinivasan K. and Madhavan V., 2010, "Experimental Determination of Strain Rate and Flow Stress in the Primary Shear Zone While Machining Hot Rolled AISI 4340," Transactions of NAMRI/SME 38, pp. 213-220.

Steinmann P., Betsch P., 2000, "A localization capturing FE-interface based on regularized strong discontinuities at large inelastic strains," International Journal of Solids and Structures, v 37, pp 4061-4082.

Stevenson M.G. and Oxley, P.L.B., 1969, "An experimental investigation of the influence of speed and scale on the strain-rate in a zone of intense plastic deformation," Inst Mech Eng Proc (Part 1) Gen Proc, pp. 561-176.

Tan T.M., Li S., and Chou P.C., 1989, "Finite element solution of Prandtl's flat punch problem," Finite Elements in Analysis and Design, v6, pp.173-186.

Toulios M., and Collins I. F., 1982, "A Technique for Calculating the Continued Deformation of a Class of Slip Line Field Solutions," International Journal of Mechanical Sciences, v 24, n2, pp. 61-72.

Waldorf D.J., 2006, "A Simplified Model for Ploughing Forces in Turning," Journal of Manufacturing Processes, v8, pp.76-82.

Waldorf D.J., DeVor R.E., and Kapoor S.G., 1996, "An Evaluation of Ploughing Models for Orthogonal Machining," Transactions of ASME, v121, pp. 550-558.

Waldorf D.J., DeVor R.E., and Kapoor S.G., 1998, "A Slip-Line Field for Ploughing During Orthogonal Cutting," Journal of Manufacturing Science and Engineering, v120, pp. 693-699.

Waldorf D.J., DeVor R.E., and Kapoor S.G., 1999, "Worn Tool Forces Based on Ploughing Stresses," Transactions of the North American Manufacturing Research Institution of SME 27, pp. 165-170.

Zhang Z., 2008, "Slip Line Modeling of Machining with Worn Blunt Cutting Tools," PhD Dissertation, Michigan Technological University.